NASA/CR-20250002768

Hybrid Thermally Efficient Core (HyTEC) High Temperature CMC Vanes Final Report

John Shaw, Evan Benjamin Callaway, and David Litton
Pratt & Whitney, East Harford, Connecticut

GV Srinivasan and Thomas Martin
RTX, East Harford, Connecticut

Miriam Lazur
Pratt & Whitney, Carlsbad, California

March 2025

NASA STI Program . . . in Profile

Since its founding, NASA has been dedicated to the advancement of aeronautics and space science. The NASA scientific and technical information (STI) program plays a key part in helping NASA maintain this important role.

The NASA STI program operates under the auspices of the Agency Chief Information Officer. It collects, organizes, provides for archiving, and disseminates NASA's STI. The NASA STI program provides access to the NTRS Registered and its public interface, the NASA Technical Reports Server, thus providing one of the largest collections of aeronautical and space science STI in the world. Results are published in both non-NASA channels and by NASA in the NASA STI Report Series, which includes the following report types:

- TECHNICAL PUBLICATION.
  Reports of completed research or a major significant phase of research that present the results of NASA programs and include extensive data or theoretical analysis. Includes compilations of significant scientific and technical data and information deemed to be of continuing reference value. NASA counterpart of peer-reviewed formal professional papers but has less stringent limitations on manuscript length and extent of graphic presentations.

- TECHNICAL MEMORANDUM.
  Scientific and technical findings that are preliminary or of specialized interest, e.g., quick release reports, working papers, and bibliographies that contain minimal annotation. Does not contain extensive analysis.

- CONTRACTOR REPORT.
  Scientific and technical findings by NASA-sponsored contractors and grantees.

- CONFERENCE PUBLICATION.
  Collected papers from scientific and technical conferences, symposia, seminars, or other meetings sponsored or cosponsored by NASA.

- SPECIAL PUBLICATION.
  Scientific, technical, or historical information from NASA programs, projects, and missions, often concerned with subjects having substantial public interest.

- TECHNICAL TRANSLATION.
  English-language translations of foreign scientific and technical material pertinent to NASA's mission.

Specialized services also include organizing and publishing research results, distributing specialized research announcements and feeds, providing information desk and personal search support, and enabling data exchange services.

For more information about the NASA STI program, see the following:

- Access the NASA STI program home page at http://www.sti.nasa.gov

NASA/CR-20250002768

Hybrid Thermally Efficient Core (HyTEC) High Temperature CMC Vanes Final Report

John Shaw, Evan Benjamin Callaway, and David Litton
Pratt & Whitney, East Harford, Connecticut

GV Srinivasan and Thomas Martin
RTX, East Harford, Connecticut

Miriam Lazur
Pratt & Whitney, Carlsbad, California

Prepared under Contract 80GRC21CA009

National Aeronautics and
Space Administration

Glenn Research Center
Cleveland, Ohio 44135

March 2025

This work was sponsored by the Advanced Air Vehicles Program
at the NASA Glenn Research Center.

Level of Review: This material has been technically reviewed by NASA expert reviewer(s).

This report is available in electronic form at https://www.sti.nasa.gov/ and https://ntrs.nasa.gov/

NASA STI Program/Mail Stop 050
NASA Langley Research Center
Hampton, VA 23681-2199

TABLE OF CONTENTS

LIST OF FIGURES

LIST OF TABLES

ACRONYMS

	-A-
APS	Air Plasma Spraying
ASTM	American Society for Testing and Materials
	-B-
BSE SEM	Backscattered Scanning Electron Microscope
	-C-
CDR	Critical Design Review
CFD	Computational Fluid Dynamics
CMAS	Calcia-magnesia-alumino-silicate
CMC	Ceramic Matrix Composite
COD	Crack Opening Displacement
CVI	Chemical Vapor Deposition
	-D-
DDP	Durability Design Point
	-E-
EBC	Environmental Barrier Coating
	-F-
FCT	Furnace Cycle Testing
FEM	Finite Element Mesh
	-H-
HPC	High Pressure Combustor
HPT	High Pressure Turbine
HPTC	High Pressure Thermal Cycle
HyTEC	Hybrid Thermally Efficient Core
	-I-
IFC	Interface Coating
ILT	Interlaminar Tension
ILS	Interlaminar Stress
	-K-
KPP	Key Performance Parameter
	-M-
MRL	Manufacturing Readiness Level
	-N-
NASA	National Aeronautics and Space Administration
NGSA	Next Generation Single Aisle Aircraft
	-O-
OEM	Original Equipment Manufacturer
OPR	Overall Pressure Ratio

-P-

P&W	Pratt & Whitney

-R-

RT	Room Temperature
RTRC	Raytheon Technologies Research Center

-S-

SEM	Scanning Electron Microscope
SiC	Silicon Carbide
SOA	State of the Art

-T-

TC	Thermocouple
TPM	Technical Performance Measure
TRL	Technology Readiness Level
TSFC	Thrust Specific Fuel Consumption

-V-

VLM	Visible Light Microscope

1 INTRODUCTION & BACKGROUND

The cooling of airfoils within a modern high-pressure turbine (HPT) presents a formidable challenge due to the high operating temperatures needed to support optimized cycles for reduced fuel burn. As engines become more fuel efficient, the turbine inlet temperatures continue to increase beyond the temperature capability of turbine airfoil materials. It is therefore necessary to have effective cooling designs in order to protect turbine components from the hot mainstream gases. The air used for cooling purposes is extracted from the high-pressure-compressor stages, which results in a performance penalty because the cooling air bypasses some of the work extraction of the first turbine stage. Therefore, for optimum performance, it is necessary to minimizing the amount of turbine cooling air.

The NASA HyTEC program focuses on improving U.S. based Original Engine Manufacturers (OEMs) in the advancement of critical technologies for the next generation of aircraft propulsion. Today, the vision of this future architecture includes engine hybridization and small core designs. To enable this vision, Pratt & Whitney has identified five (5) campaigns through the HyTEC program that will help bridge the TRL gap between today's capability and the requirements of this architectural change. This contract is focused on implementation of Ceramic Matrix Composites (CMCs) in small core HPT.

The key benefit from high temperature CMC vanes will be the reduction in turbine cooling air derived from the high temperature capability of the CMC / EBC material system. The reduced turbine cooling air can then be traded for improved thrust specific fuel consumption (TSFC) for given flight points and integrated throughout the mission to calculate fuel burn reduction. The reduction in turbine cooling air from the high temp CMC vanes will be calculated by scaling the cooling requirements based on the temperature capability demonstrated by the CMC / EBC material system via testing in the HyTEC work scope. By decomposing the mission profile into temperature buckets, the required mission times at temperature will be established. Therefore, better performance of the material in the HyTEC testing will translate to less required cooling flow. Conversely, poorer performance of the material will translate to the need for more required cooling flow (and therefore, less overall benefit).

This final report will serve as a summary of the work completed under this contract and how each individual task performed against the Technical Performance Measures (TPM). This final report will include test results and conclusions from each of the individual Task Reports that were generated to status the program's success and learning developed. At the conclusion of this report a status of all TPM's and the present status of the associated Technology Readiness Levels (TRL) will be presented.

SiC/SiC CMCs are commonly accepted to have a pesting regime which relates to relative rates of oxidation of their constituent phases. At high temperatures (>2200°F) the oxidation of SiC is relatively rapid, allowing any cracks in the matrix – so long as they are sufficiently small – to seal with oxidation product before the bulk of the substrate is compromised. However, creep becomes a concern for prolonged exposure at elevated temperatures. At intermediate temperatures (~1200°F-2000°F) oxidation of SiC is sluggish, allowing oxygen ingress through open cracks to attack a C- or BN-based interface coating and compromise the strength of the composite. At lower temperatures oxidation of all phases is sluggish and no time-dependent effect on properties is expected. The presence and size of matrix cracks, controlled by the in-plane stress on the composite, also controls the rate of oxidation – at sufficiently low applied stress, no matrix cracks should be present, and no oxidative degradation is expected to occur. These regimes of material behavior are summarized in Figure 1.

This project hypothesizes that a commercial engine cycle, with short exposures at high temperature and longer exposures at moderate temperature, may enable beneficial interactions

of these oxidation mechanisms. The short, high temperature exposures may be sufficient to seal matrix cracks and prevent pesting during the long, intermediate temperature exposures. This regime is labeled as “Matrix Crack Sealing” in Figure 1.

A second mechanism is hypothesized in which both temperature and stress are cycled. Oxide which forms at the interface coating would be rich in boria, with a lower softening temperature than the silica formed on the crack faces. If a specimen is loaded when hot, the crack would interact with a soft phase at the fiber surface and may be blunted. If a specimen is loaded when cold, the crack would interact with a rigid phase at the fiber surface and may propagate through the fiber. The order of heating and loading may be alternated to explore this mechanism.

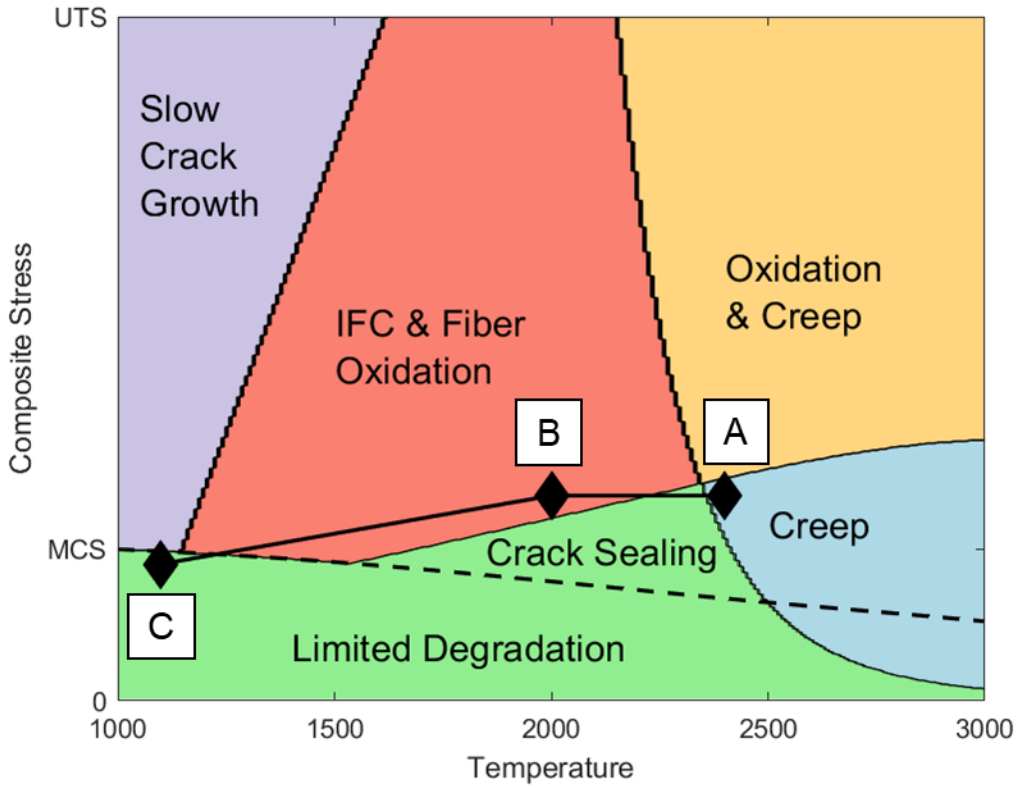

Figure 1. Degradation mechanism map for CMCs at high temperature. Overlayed lines indicate approximate stresses and temperatures of (A) takeoff, (B) cruise, and (C) idle conditions

A model was built to simulate a commercial mission cycle of an uncooled CMC high-pressure turbine vane to assess whether and where the above mechanisms were likely to occur. The relative temperatures at the Environmental Barrier Coating (EBC) surface, the EBC/CMC interface, and the backside of CMC as a function of elapsed time in one mission are shown in Figure 2. The highest temperatures occur over the first 5 minutes during takeoff. Temperature then decreases somewhat for 15 minutes of climb before decreasing to cruise temperatures for roughly 30 minutes. Temperatures then drop off sharply for a slow descent for roughly an hour, then rise slowly for maneuvering for landing. Short term temperature spikes occur at the end of the mission when thrust reversing is deployed.

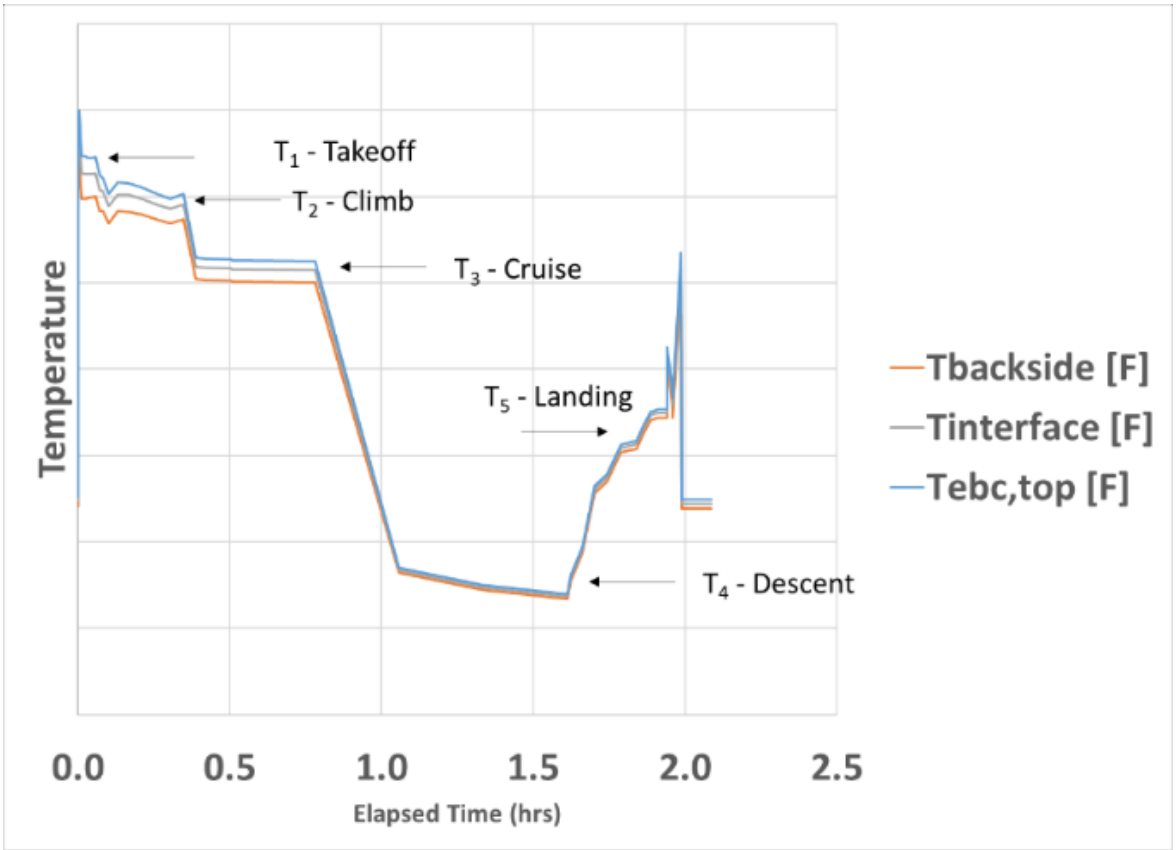

Figure 2. Notional commercial mission cycle and corresponding material temperatures for an uncooled CMC high-pressure turbine vane

In conjunction with thermal data, a preliminary structural analysis was performed on a vane for the takeoff, cruise, and idle thermal boundary conditions. This is the second input in an assessment of the degradation behavior of a component. Stress and temperature maps are shown in Figure 3. This analysis identifies regions of the interior cavity of the vane that would be above the matrix cracking stress during cruise and takeoff conditions at surface temperatures that straddle the pesting and crack sealing temperature regimes. Furthermore, since this interior region of the vane is exposed to cooling circuit air and not gas path air, the analysis and testing are simplified – water vapor content is lower, and CMAS would not be present. The stress, temperature, and environmental conditions of this region form the basis of the test campaign described in Section 3.

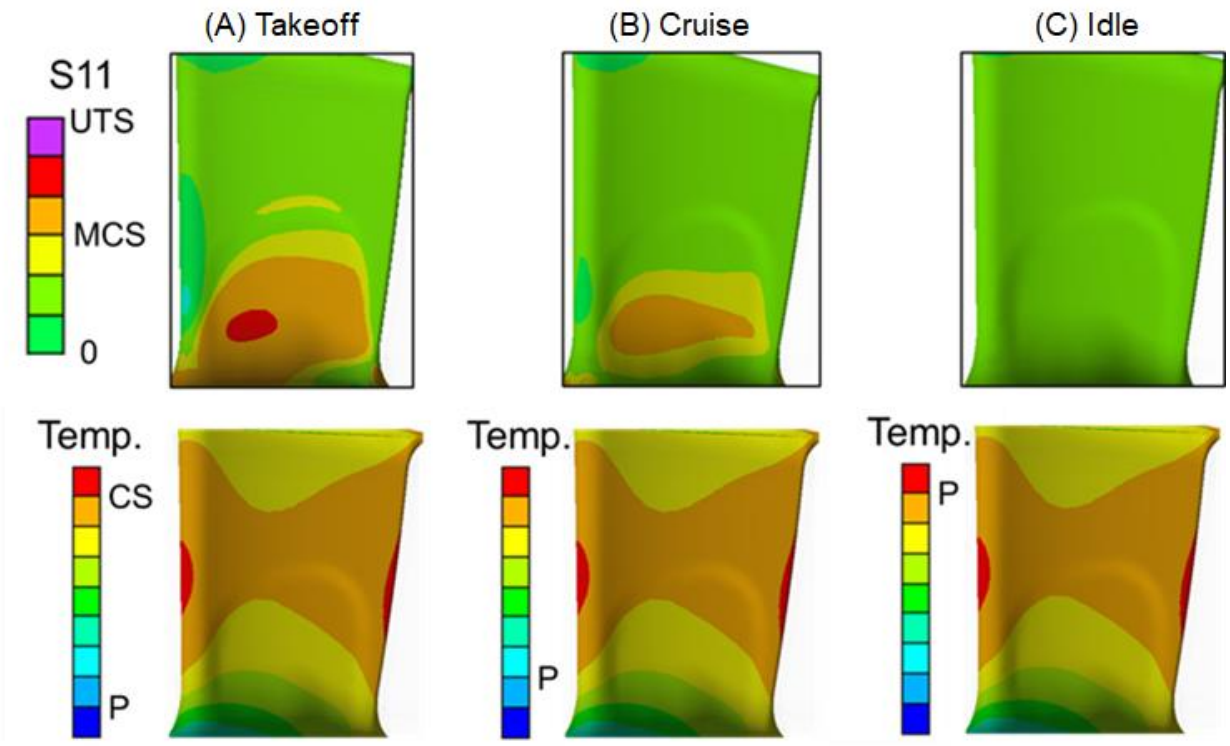

Figure 3. Predicted stresses and temperatures on the pressure side cavity wall at (A) takeoff, (B) cruise, and (C) idle. The colormap for stress (S11) is normalized by the matrix cracking stress (MCS) and ultimate tensile strength (UTS) at room temperature. The colormap for temperature is normalized by the lower bound onset of pesting (P) and the onset of crack sealing (CS) of the matrix.

2 TECHNOLOGY DEVELOPMENT PLAN

2.1 CMC DURABILITY TESTING (TASK 2.1)

The TRL advancement strategy for this task was to improve the prediction capability of CMC Lifing models developed by P&W to support product maturity to TRL 6 and beyond. Data obtained through coupon testing under this task will be used to confirm existing material properties and validate lifing model capabilities. The CMC lifing model was developed by P&W to predict CMC component durability and expected life.

2.2 EBC DURABILITY TESTING (TASK 2.2)

The TRL advancement strategy for this task was to improve the prediction capability of EBC Lifing models developed by P&W to support product maturity to TRL 6 and beyond. Data obtained through coupon testing under this task will be used to confirm existing EBC material properties and validate lifing model capabilities. The EBC lifing model was developed by P&W to be used in conjunction with the P&W CMC lifing model to predict CMC component durability and expected life.

2.3 HIGH TEMPERATURE CMC VANE DESIGN AND VALIDATION (TASK 2.3)

The TRL advancement strategy for this task was to validate CMC component design features and application of CMC and EBC lifing models to component geometries. A CMC HPT vane design was selected and optimized for Task 2.3 rig testing at Raytheon Technologies Research Center's (RTRC) High Pressure Thermal Cycle (HPTC) rig.

2.4 TPM DEFINITION

2.4.1 KPP1: Fuel Burn Reduction attributed to high-power density-core of the original equipment manufacturer's vision engine.

The key benefit from high temperature CMC vanes will be the reduction in turbine cooling air derived from the high temperature capability of the CMC / EBC material system. The reduced turbine cooling air can then be traded for improved thrust specific fuel consumption (TSFC) for given flight points and integrated throughout the mission to calculate fuel burn reduction. The reduction in turbine cooling air from the high temperature CMC vanes will be calculated by scaling the cooling requirements based on the temperature capability demonstrated by the CMC / EBC material system via testing in the HyTEC work scope. By decomposing the mission profile into temperature buckets, the required mission times at temperature will be established. Therefore, better performance of the material in the HyTEC testing will translate to less required cooling flow. Conversely, poorer performance of the material will translate to the need for more required cooling flow (and therefore, less overall benefit). The translation of Technical Performance Metrics (TPM's) to key Performance Points (KPP's) is highlighted in Figure 3, shown below.

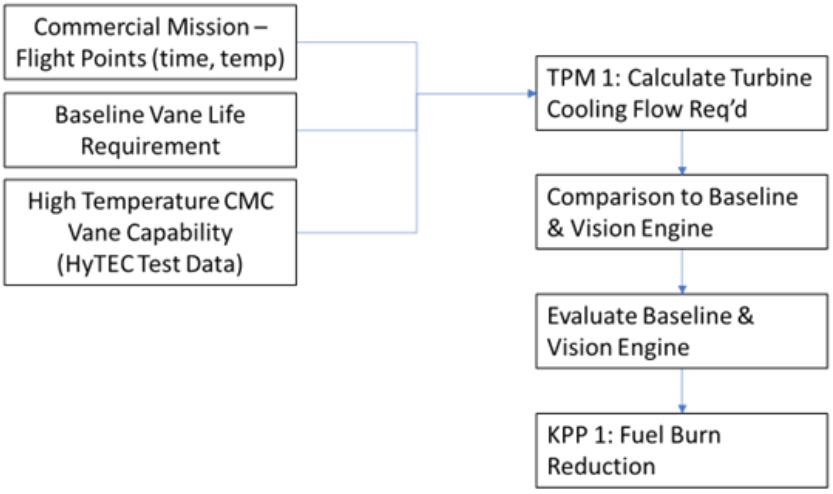

Figure 4. KPP #1 relationship to TPM #1.

2.4.2 KPP3: Engine Overall Pressure Ratio (defined at top of climb)

The high temperature CMC vane technology enables the turbine to run at higher engine Overall Pressure Ratio (OPR) in two ways; first by reducing turbine cooling flow requirements, making the core more efficient. The higher temperature capability of the material supports increase T3 levels, which is representative of higher OPR engines.

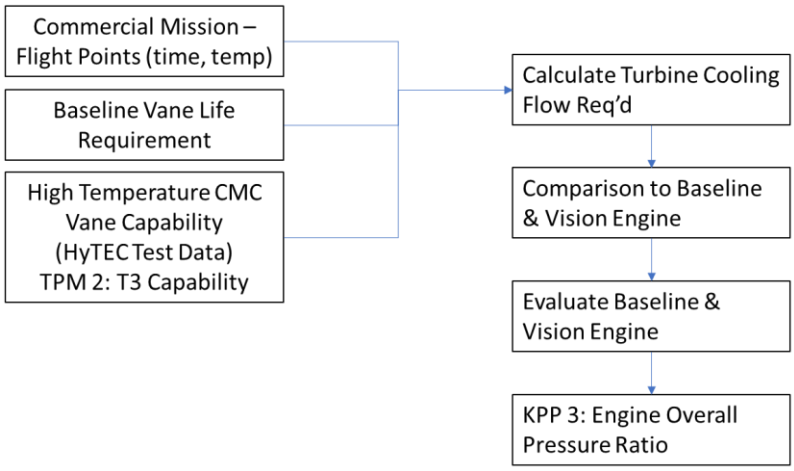

Figure 5. KPP #3 relationship to TPM #2.

2.4.3 KPP4: Durability, measured in operating hours between major refurbishments

The alternative benefit from high temperature CMC vanes would be to utilize the material capability to extend component life or durability by maintaining baseline levels of turbine cooling (running longer at lower temperatures). The increased durability will be assessed following a similar approach as KPP1, but now the turbine cooling will be held fixed, and any excess capability from the CMC / EBC material system will be translated into additional life of the vanes based on the testing results. This translation of technical performance metrics (TPM's) to key Performance Points (KPP's) is highlighted in Figure 6, shown below.

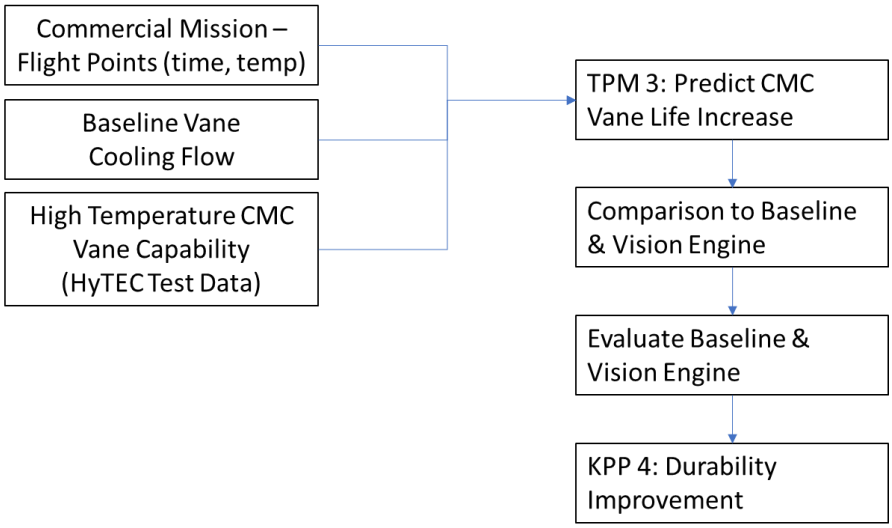

Figure 6. KPP #4 relationship to TPM #3.

2.4.4 KPP6: HPC Exit Corrected Flow

The scale of the NASA HyTEC Vision Engine will be smaller than current State of the Art engine. KPP #6 is an evaluation of the size of the engine core. The high temperature CMC vane technology will thermodynamically enable these smaller core sizes but will also need to be geometrically compatible with these smaller core sizes for critical features such as airfoil leading edge radii, and trailing edge thickness to ensure the aerodynamics of the small core size are delivered to meet the thermal efficiencies of the Vision Engine.

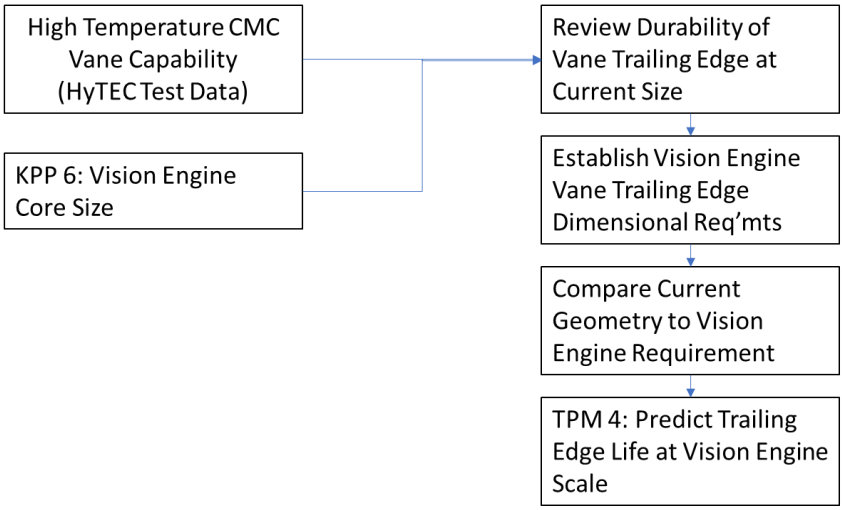

Figure 7. KPP #6 relationship to TPM #4.

3 PLANNING AND EXECUTION

This section will be broken out by each sub-task within the NASA HyTEC CMC contract. The intent of this section is to review the goal of each task, a summary of the key design features, manufacturing plans, and a review of the task's schedule performance. This section will serve as a review of how the tasks evolved from the initial plan at the beginning of the contract and the resulting execution of the work. The contents of this section will serve a high-level summary of describing the tasks but will not delve into the details. Further details to the design methodology and analysis will be found in the appropriate Critical Design Review (CDR) and details of the individual test plans can be found within the appropriate Final Test Plan and Test Readiness Reviews.

3.1 TASK 2.1 CMC DURABILITY TESTING

3.1.1 Task Overview

The objective of Task 2.1 of the HyTEC Phase 1 CMC contract was to complete and analyze laboratory scale testing that induced degradation mechanisms which are representative of a commercial engine mission in an accelerated test environment. Key learning included the interaction of well-understood Ceramic Matrix Composite (CMC) lifing mechanisms when operating in a cyclic environment. Results will be used to improve the capability of the P&W lifing model and as a basis for interpreting CMC degradation that occurs in the HPTC rig testing in Task 2.3, in support of validation of the vane design in that task.

Improvements in the lifing model will support successful achievement of Technical Performance Measure (TPM) #3 – maximum use temperature at state-of-the-art life - which supports successful achievement of Key Performance Parameter (KPP) #4: durability, measured in operating hours between major refurbishments. Additionally, the CMC durability testing task will support vane trailing edge life evaluation, which is TPM # 4. TPM #4 supports KPP #6: HPC Exit Corrected Flow.

3.1.2 Manufacturing Plan and Test Execution

Ninety-nine (99) tensile dogbones were machined from nine (9) Pratt & Whitney Gen 1.2 SiC/SiC CMC panels. This number includes spares to recover from invalid tests. The specimen geometry was modified from ASTM C1275 Fig. X2.3 and accounted for the unit cell size of the weave architecture. After machining, all specimens were sealed with a thin coat of CVI SiC to prevent oxygen ingress through cut edges during exposure.

A modified version of the mission cycle discussed in Section 2 was developed to: (i) simplify test conditions; and (ii) mitigate specific concerns about the material. The first modification was due to the inability to rapidly ramp the temperature between test points. To avoid spending a significant proportion of the exposure cycle ramping between test points, the cycle was simplified to two temperature-duration pairs: 15 minutes in the crack sealing regime (point A in Fig.1, corresponding to T1 for approximately the combined duration of takeoff and climb in Fig. 2) and 105 minutes in the pesting regime (point B in Fig. 1, corresponding to T3 for an extended cruise exposure). In this way the proportion of time spent ramping between test points was kept below 20% of the total exposure time. The second modification was to reduce the exposure stress at the takeoff condition to match that of the cruise condition. The material was not expected to be able to sustain a net-section stress of the predicted takeoff conditions for long durations. However, the stress state at cruise still lies above the room temperature matrix cracking stress of the material and allows for investigation of the mechanisms discussed in Section 2.

Creep and fatigue testing was performed in accordance with ASTM C1337 at Cincinnati Testing Laboratories. All testing was in an air environment on servo-hydraulic test frames. Each frame is equipped with a multi-zone furnace to maintain uniform temperature over the gage section of the tensile coupon. Strain is measured by extensometer during the exposure. Each test begins with a short soak at the target temperature to establish thermal equilibrium prior to loading the specimen to the target load. Specimens are exposed continuously for the intended test duration. In the event of a power or mechanical system failure during exposure, a spare was used to duplicate the test.

Isothermal, isostatic creep testing

The purpose of this testing was to set the baseline response of the CMC to exposures in the pesting and crack sealing temperature regimes. Comparison with cyclic exposures will indicate whether combined mechanisms are beneficial or detrimental to material performance. The baseline isothermal, isostatic test conditions are summarized in Table 1. Pesting conditions (T3) are examined for durations ranging from 20-500 hours, while crack sealing conditions (T1) are examined for durations ranging from 20-100 hours. For the 20 hour exposures, residual tensile properties are not measured so that the specimens may be characterized in the as-exposed condition. For longer exposures, the specimens are tested according to ASTM C1275 at room temperature following exposure to measure the residual tensile properties.

Table 1. Isothermal, isostatic creep test summary

Temperature	Load	Exposure duration (hrs)	Residual properties measured	Specimen count
T1	P1	20	N	2
T1	P1	100	Y	6
T3	P1	20	N	2
T3	P1	100	Y	6
T3	P1	500	Y	6

Isothermal, cyclic thermal creep testing

The purpose of this testing was to examine the interaction between oxidation mechanisms by cycling between pesting and crack sealing thermal conditions. Specimens were exposed to the modified mission cycle described previously for a set number of cycles of fifteen (15) minutes at T1 and one hundred five (105) minutes at T3: 9 (~20 hours); 43 (~100 hours); or 214 (~500 hours). The details of testing are summarized in Table 2. For the 20h exposures, residual tensile properties are not measured so that the specimens may be characterized in the as-exposed condition. For longer exposures, the specimens are tested according to ASTM C1275 at room temperature following exposure to measure the residual tensile properties.

Table 2. Isostatic, cyclic thermal creep test summary

Temperature	Load	Exposure duration (cycles)	Residual properties measured	Specimen count
T1, T3	P1	9	N	2
T1, T3	P1	43	Y	6
T1, T3	P1	214	Y	6

Cyclic thermal fatigue testing

The purpose of this testing was to examine a special case of interacting degradation mechanisms. In the event of the formation of a low melting point glass at a crack tip, re-loading of a specimen may have different effects depending on whether the glass is rigid or softened. This exposure follows the same cycle described in the isothermal, cyclic thermal creep testing section with the addition of a thermal and mechanical cycle following the one hundred-five (105) minutes T3 exposure. At this time the temperature is reduced to an idle condition (point C of Fig. 1, corresponding to T4 of Figure 2) and the load is reduced to P2.

After a brief equilibration, the specimens are reloaded to the takeoff condition in one of two ways. In the first, termed “load first”, the specimen is reloaded to P1 prior to heating to T1 – this applies load to glass at the crack tip in the cold state. In the second, termed “temperature first”, the specimen is heated to T1 prior to reloading to P1 – meaning that the glass at the crack tip is loaded in a softened state.

Specimens were exposed to forty-three (43) fatigue cycles (~110 hours) to correspond to the cyclic thermal creep testing. The additional thermal excursion to T4 extends the length of the cycle by ~10%. The details of testing are summarized in Table 3. The specimens are tested according to ASTM C1275 at room temperature following exposure to measure the residual tensile properties.

Table 3. Cyclic thermal fatigue testing

Temperature	Load	Exposure duration (cycles)	Reload sequence	Residual properties measured	Specimen count
T1, T3, T4	P1, P2	43	Load first	Y	6
T1, T3, T4	P1, P2	43	Temperature first	Y	6

Numerical oxidation model

The numerical oxidational model combines the micro-mechanical model of Callaway & Zok 2020 with oxidation degradation mechanisms of TAP et al 2019. For the micro-mechanics, the model considers individual filaments in the loading direction with a homogenized matrix comprising transverse filaments, porosity, and SiC matrix. Individual filaments spanning the full width of the test geometry are split into small segments and randomly assigned Weibull strengths.

Similarly, the matrix is split into small segments and assigned Weibull strengths from a separate distribution. Four input parameters govern these strengths: the Weibull modulus and the Weibull reference strength for both fiber and matrix. The sliding stress is the fifth model input which

governs the slip lengths and crack opening displacements (COD). The five (5) parameters are obtained from calibration to room temperature tensile testing and fiber push-in testing (sliding stress).

For the oxidation degradation portion of the model, governing equations from TAP are incorporated into the micromechanics model to mathematically describe the inward diffusion of oxidants down matrix cracks and subsequent attack of the interface coating and fiber resulting in a degradation of fiber strength. Two key temperature-dependent parameters are needed for this portion of the model: oxidation kinetics of the SiC matrix and strength degradation of the fiber. The former is well described by Deal-Grove oxidation laws and values from the literature are used [Collier et al. 2022]. The latter requires a fit of experimental residual strengths after isothermal exposures at various temperatures. The isothermal 100-hour exposures at T1 and T3 were used for fitting this parameter. This homogenized parameter depends on the complex oxidation behavior of the IFC and the fiber. Therefore, the parameters used in this study are unique to the proprietary IFC system.

With this calibration, the model can simulate isothermal, thermal cyclic, and fatigue tests. The key time-dependent mechanisms at play in this model are COD, crack face oxidation leading to crack sealing, and fiber strength degradation. Key model outputs are the time at which cracks seal and the residual stress-strain response. Creep, which may occur at T1, is not included in this model. Additionally, the hypothesized mechanism related to reloading a solidified versus molten glass is not accounted for in this model. Normalized results of the model are presented in the Results and Discussion section below.

3.1.3 Results and Discussion

Post-Test Analysis

All specimens were photographed after testing to document the location of failure. Select specimens (1-2) from each exposure condition were assigned for more detailed characterization. Longitudinal sections from the gage section of all selected specimens were also mounted in epoxy, polished, and imaged using a Phenom XL scanning electron microscope (SEM). Selected specimens that were tested to failure were also sectioned and mounted for fractography of the failure surface using a Phenom XL scanning electron microscope (SEM).

A subset of the longitudinal sections was then sent to the University of Connecticut for higher quality imaging of oxidized regions of the material. On these specimens, surface cracks were located from the initial SEM micrographs and areas where those cracks intersect axial fibers were identified. These regions were polished using a focused ion beam (FIB) and subsequently imaged by SEM.

3.1.3.1 Isostatic creep testing

Isothermal, isostatic creep testing

The testing described in Table 1 was completed successfully with all specimens surviving the target exposure time. Specimens exposed to T3 were expected to see pesting conditions, with degradation of material properties over the duration of the exposure. Figures 8 and 9 show the residual tensile properties at load P1 and temperature T3 for one hundred (100) hours and five hundred (500) hours, respectively. In both cases the material retains composite behavior after exposure, but strain to failure falls with increasing exposure time.

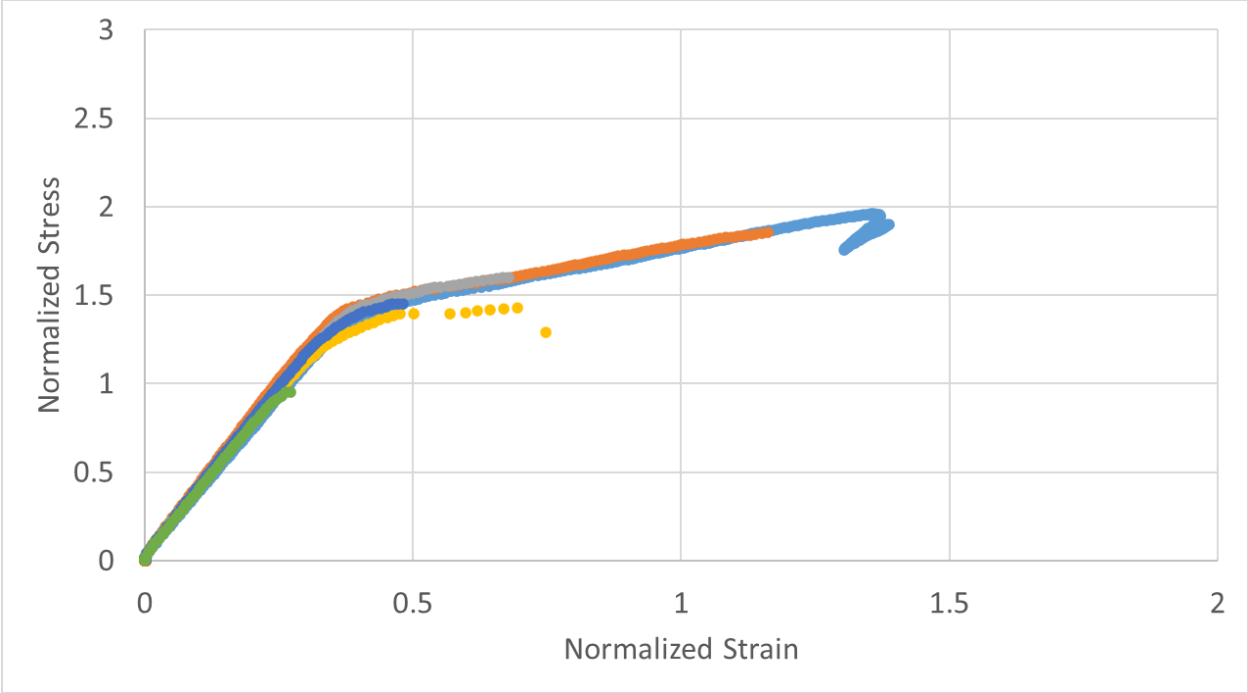

Figure 8. Residual tensile behavior of specimens exposed for 100 hours at load P1 and temperature T3

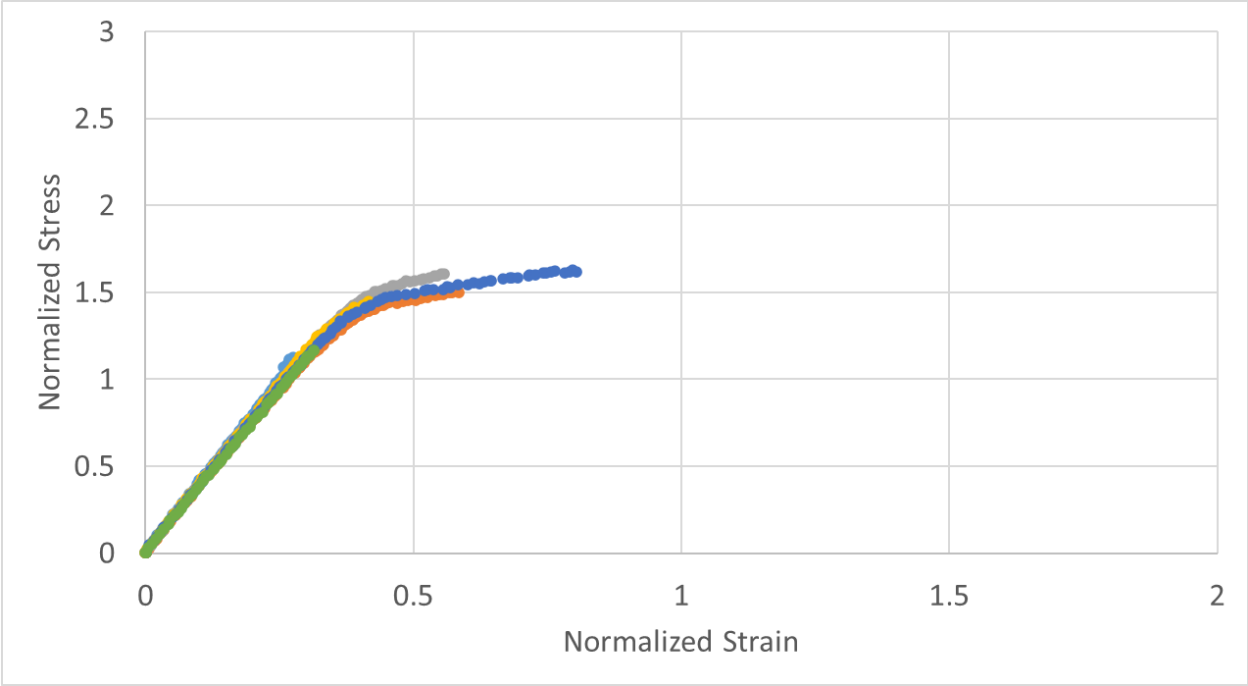

Figure 9. Residual tensile behavior of specimens exposed for 500 hours at load P1 and T3.

Specimens exposed to T1 at load P1 are expected to be in a regime where matrix cracks may seal with oxide. Figure 10 shows the post-exposure tensile behavior of specimens exposed for 100 hours. The strain to failure of these specimens exceeds those of specimens exposed at T3, consistent with expectations.

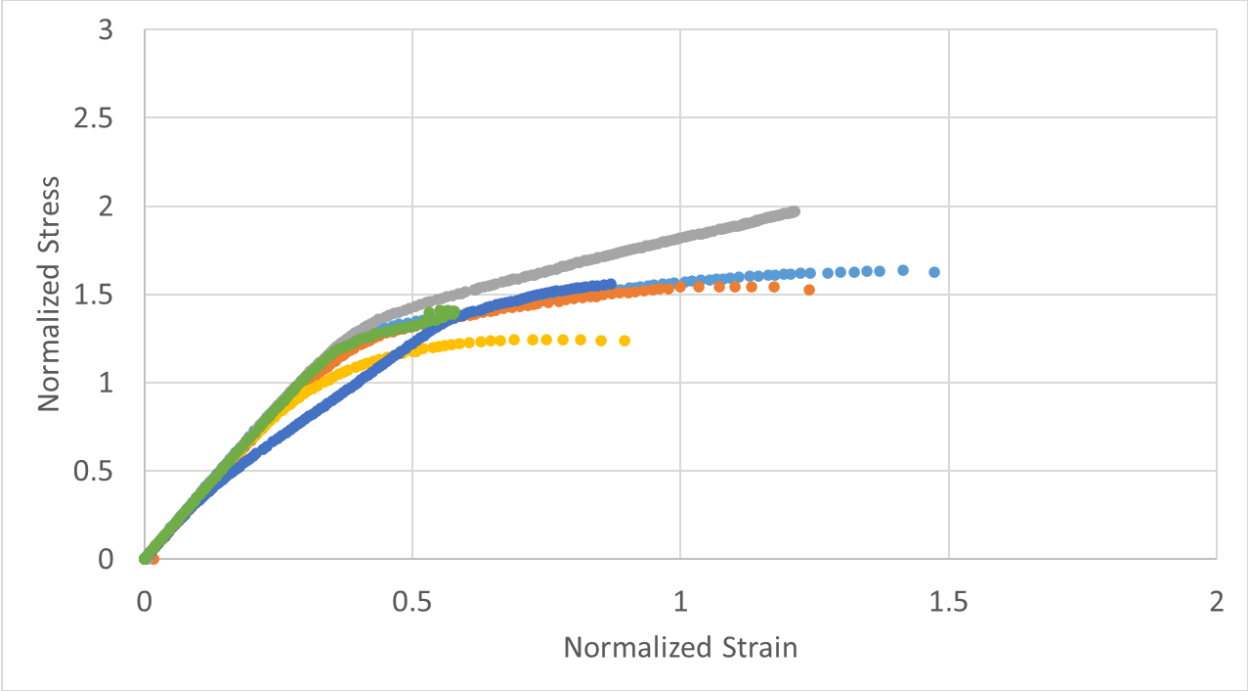

Figure 10. Residual tensile behavior of specimens exposed for 100 hours at load P1 and temperature T1.

Normalized creep strain of the 100h exposures is shown in Figure 11. As expected based on Figure 1, exposure at T1 results in substantially higher total creep strain than exposure at T3. This is a cause for concern even if the pesting phenomenon is avoided, however for these durations creep doesn't lead to failure.

Each of the three isostatic exposures had corresponding tests interrupted at twenty (20) hours that were subsequently mounted and polished to observe the extent of crack face oxidation. All three conditions did have observable crack face oxidation over this period. The measured values were used to inform the oxidation model of this system.

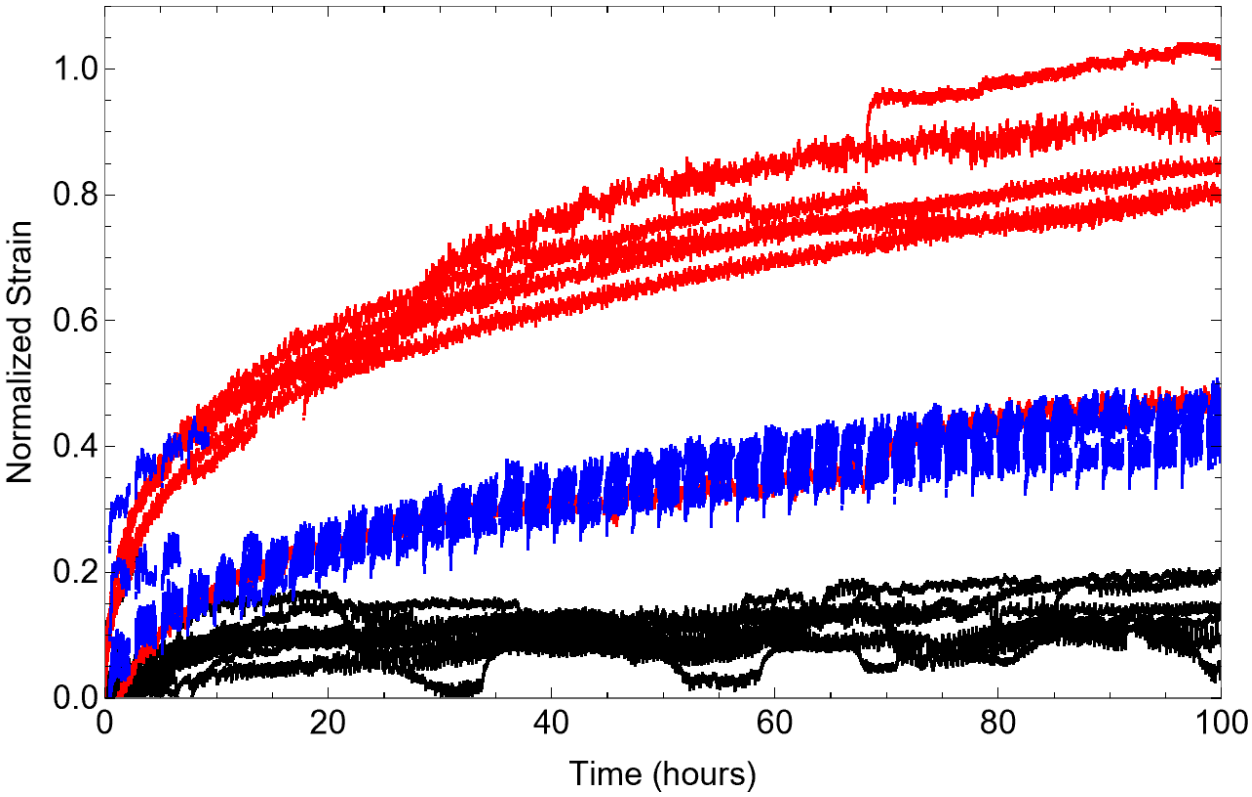

Figure 11. Creep strain for 100 hours isostatic (P1) exposures at: T3 (black); T1 (red); and cyclic conditions (blue). Note that mechanical strain from loading, and thermal strain from heating, are excluded from this plot. Additionally, strain is only plotted for the T3 dwell portions of the cyclic exposure.

Isostatic, thermal cyclic creep testing

The testing described in Table 2 was completed successfully with all specimens surviving the target exposure time. Figure 12 shows the residual tensile response of specimens exposed to thermal cyclic creep at load P1 for forty-three (43) cycles. Figures 13 and 14 compare residual tensile strength and residual strain to failure using standard box plots, respectively, for this exposure and the two (2) one hundred (100) hour isothermal exposures. While residual tensile strength is not strongly impacted by exposure type, the residual strain to failure following cyclic exposure exceeds that of the one hundred (100) hours T3 pesting exposure and lies closer to that of the one hundred (100) hour T1 crack sealing exposure. This is consistent with the theory of a beneficial interaction between the crack sealing and pesting mechanisms. A summary of two-population t-tests is shown in Table 4. None of the populations are significantly different at a p=0.05 level, however, the p-value for failure strain between T3 and any other condition is much lower than observed for the T1-Cyclic pair or for any of the residual strength pairs.

Figure 11 shows the creep response of cyclic exposure. While short dwells at T1 result in higher total creep strain than isothermal exposure at T3, substantially lower creep strains are observed in cyclic exposures than isothermal exposures at T1. Total creep strain for one hundred (100) hour cyclic exposure is consistent with the creep strain observed for the cumulative time spent at T1 (~12.5 hours).

Table 4. Summary of paired t-tests for equivalence of residual strength and failure strain of isothermal exposures

Exposure pair	Exposure duration (hrs)	p-value (residual strength)	p-value (residual failure strain)
T1 vs T3	100	0.697	0.167
T1 vs Cyclic	100	0.751	0.731
T3 vs Cyclic	100	0.894	0.265
T3 vs Cyclic	500	0.973	0.134

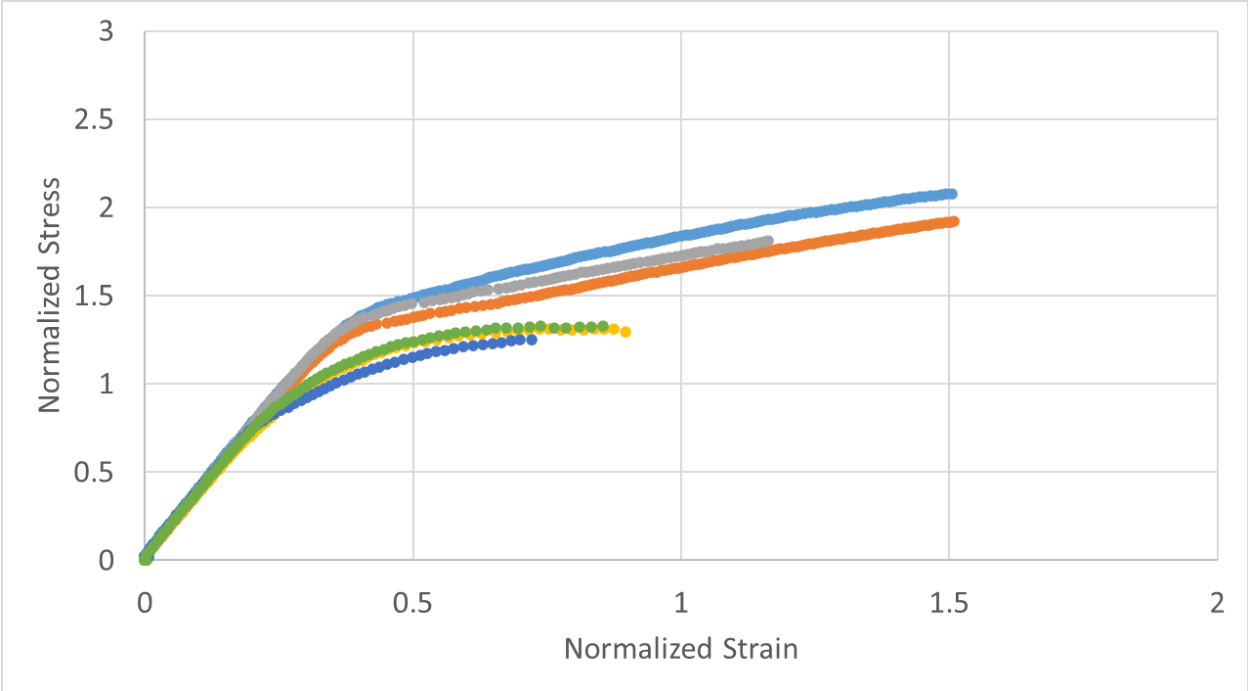

Figure 12. Residual tensile behavior of specimens exposed for 43 cycles at load P1 and cyclic thermal loading at T1 and T3.

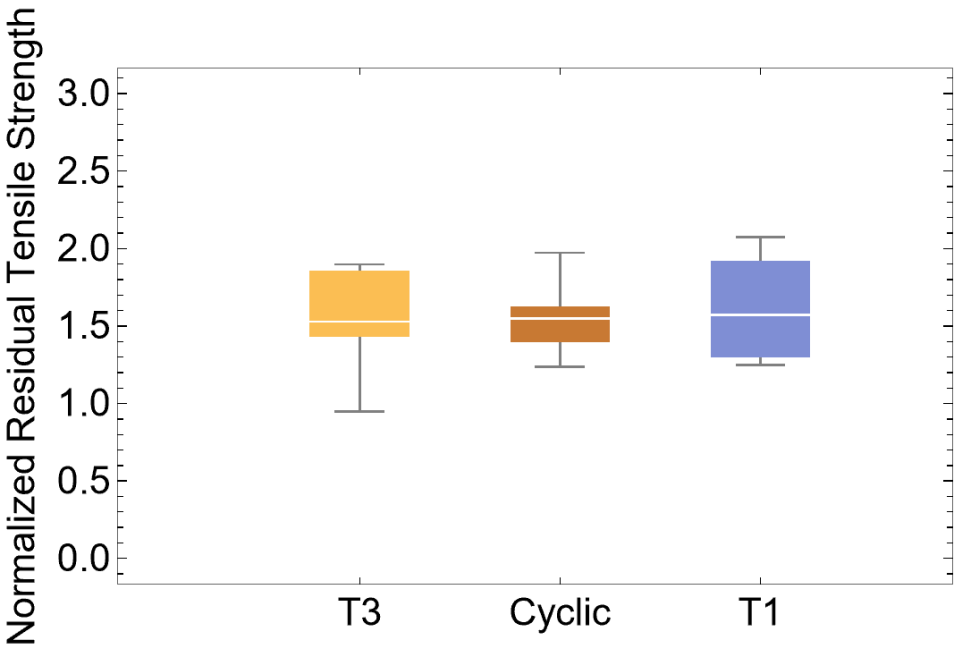

Figure 13. Residual tensile strength for three ~100 hour creep exposures: T3 isothermal; T1 isothermal; and thermal cyclic.

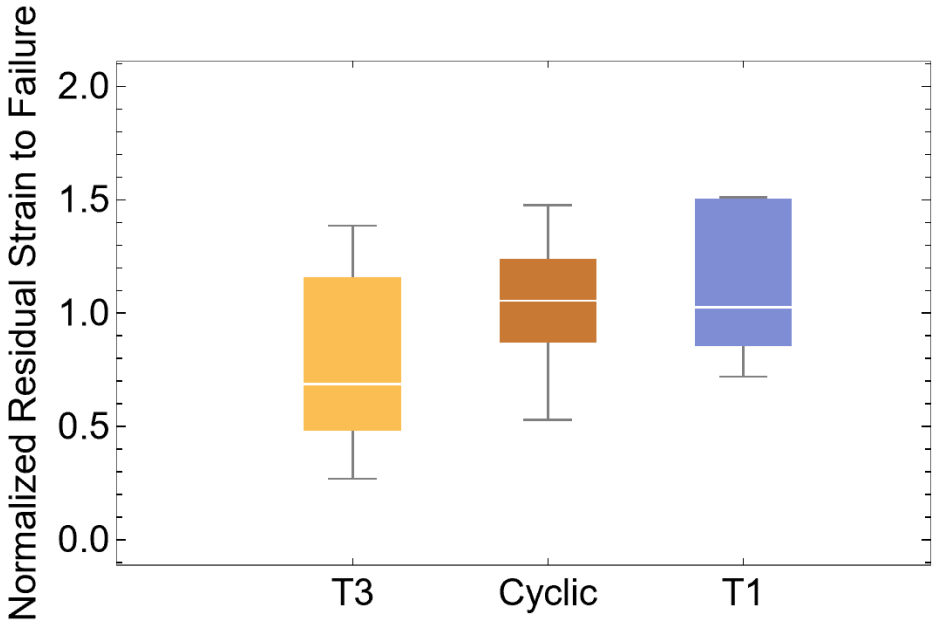

Figure 14. Residual strain to failure for three ~100 hour creep exposures: T3 isothermal; and thermal cyclic, and T1 isothermal.

Longer duration tests were performed with the expectation that any beneficial interactions from cyclic loading would have a more significant effect with increased exposure time. Figure 15 shows the residual tensile response of specimens exposed to two hundred fourteen (214) cycles of thermal cyclic loading between T1 and T3 at load P1. Figures 16 and 17 compare the residual failure strength and residual strain to failure using standard box plots, respectively, between thermal cyclic exposures and corresponding 500h T3 isothermal exposures. Once again the differences in residual tensile strength are minimal, but the difference in residual strain to failure is significant – the difference in means is similar to what is observed for 100h exposures, indicating that the benefit of cyclic loading does persist over time.

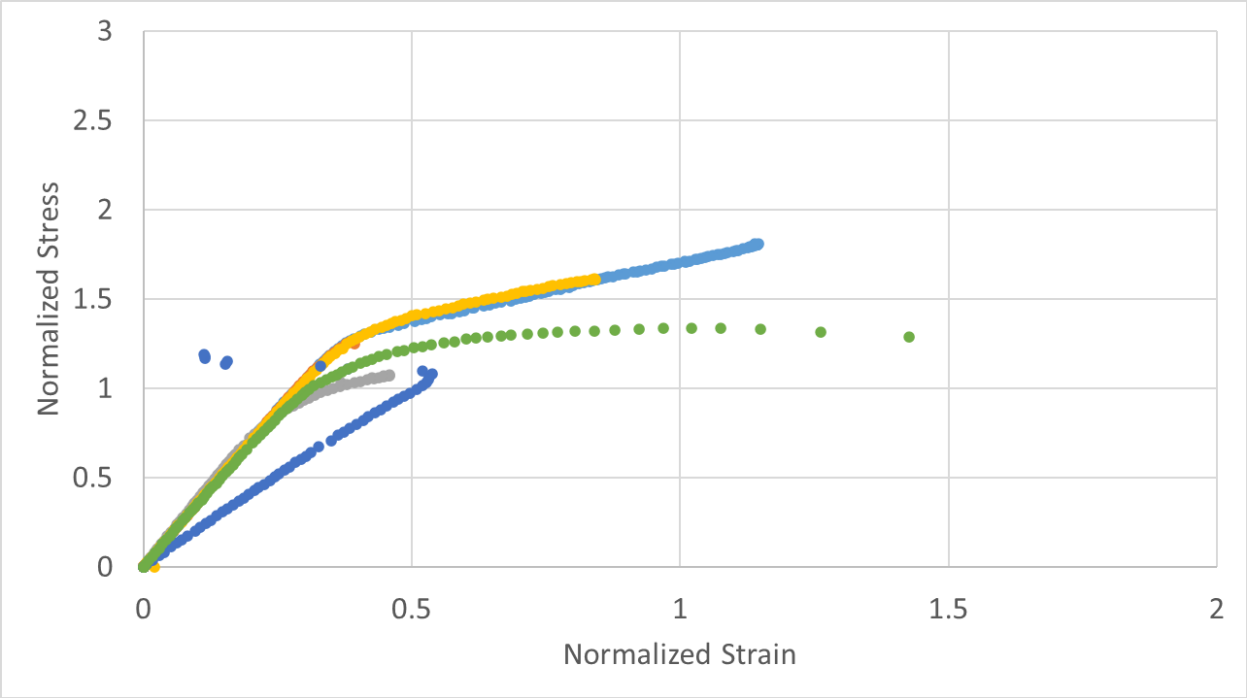

Figure 15. Residual tensile behavior of specimens exposed for two hundred fourteen (214) cycles at load P1 and cyclic thermal loading at T1 and T3. (Note: Failure strain from anomalous specimen not included in population summaries)

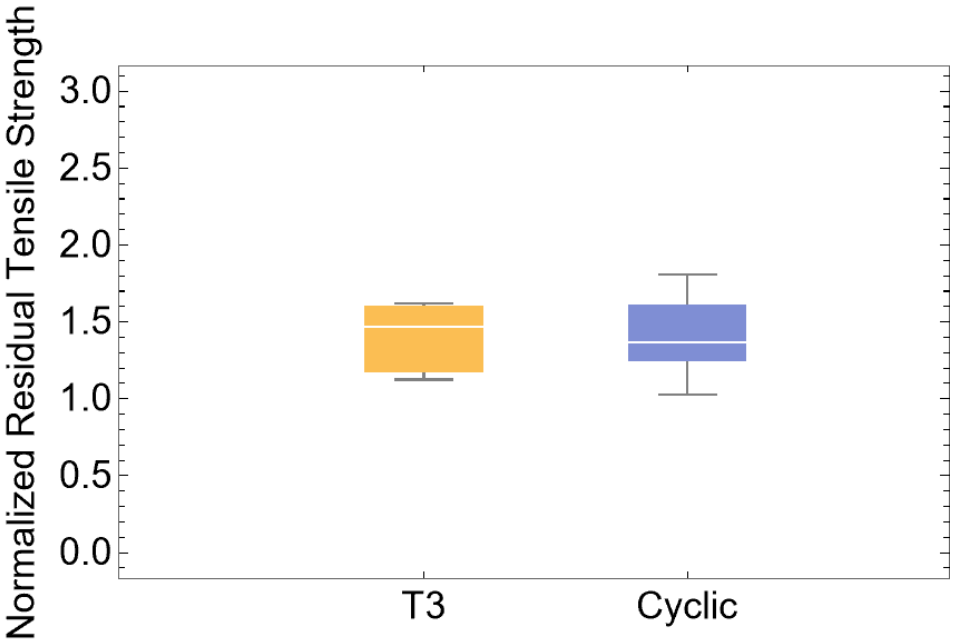

Figure 16. Residual tensile strength of specimens exposed to: 500h isothermal exposure at T3 and P1; and specimens exposed to thermal cyclic loading for two hundred fourteen (214) cycles at load P1.

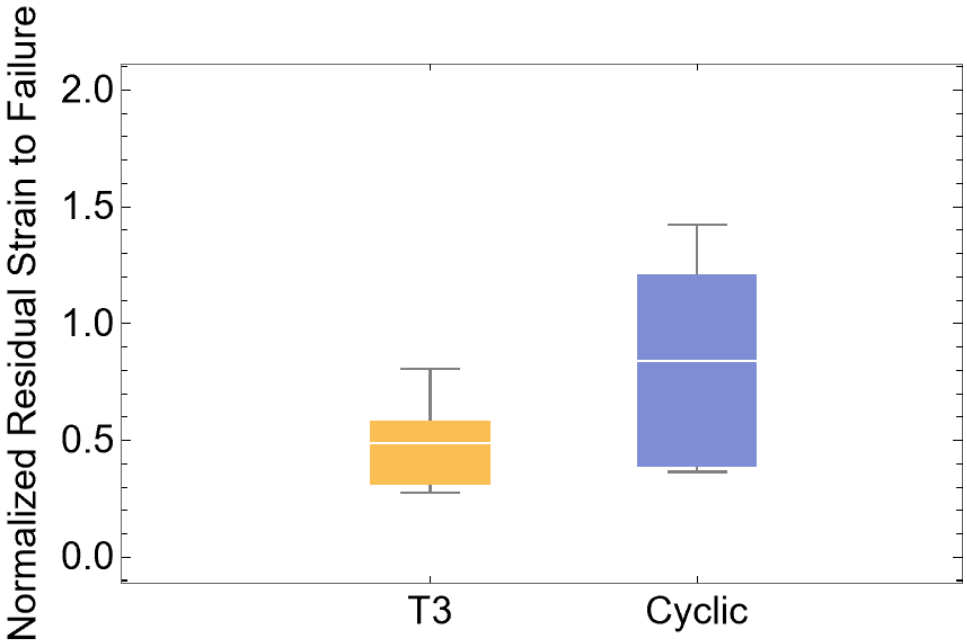

Figure 17. Residual strain to failure of specimens exposed to: 500h isothermal exposure at temperature T3 and load P1; and specimens exposed to thermal cyclic loading for two hundred fourteen (214) cycles at load P1.

3.1.3.2 Thermal cyclic fatigue testing

An additional load and thermal cycle were added to the thermal cyclic condition to explore whether glass formation near the fiber-matrix interface could be detrimental to material performance. If the glass is soft when load is increased the energy at the crack tip may be dissipated, however, if the glass is rigid, a crack may form in the glass and propagate through the adjacent fiber. Experiments were performed to explore each of these scenarios for a duration of forty-three (43) thermal cycles.

Figure 18 shows the residual tensile response of material exposed to thermal cyclic fatigue where the load was increased while the material was at temperature T1 (“temperature first”). Figure 19 shows the residual response of material exposed to thermal cyclic fatigue where the load was increased while the material was at temperature T4 (“load first”). Comparisons of residual failure strength and residual strain to failure standard box plots are shown in Figures 20 and 21, respectively. Notably, the “load first” condition was the only exposure condition in this test campaign where specimens failed prior to reaching the runout condition – 50% of specimens failed in less than 10 cycles. For specimens that reached the runout condition of forty-three (43) cycles, there was no meaningful difference in residual failure strength or residual strain to failure for the two loading conditions. This is suggestive of crack propagation during the “load first” condition.

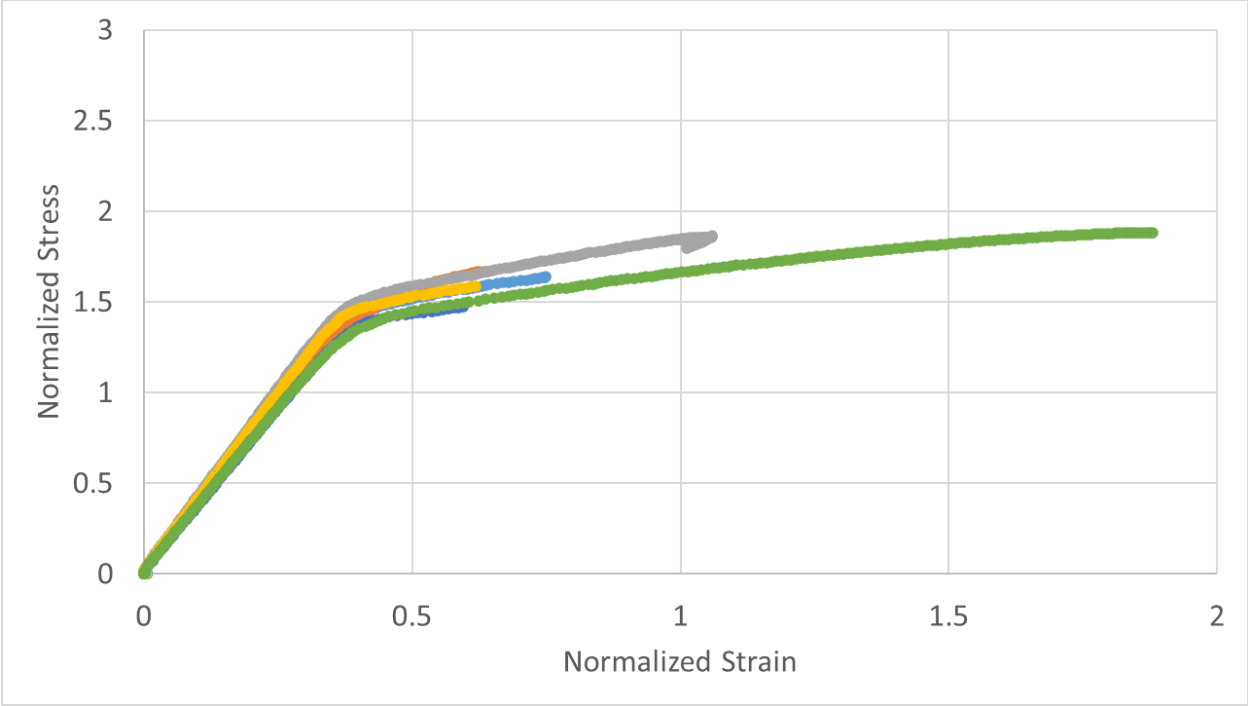

Figure 18. Residual tensile behavior of specimens exposed for forty-three (43) cycles of fatigue loading where the temperature was increased before load

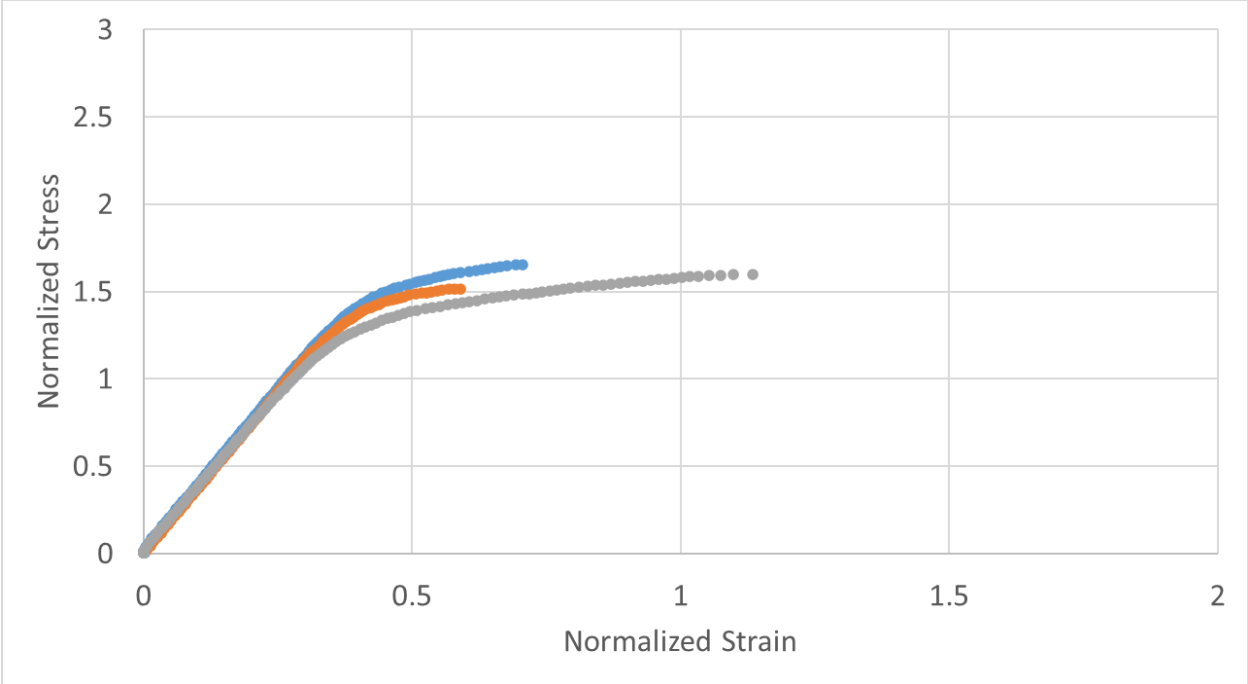

Figure 19. Residual tensile behavior of specimens exposed for forty-three (43) cycles of fatigue loading where the load was increased before temperature. Note that only three of six specimens survived the exposure condition.

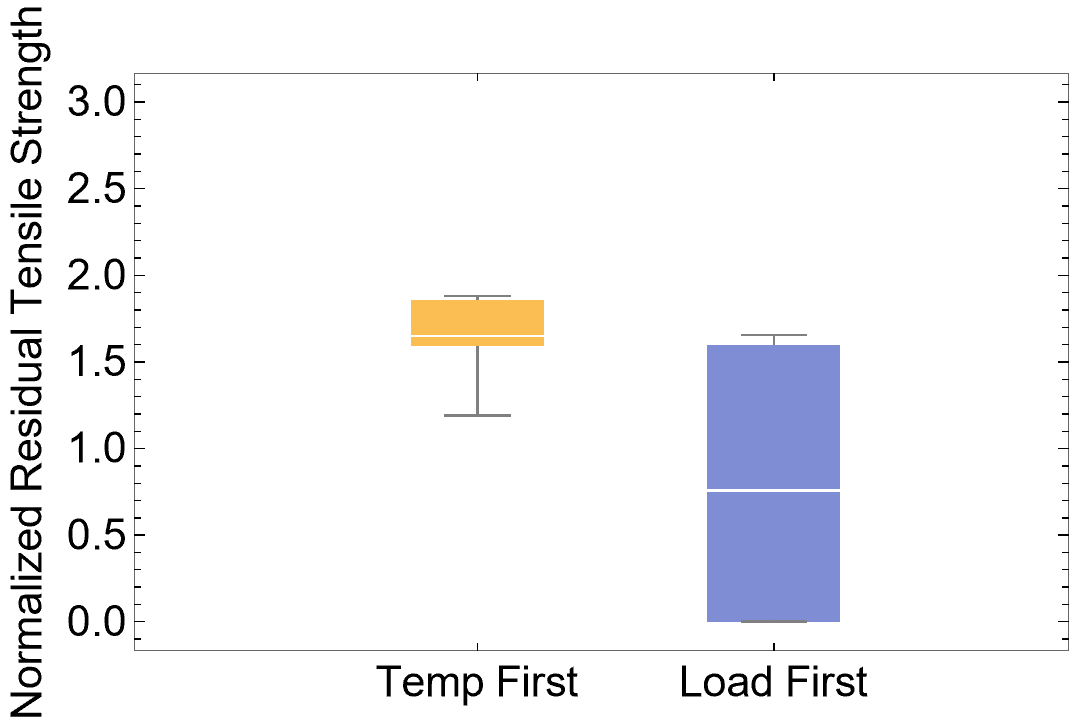

Figure 20. Comparison of residual tensile strength for specimens exposed to forty-three (43) cycles of fatigue in the “temperature first” and “load first” conditions.

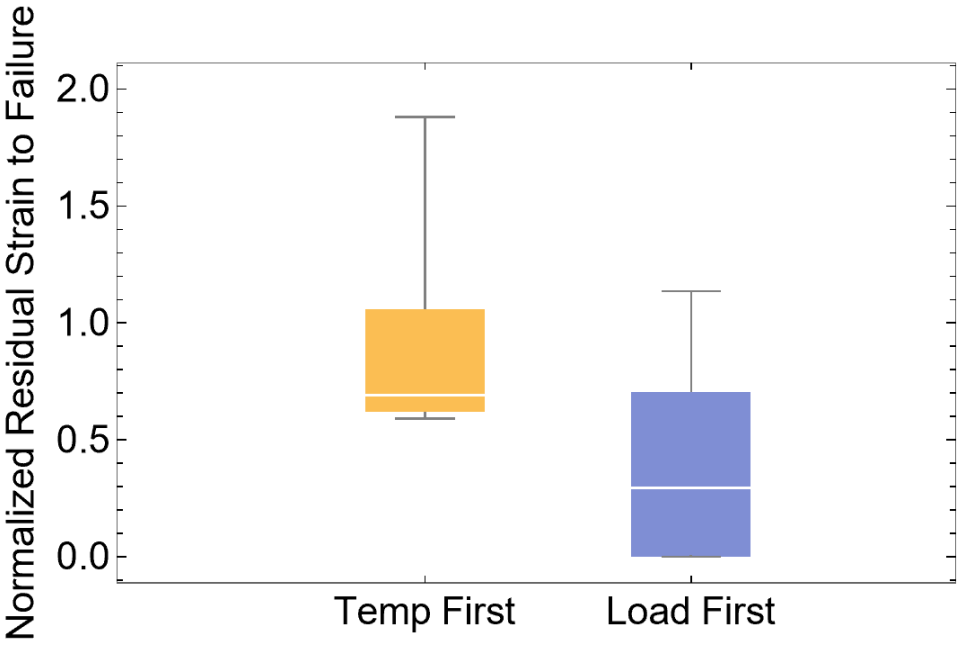

Figure 21. Comparison of residual strain to failure for specimens exposed to forty-three (43) cycles of fatigue in the “temperature first” and “load first” conditions.

The mechanism for early failures in the “load first” condition was further investigated with SEM characterization. For specimens that failed during the exposure condition fractography reveals extensive regions of flat fracture, with fibers failing coplanar to the matrix (Figure 22). This is indicative of an oxidative degradation mechanism and suggestive of crack propagation during exposure. In contrast, the “temperature first” fracture surfaces – as well as all isostatic load conditions – show limited fiber pullout only near the surfaces of the specimen (Figure 23).

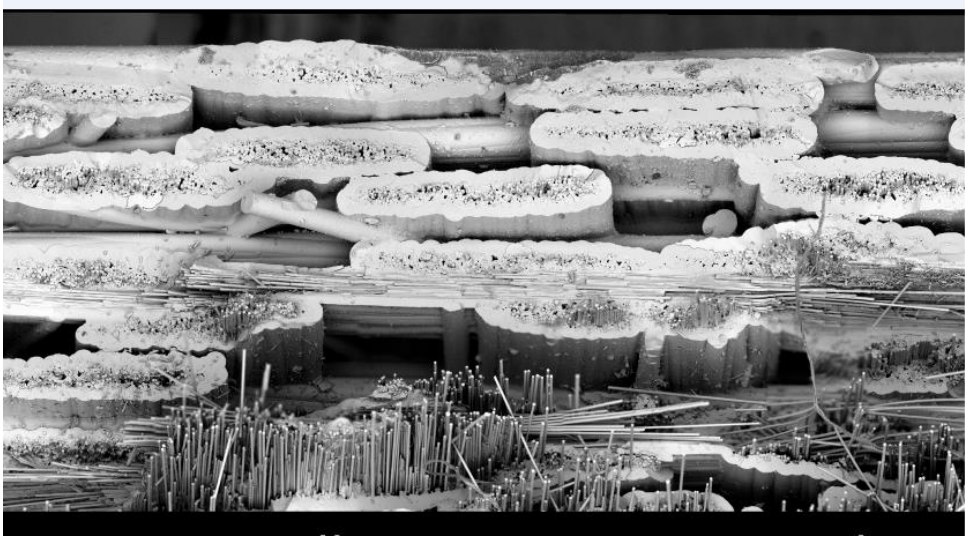

Figure 22. Fracture surface of specimen exposed to “load first” condition that failed during exposure.

Figure 23. Fracture surface of specimen exposed to “temperature first” condition.

One “load first” specimen that survived the exposure and tested for residual properties was mounted and polished for detailed characterization. One location was identified where a surface crack intersected axial fibers (Figure 24). This crack is clearly filled with oxide, indicating that it formed during the thermal cycling exposure rather than during the residual tensile test. Ahead of the crack several fibers have cracked near the plane of the matrix crack, a feature not observed in other specimens that were not exposed to isothermal T1 conditions. It is hypothesized that this crack was small enough to rapidly seal, and prevented early failure as observed in other specimens exposed to this condition. This feature is consistent with the theory of crack propagation through fibers in the presence of a rigid glass, although it does not confirm the mechanism. This observation warrants further study and will be monitored during the execution of Task 2.3.

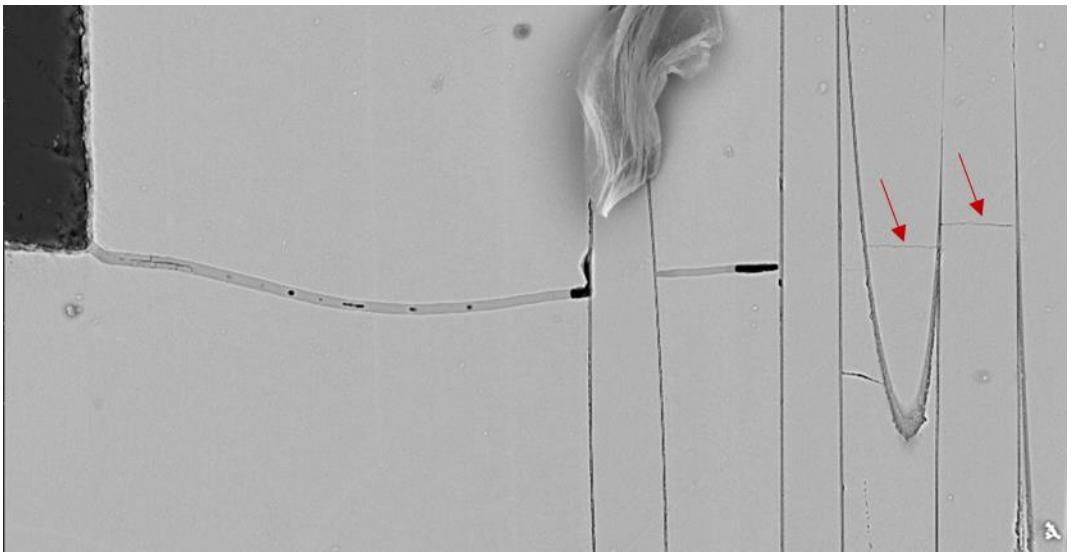

Figure 24. SEM micrograph of “load first” specimen that hit the runout condition and was tested for residual tensile performance. Red arrows indicated cracked fibers ahead of matrix crack. Specimen surface is at left edge of image.

3.1.3.3 Modeling oxidative degradation

Simulations of the test conditions described in the above sections were performed with the numerical oxidation model. For simulation results described below, “cyclic” refers to isostatic thermal cycling between T1 and T3 whereas “fatigue” refers to cyclic thermal fatigue testing described in Table 3. In the fatigue simulation, the “load first” and “stress first” conditions are identical as there is no degradation mechanism implemented in the model to distinguish these different conditions. Stress and strain results are normalized in the same manner as experimental results. For each condition, six simulations were run. The randomized Weibull strengths assigned to the fiber and matrix segments adds a stochastic element to the simulations.

Simulations were run for one hundred (100) hour runouts, forty-three (43) cycles, or until all matrix cracks were sealed. Once sealed, the damage mechanism of fiber and IFC oxidation halts, and residual strengths degrade no further with time. As shown in Figure 25, cracks in all four conditions seal well before the 100 hour or 43 cycle runout condition. At the higher temperature T1, the crack sealing time is less than 1 hour. At the lower temperature T3, this time is about twelve (12) hours. It is important to note that the crack sealing time is sensitive to the load. COD increases with applied stress; thus, crack sealing time also increases with stress. For the cyclic and fatigue conditions, cracks seal within the first (1st) two (2) or three (3) cycles. The majority of the matrix oxidation occurs during the fifteen (15)-minute increments at T1. Crack sealing in fatigue conditions is slightly slower than that of cyclic conditions due to the drop down to T4 where SiC oxidation kinetics are sluggish at this low temperature. Additional isothermal simulations were done at T4 and crack sealing did not occur even after a 2000 hour runout.

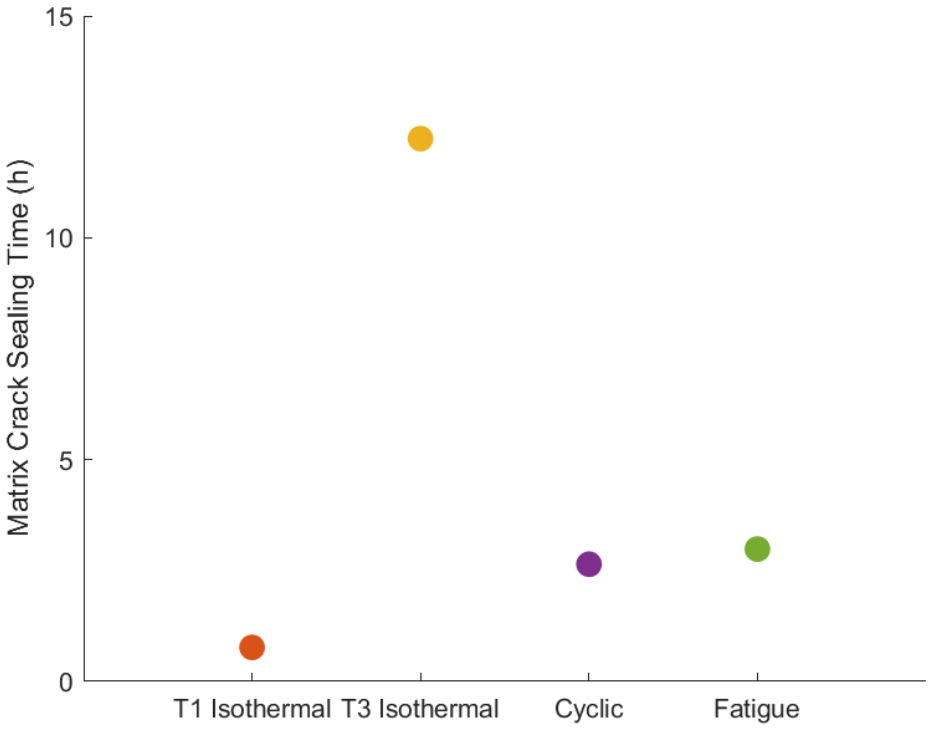

Figure 25. Simulated crack sealing time for the four test conditions.

After runout or crack sealing, simulations underwent residual tensile testing. A representative residual stress-strain response is shown in Figure 26 for each condition. The simulated tensile response up to failure is similar for the various conditions; however, the different exposures reduce the residual strength and failure strains. These values are shown in Figures 27 and 28. The residual strengths and failure strains are inversely correlated to crack sealing time. The longer the cracks are unsealed, the more time for the fiber and IFC to oxidize and degrade. The residual strengths of the T1 isothermal, cyclic and fatigue conditions are slightly higher in the simulations than in the experiments. This overestimate of strength may be due to the lack of creep degradation in the model. Significant creep strain is observed during isothermal T1 experiments but not at T3. Similarly, the residual failure strains are overestimated in the model. Both model and experiments show similar behavior in the relatively low residual failure strain of the isothermal T3 condition.

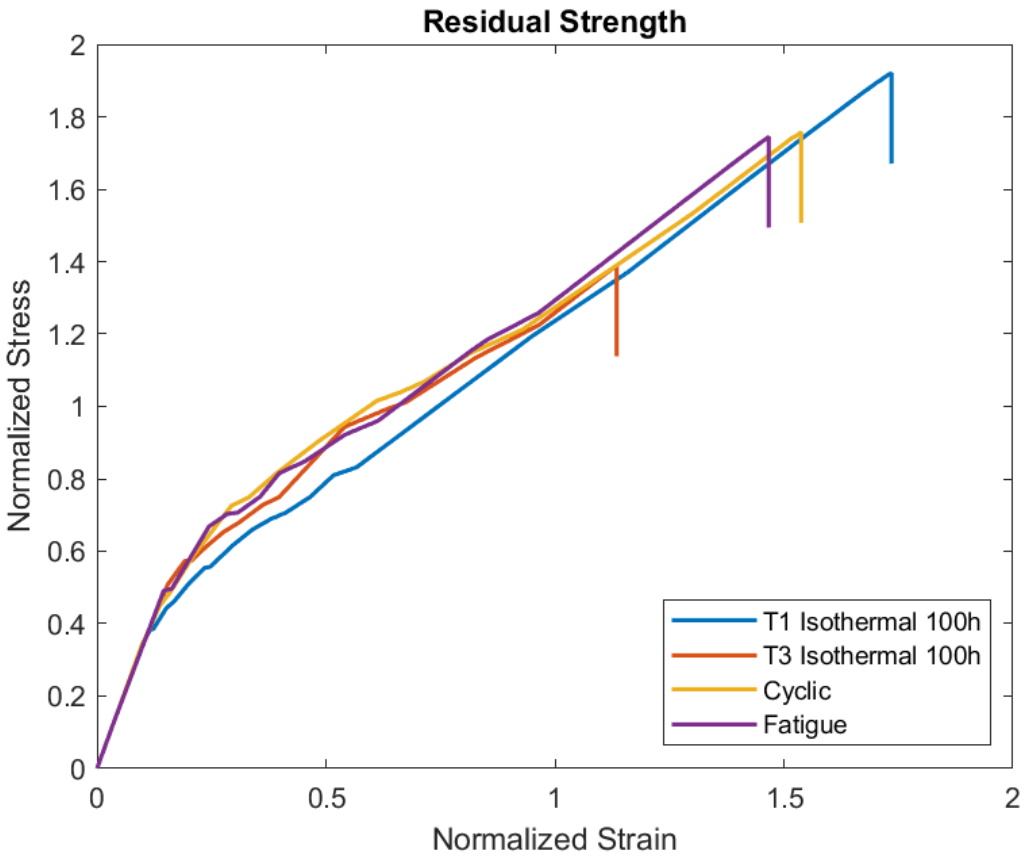

Figure 26. Simulated residual stress-strain response

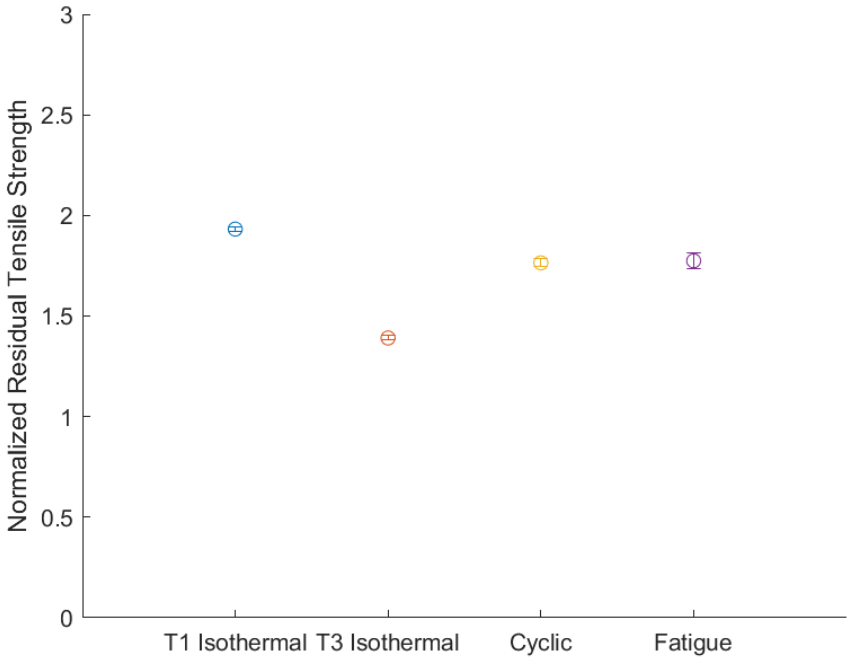

Figure 27. Simulated residual tensile strengths. Circles denote the mean with error bars representation +/- 1 standard deviation

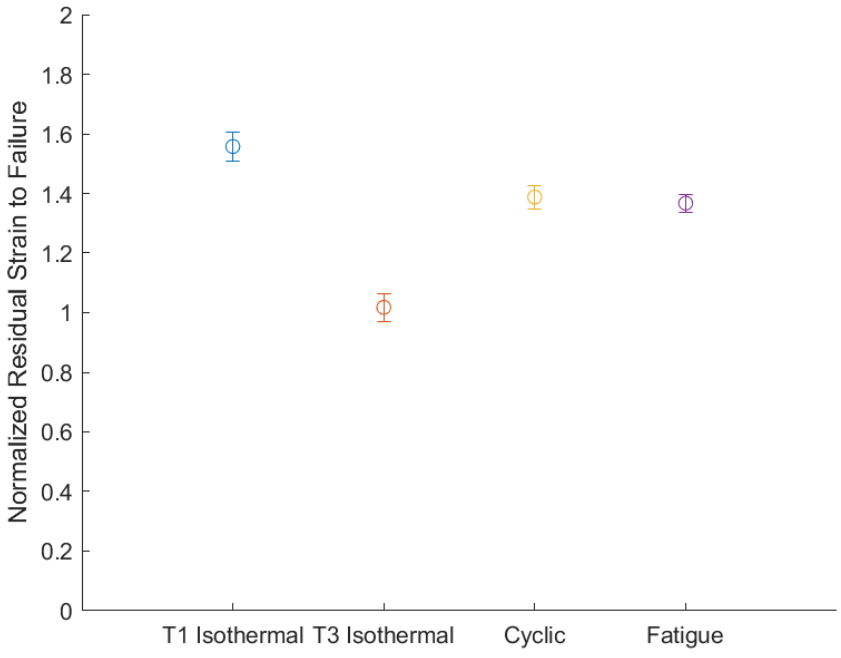

Figure 28. Simulated residual failure strains. Circles denote the mean with error bars representation +/- 1 standard deviation

3.1.4 CONCLUSIONS AND KEY TAKEAWAYS

- In isostatic testing, short thermal cycles above the pesting regime are shown to improve residual tensile properties relative to isothermal testing in the pesting regime at durations of 100 hours and 500 hours.
- Mechanical cycling of specimens during thermal exposures is shown to affect failure times of specimens, depending on the sequence of loading.
- Post-test inspection of fatigue specimens indicates significant regions of flat fracture in “load first” specimens that do not survive the exposure condition; evidence of fiber failure is observed ahead of matrix cracks in sister specimens that do survive exposure.
- Simulation results generally align with experimental trends. High temperature exposures rapidly seal matrix cracks and limit degradation, leading to improved residual properties relative to isothermal testing in the pesting regime. An overestimation of retained properties in the simulation is likely due to lack of creep degradation in the model.

3.2 TASK 2.2 ENVIRONMENTAL BARRIER COATING DURABILITY TESTING

3.2.1 Task Overview

The objective of Task 2.2 of the HyTEC Phase 1 – CMC contract was to complete and analyze laboratory scale testing that induced degradation mechanisms which represent course of duty conditions representative of a commercial engine mission in an accelerated test environment. Key learning included the sequence of EBC life-limiting degradation mechanisms leading to failure and the relative ranking of contributing factors. Results will be used to improve the capability of the P&W lifing model and as a basis for interpreting EBC degradation that occurs in the HPTC rig testing in Task 2.3, in support of validation of the vane design in that task.

Improvements in the lifing model will support successful achievement of Technical Performance Measure (TPM) #3 – maximum use temperature at state-of-the-art life - which supports successful achievement of Key Performance Parameter (KPP) #4: durability, measured in operating hours between major refurbishments. Additionally, the EBC durability testing task will support vane trailing edge life evaluation, which is TPM # 4. TPM #4 supports KPP #6: HPC Exit Corrected Flow.

After the initial objectives were met, the HyTEC Phase 1 – CMC contract was modified to increase scope and include Task 2.2.5 to complete and analyze furnace cycle testing (FCT) of P&W EBCs on P&W CVI SiC/SiC CMCs under saturated steam conditions in the NASA Steam FCT rig for comparison to testing that was completed in a similar Steam FCT rig at RTRC under Task 2.2 of this contract. The primary difference between the operation of the two rigs is a faster cycling frequency in the NASA rig. Samples were cycled between the test temperature and near room temperature every hour in the NASA rig, as compared to every 20 hours in the RTRC rig. There are also some differences in the design of the two rigs, but both rigs were designed to test the samples under the same temperature and steam environment. Testing of the P&W EBCs in the NASA Steam FCT rig was completed under Task 2.2.5. The key learning from this task is that the degradation mechanism and progression of the EBC system was the same in both rigs. The rate of damage accumulation was slightly faster in the RTRC rig, presumably due to the difference in cycling frequency.

The second objective of added Task 2.2.5 was to coat and test NASA EBCs on P&W CMCs in the NASA Steam FCT rig and to compare the results to those for the P&W EBCs. Key learning was that in most locations, the NASA EBC exhibited very little damage accumulation after the full FCT Steam test duration. However, in some locations on the samples the large macroscopic surface roughness due to the five-harness satin weave of the P&W CVI SiC/SiC CMC led to poor

adhesion between layers of the NASA EBC. In addition cracks through the NASA EBC occurred in some of these high-roughness locations. This led to local spallation of the NASA EBC and internal oxidation of the CMC in the spalled locations.

3.2.2 Manufacturing Plan and Test Execution

One hundred thirty (130) 1”x1” squares and twelve (12) 1.5” diameter discs were machined from four (4) SiC/SiC CMC flat panels and coated for testing per the plan documented herein. These include spare samples to allow for potential additional testing to leverage lessons learned during execution of the program. Additionally, twenty-four (24) commercially available sintered SiC 1”x1” coupons were coated for testing, with an appropriate number of spares. Nineteen (19) 1”x1” CMC samples were coated and nondestructively and destructively analyzed to determine average thicknesses and surface roughness in the as-coated condition.

The environmental barrier coating that was deposited on the coupons is the P&W Gen 1.2 EBC. After deposition, the bondcoated coupons were sintered to densify the bondcoat and improve adhesion to the CMC.

The topcoat is deposited by air plasma spraying (APS). Since the raw material powder dissociates, and since some SiO2 is lost due to volatilization during the spray process, the as-processed coatings consisted of a mixture of phases. After deposition, the EBC-coated coupons are heat treated to move the topcoat phase composition toward equilibrium.

Fabrication and inspection data for the coupons were reported in the Hardware Inspection Report for this task – CDRL 4.1-2.2-1, dated August 31, 2022. Sources of sample-to-sample variation were discussed in that report. Ultimately that variation did not have a significant effect on the key learning from this task.

Under Task 2.2.5, Forty-eight (48) additional samples were machined from remnants of three (3) SiC/SiC CMC flat planes that had been fabricated under this contract. These coupons were sent to NASA for development coating trials and to coat 24 samples for Steam FCT testing in the NASA rig under Task 2.2.5. Coating of these twenty-four (24) coupons for testing was successful.

3.2.2.1 Testing in Ambient Air

Static ambient furnace testing

Static exposures in an ambient environment were carried out using commercially available box furnaces. The samples used in this testing were 1”x1” coupons machined from P&W Gen 1.2 CVI SiC/SiC panels. No CVI SiC sealcoating of the edges was completed after machining, Coupons were coated with the P&W Gen 1.2 EBC system on one side. Experience to date has shown that the lack of sealcoating on edges and the uncoated back side does not affect test results for ambient furnace cycle testing. The intent of this testing was to identify damage modes and the rate of damage progression under what were expected to be the least damaging conditions since neither thermal cycling nor saturated steam environments were present in this test. Post-test destructive microstructural analysis of samples removed from test after several durations was completed to monitor the evolution of damage.

Table 5 summarizes the planned conditions for static ambient furnace exposures. Samples were tested at the average takeoff temperature (T1), average climb temperature (T2), average cruise temperature (T3), average descent temperature (T4) and average landing temperature (T5) as indicated in Figure 1. Inclusion of the lower test temperatures was to validate the expectation that minimal damage will accumulate at these temperatures, since appreciable portions of the mission time are spent at these temperatures.

For the static ambient furnace testing, at each temperature, all 8 samples were started in the furnace at the same time. Two samples were removed after each of the four exposures listed in Table 5.

Table 5. Test plan for static ambient furnace testing

Temperature	# of samples removed after 25% of total duration	# of samples removed after 50% of total duration	# of samples removed after 75% of total duration	# of samples removed after 100% of total duration
T1	2	2	2	2
T2	2	2	2	2
T3	2	2	2	2
T4	2	2	2	2
T5	2	2	2	2

Ambient furnace cycle testing

Furnace cycle testing in ambient air was carried out using commercially available bottom loading cyclic furnaces from CM Furnaces Inc., Bloomfield, New Jersey with a nominal 1 hour thermal cycle. That cycle consists of a heating ramp, a soak at the target temperature, and a quick cooling ramp with ambient air blown on the samples by a fan. Twenty (20) cycles are completed per day in this test. As such the samples are near or at room temperature for four (4) hours per day.

The samples used in this testing were 1”x1” coupons machined from P&W Gen 1.2 CVI SiC/SiC panels. No CVI SiC sealcoating of the edges was completed after machining, Coupons were coated with the Pratt & Whitney Gen 1.2 EBC system on one side. Experience to date has shown that the lack of sealcoating on edges and the uncoated back side does not affect test results for ambient furnace cycle testing.

The intent of this testing was to provide baseline data for the evolution of the EBC microstructure as a function of cyclic exposure at key temperatures in the notional commercial mission cycle shown in Figure 2. Post-test destructive microstructural analysis of samples removed from test after several durations was used to monitor the progression of damage accumulation.

Table 6 summarizes the ambient furnace cycle testing that was completed. Testing was done at three temperatures – average takeoff temperature (T1), average climb temperature (T2), and average cruise temperature (T3), as indicated in Figure 2. The rationale for the choice of these temperatures is that T1 is the maximum temperature of the mission cycle and large proportions of the total mission cycle time are spent at T2 and T3. Data on damage accumulation rates at these temperatures is necessary input to develop robust lifing models.

At each temperature, two (2) samples were tested for a target duration. Additionally, two (2) samples were tested for 25%, 50%, and 75% of that duration for all three (3) test temperatures, to enable generation of data describing the rate and mechanisms of damage accumulation via post-test destructive analysis. Again, at each temperature, all 8 samples were started in the furnace, then 2 samples were removed after each of the exposures listed in Table 6. Based on P&W experience with this test to date, minimum temperatures during the cooling phase of each thermal cycle will be below 150°C. This ensures that any cristobalite present in the EBC system

will go through the high-to-low transformation temperature of 220°C during cooling and reheating every cycle.

The failure criterion for this test was spallation of twenty (20%) percent or more of the area of the coating from the coupon.

Table 6. Ambient furnace cycle testing completed

Temperature	# of samples removed after 25% of total duration	# of samples removed after 50% of total duration	# of samples removed after 75% of total duration	# of samples removed after 100% of total duration
T1	2	2	2	2
T2	2	2	2	2
T3	2	2	2	2

Static steam furnace testing

Static exposures in a saturated steam environment were carried out using a furnace previously designed at RTRC. The samples used in this testing were 1”x1” coupons machined from P&W Gen 1.2 CVI SiC/SiC panels. No sealcoating of the edges was completed after machining; however, coupons were coated with the P&W Gen 1.2 EBC system on both sides of the samples. The edges of the samples were also manually painted with the bondcoat slurry. Experience to date has shown that this approach avoids having the results of steam furnace cycle testing from being confounded by degradation of uncoated locations on the samples.

The intent of this testing was to compare to the other testing completed in this task to elucidate the relative roles of static vs. cyclic testing and steam vs. ambient environments on the damage accumulation during exposure. Again, post-test destructive microstructural analysis of samples removed from test after several durations was relied upon to develop the output data for this testing.

The same total nominal exposure times at test temperature was used as in the testing described in the above two sections. Table 7 summarizes the planned conditions for static ambient furnace exposures. Only one furnace was available for this test, so P&W only tested at the average takeoff temperature (T1).

Only two (2) samples could be tested at a time. Two (2) samples were planned to be put in the rig at the start of the test. After 33% of the planned test, one sample was planned to be removed and replaced by a second sample that would run for the remaining planned 66% of the test hours.

Table 7. Test plan for static steam furnace testing

Temperature	# of samples removed after 33% of total duration	# of samples removed after 66% of total duration	# of samples removed after 100% of total duration
T1	1	1	1

Steam furnace cycle testing

Furnace cycle testing in a low velocity, ambient pressure, saturated steam furnace was planned using steam cyclic furnaces previously designed and built at the RTX Research Center (RTRC). A schematic and a photograph of the furnace are shown in Figure 29. These furnaces are closed end vertical tube furnaces. As shown in the schematic, the flowing steam environment has a controlled water/oxygen ratio established using mass flow controllers. Alumina tubes are used in this design. Temperature was controlled via a thermocouple located close to the samples. Samples rest on an alumina tube and are raised into and out of the hot zone to accomplish the thermal cycling.

The high temperature soak portion of the thermal cycle was 20 hours, since more rapid cycling would cause damage to the furnace components, reducing the reliability of the test. This unavoidable difference in thermal cycling complicated direct comparison of results from this test to the ambient air furnace cycle testing. However, as described in the static steam furnace testing section, isothermal steam testing with no cycling was included in the plan to capture cycling effects on EBC degradation by comparison to the cyclic testing in this task. Exposure with applied mechanical loads was not included in this plan.

The samples used in this testing were of 1”x1” coupons machined from P&W Gen 1.2 CVI SiC/SiC panels. No sealcoating of the edges was completed after machining; however, coupons were coated with the P&W Gen 1.2 EBC system on both sides of the samples. The edges of the samples were also manually painted with the bondcoat slurry. Experience to date has shown that this approach avoids having the results of steam furnace cycle testing from being confounded by degradation of uncoated locations on the samples.

The intent of this testing was to provide data for the effect of steam on the rate and mechanisms of damage accumulation during thermal cycling, via comparison to the test results from the ambient furnace cycle testing described above. The saturated steam environment simulates the water concentration in the gas phase that is representative of combustion products in the hot section of a turbine engine. Again, post-test destructive microstructural analysis of samples removed from test after several durations was used to develop the output data for this testing. Due to the low velocity of the water vapor in this test, no significant recession of the EBC topcoat was anticipated during this testing. Testing to determine the recession kinetics of the topcoat are described in the section on steam jet testing.

Based on experience from ambient and steam FCT testing at higher temperatures than those planned for this task, P&W did not expect spallation of the EBC to occur within the time available for testing given the current program of record for this contract. Thus, fixed duration testing similar to that described in the ambient furnace cycle testing section was planned.

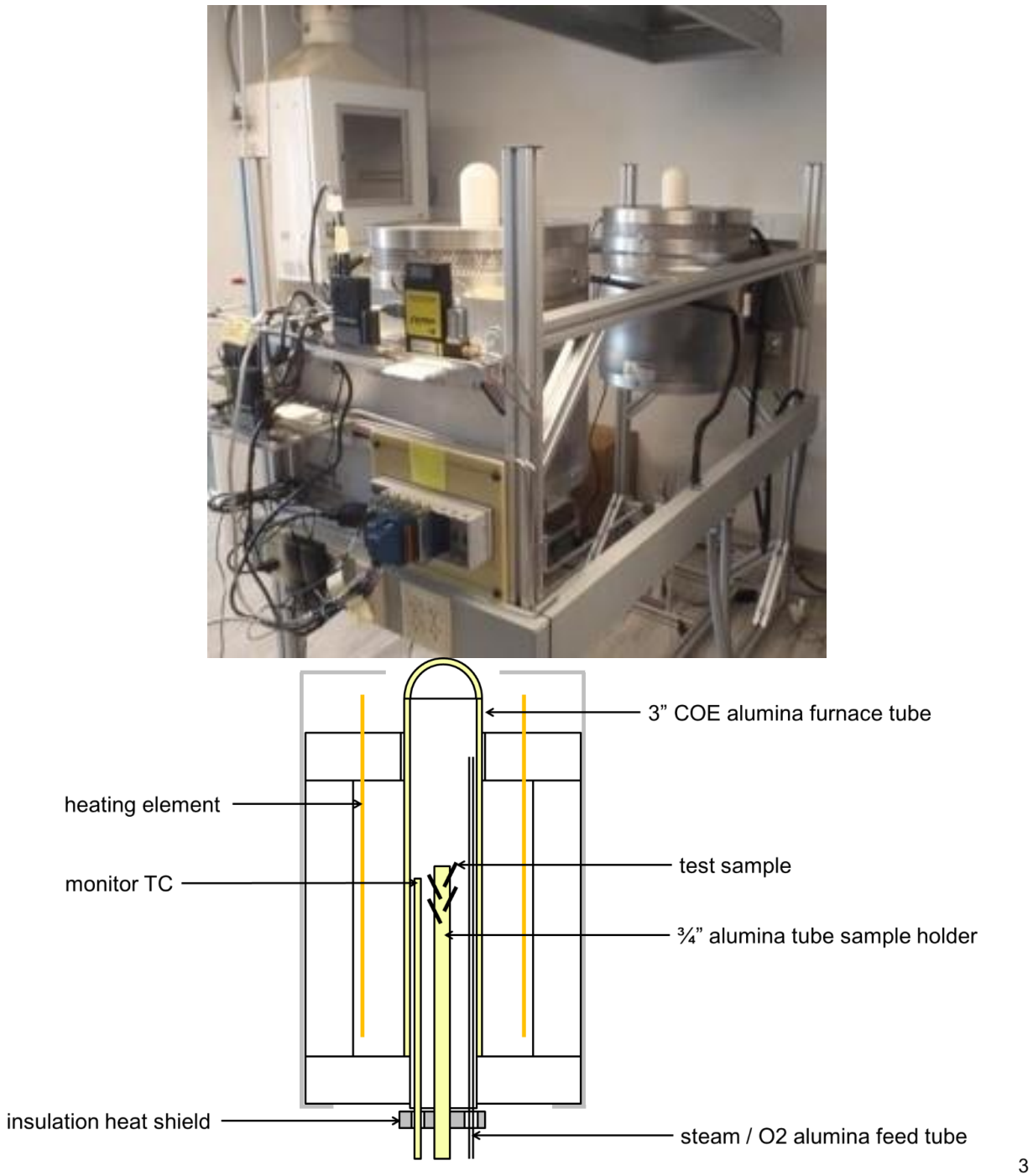

Figure 29. Photograph (top) and schematic (bottom) of the RTRC cyclic steam furnace

Table 8 summarizes the planned conditions for steam furnace cycle testing. Testing was planned at two temperatures - average climb temperature (T2) and T1+ 100°F. The choice of T1 + 100°F for the second test temperature was to expand the design space for which P&W has data. T1 + 100°F was a better choice than T1 to leverage historical data. Only two (2) samples were able to be tested at a time. Two (2) samples were planned to be put in the rig at the start of

the test. After 33% of the planned test time, one sample was planned to be removed and replaced by a second sample that would run for the remaining planned 66% of the test hours.

Table 8. Test plan for steam furnace cycle testing

Temperature	# of samples removed after 33% of total cycles	# of samples removed after 66% of total cycles	# of samples removed after 100% of total cycles
T1 +100°F	1	1	1
T2	1	1	1

Cyclic Gradient Burner Rig Testing

Cyclic gradient burner rig testing was completed using a gradient burner rig designed by RTRC and an outside vendor. A photograph of the rig is shown in Figure 30. The rig used methane/O2 torches to heat the front side and forced air cooling of the backside of the samples to achieve the gradient. Front and backside pyrometers continuously monitored temperature during the test. Samples were translated in and out of the flame to achieve the rapid cycling.

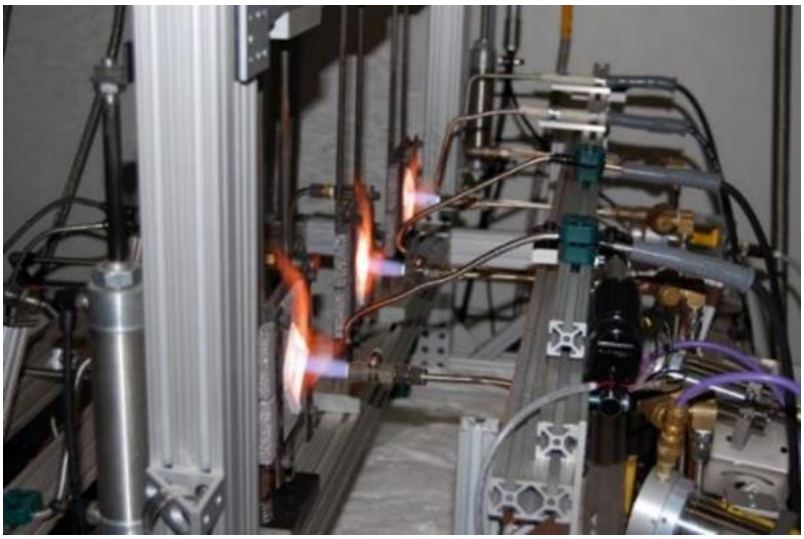

Figure 30. Photograph of the RTRC gradient burner rig

The intent of this testing was to compare to the testing described in the previous three sections primarily to elucidate the role of rapid cycling on the damage accumulation during exposure. The temperature gradients through the EBC and CMC were relatively small since the relevant part is uncooled. As a result, effects of through thickness gradients in this testing are expected to be small. Again, post-test destructive microstructural analysis of samples removed from test after several durations was relied upon to develop the output data for this testing.

The samples used in this testing were 1.5” diameter coupons machined from P&W Gen 1.2 CVI SiC/SiC panels. No CVI SiC sealcoating of the edges was completed after machining. Coupons were coated with the P&W Gen 1.2 EBC system on one side. The second side had to be uncoated in order to achieve the thermal gradient during the test.

The one rig that was available for this test is capable of testing four (4) samples simultaneously. The plan was to test one sample each for the full duration or to failure,

whichever comes first, with the topcoat/bondcoat interface temperature maintained at the temperature equivalent to max takeoff temperature. A second sample was planned to be tested for the full duration or to failure with the interface temperature maintained at T2 to simulate the climb condition. A third sample was tested for 25% of the planned full duration. Upon its removal, it was replaced by a fourth sample, which ran for the remaining planned 75% of the test cycles. A fifth and sixth sample were run for 50% of the planned test cycle, one after the other. Testing conditions that were completed are listed in Table 9. Note that the Final Test Plan CDRL document listed the full test duration planned that was longer than the duration that was executed in this task, due to constraints with access to the RTRC gradient burner rig.

Table 9. Test plan for gradient burner rig testing

Temperature	# of samples removed after 25% of total cycles	# of samples removed after 50% of total cycles	# of samples removed after 75% of total cycles	# of samples removed after 100% of total cycles
T1	1	2	1	1
T2	-	-	-	1

Steam Jet Testing

Steam jet testing was completed using a high velocity steam rig built at RTRC using a design that closely matches that reported by dos Santos e Lucato, et al, Ridley et al, and Golden, et al. A schematic of the rig is shown in Figure 31. The rig is contained in a tube furnace that tightly controls the temperature of the sample. A Pt-Rh capillary tube is located in the furnace, with the exit situated 1 mm from the surface of the sample. The surface of the sample was tilted at an angle of 30° degrees to the axis of the capillary exit. Water was pumped into and heated along the length of the capillary such that it transformed fully into steam before the capillary exit. The volume expansion associated with transformation to steam accelerated the steam, resulting in a high velocity steam jet impinging on the sample. Careful control of the water flow rate and heating to ensure full transformation to steam ensured control of the velocity of the water jet at the sample surface.

As the water jet expanded out of the capillary exit, the velocity continuously drops off such that there is a distribution of velocities on the surface of the sample. The maximum velocity occurs where the jet first reaches the sample surface. Informed by the procedure outlined in the Opila publications4,5, computational fluid dynamics (CFD) simulations were completed at RTRC to predict the velocity distribution of the steam on the sample surface as a function of distance from the capillary exit. CFD simulations were carried out for all steam jet parameters to be used in the test matrix, as discussed below.

The planned test matrix is listed in Table 10. Three temperatures were tested: T1, T2, and T3+90°F. The original plan in the final test plan CDRL for this task was for the third temperature to be T3. However, T3+90 was chosen to be consistent with testing published in the open literature. Two different water flowrates were tested to vary the velocity of the steam jet impinged on the sample in line with flowrates reported in the literature 4,5. Three test durations were tested.

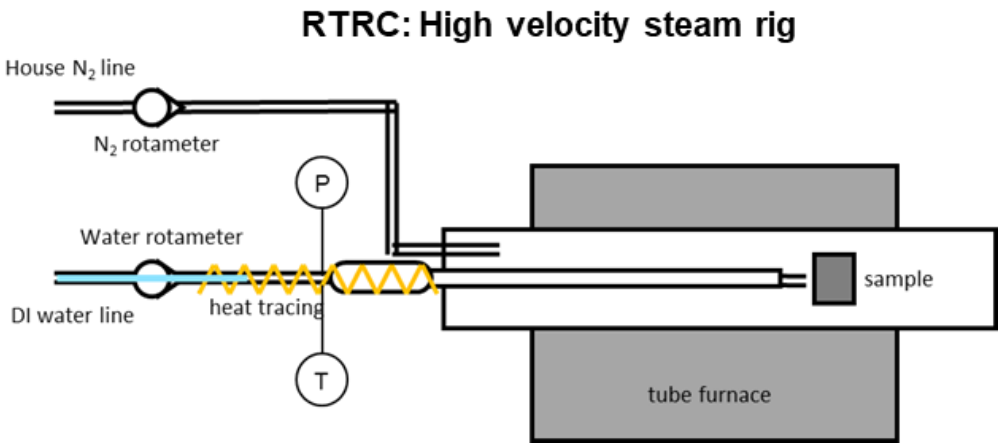

Figure 31. Schematic diagram of the RTRC high velocity steam rig

Post-test nondestructive and destructive analysis was carried out to assess the variation of water recession damage as a function of distance from the impingement location of the steam jet on the sample surface. Backscattered SEM analysis (BSE SEM) was used to image the surface of the tested specimens. The area of the sample surface that was recessed during the test appeared in brighter contrast since recession increases the average atomic number of the topcoat material, since it removes SiO2 from the HfSiO4, leaving behind HfO2. Image analysis of the SEM images was completed to quantify the affected area. Cross sections in a few locations were then completed and analyzed by SEM and image analysis to quantify the penetration depth of the recessed zone. These results were then used to calibrate a CFD prediction of the geometry of the affected zone. This calibrated CFD model was then used to predict the geometry of the affected zone for the other conditions that were tested. The results agreed well with the experimental results. This CFD model can now be used to predict the geometry of recession associated with high velocity water vapor interaction with the P&W topcoat, as a function of steam velocity, exposure time, and test temperature.

Table 10. Planned tests for high velocity steam testing

Temperature	Water flow rate	Time	# of samples
T1	Low	Medium	1
T1	High	Medium	1
T2	Low	Medium	1
T2	High	Medium	1
T3 + 90°F	Low	Medium	1
T3 + 90°F	High	Medium	1
T1	High	Short	1
T1	High	Long	1
T2	High	Short	1
T2	High	Long	1
T3 + 90°F	High	Short	1
T3 + 90°F	High	Long	1

3.2.3 Post-Test Analysis

Tested coatings were cross-sectioned, mounted in epoxy, polished, and imaged using a VLM (visible light microscope model + imaging mode) and a Phenom XL scanning electron microscope (SEM) equipped with a backscattered electron detector (BSE). Due to chemical similarity between the gettering phase and matrix, VLM was used to obtain high-quality images of the gettering phase for image analysis. Image analysis was used with thresholding to determine the area percentage of getter phase in the VLM images. However, infiltration by epoxy into interior pores of the coating obscured these features in VLM imaging. Epoxy does not emit much back-scatter signal when imaged in SEM, thus, SEM imaging was used to obtain images for quantifying the porosity in the EBC bondcoat.

Image analysis of the area percentage of the gettering phase and of the porosity in the bondcoat was performed using ImageJ software with custom-written macros to threshold and measure the features of interest. The number of pixels per micron was calibrated for each image using ImageJ to measure the micron bar that was added to each image by the VLM or SEM software. Images were cropped to remove topcoat and substrate before analysis. At least 3 images (>1000 features) were used to obtain the reported area percentages for each test exposure. For the test types for which area percentage of the gettering phase and the porosity is reported, it is compared to data measured from the same set of three (3) cross sections of as processed bondcoats.

Task 2.2.5 Steam furnace cycle testing in the NASA Steam FCT rig

Steam furnace cycle testing in a low velocity, ambient pressure, saturated steam environment was carried out using steam cyclic furnaces previously designed and built at the NASA Glenn Research Center. The flowing steam environment had a constant water/oxygen ratio established controlled using mass flow controllers. Temperature was controlled via a thermocouple located close to the samples.

The thermal cycle consisted of a maximum temperature soak that was five times faster than the cooling portion of the cycle. The ratio of maximum temperature soak time to cooling time was much higher for the RTRC rig.

The samples used in this testing were 1”x1” coupons machined from P&W Gen 1.2 CMC panels. No sealcoating of the edges was completed after machining, The samples coated with P&W EBCs for Task 2.2.5.1 were coated with the P&W Gen 1.2 EBC system on *both* sides of the samples. The edges of the samples were also manually painted with the bondcoat slurry. Experience to date has shown that this approach avoids having the results of steam furnace cycle testing from being confounded by degradation of uncoated locations on the samples. For Task 2.2.5, the samples that were coated with NASA EBCs were only coated on one side.

The intent of Task 2.2.5 testing was to provide data for the effect of the differences in the rig design of the NASA Steam FCT rig as compared to the RTRC Steam FCT rig and the difference in cycling frequency on the rate and mechanisms of damage accumulation during thermal cycling, via comparison to the test results from the steam furnace cycle testing completed in Task 2.2. Recall that the environment simulates the water concentration in the gas phase that is representative of combustion products in the hot section of a turbine engine. Again, the intent of Task 2.2.5 testing was to compare damage mechanisms and damage accumulation rates between the NASA EBC and the P&W EBC. Post-test destructive microstructural analyses of samples removed from test after several durations were used to develop the output data for these tasks. Due to the low velocity of the water vapor in this test, no significant recession of the EBC topcoat was anticipated during this testing.

Task 2.2.5 – Steam FCT testing of P&W EBCs on P&W CMCs in the NASA rig

Table 11 summarizes the planned conditions for steam furnace cycle testing in Task 2.2.5. The temperature choices were discussed previously in this report. The durations for testing at T1+100°F were chosen to match the accumulated hours at which P&W EBCs failed in Task 2.2 in the RTRC rig – t1, 2.7*t1, and 5*t1. The numbers of hours and cycles were the same in the NASA Steam FCT test rig. Testing to failure was also included in the plan. Three samples were tested for each duration. In Task 2.2, the cycling frequency was much lower, so samples underwent much fewer thermal cycles in the RTRC fig used in Task 2.2 as compared to the NASA Steam FCT test used in Task 2.2.5.

The durations for testing at T2 in Task 2.2.5 were chosen to match durations that had been completed under P&W internal funding to understand the failure mechanisms and damage accumulation rates after failure of the P&W EBCs occurred much earlier than expected in Task 2.2. As indicated in Table 11, exposures of t2, 1.75*t2, 3.75*t2 hours and cycles, and testing to failure were planned, with three (3) samples tested for each duration. Again, recall that testing completed under P&W internal funding in the RTRC rig in support of Task 2.2 was done with much lower cycling frequency.

Table 11. Test plan for steam furnace cycle testing in Task 2.2.5

Temperature	Number of Hours and Cycles – Group 1	Number of Hours and Cycles – Group 2	Number of Hours and Cycles – Group 3	Number of Hours and Cycles – Group 4
T1 + 100 F	t1	2.7*t1	5*t1	Failure
T2	t2	1.75*t2	3.75*t2	Failure

Task 2.2.5 – Steam FCT testing of NASA EBCs on P&W CMCs in the NASA rig

Table 12 summarizes the planned conditions for steam furnace cycle testing in Task 2.2.5.2. The temperature choices were discussed previously in this report. The same durations were chosen for testing at T1 + 100°F and T2 since similar durability was expected at both temperatures. Test durations of t3, 3*t3, 5*t3, and 10*t3 hours and cycles were chosen. Three (3) samples were tested for each group.

Table 12. Test plan for steam furnace cycle testing in Task 2.2.5.

Temperature	Number of Hours and Cycles – Group 1	Number of Hours and Cycles – Group 2	Number of Hours and Cycles – Group 3	Number of Hours and Cycles – Group 4
T1+100 F	t3	3*t3	5*t3	10*t3
T2	t3	3*t3	5*t3	10*t3

Post-Test Analysis for Added Scope Tasks

Macroscopic images were taken of the samples after each planned exposure. Tested coatings were cross-sectioned, mounted in epoxy, polished, and imaged using a VLM (visible light microscope model + imaging mode) and a Phenom XL scanning electron microscope (SEM) equipped with a backscattered electron detector (BSE). Due to chemical similarity between the

gettering phase and matrix, VLM was used to obtain high-quality images of the gettering phase in the P&W EBC. However, infiltration by epoxy into interior pores of the coating obscured these features in VLM imaging. Since epoxy does not emit much back-scatter signal when imaged in SEM, SEM imaging was used to investigate porosity in the EBC. No VLM was completed for NASA EBCs in Task 2.2.5.2 since SEM imaging effectively images all phases in the NASA EBC.

3.2.4 Results and Discussion

3.2.4.1 Static ambient furnace testing

T1 static ambient furnace testing

Table 13 lists the sample identification numbers, percentages of hours accumulated relative to the longest exposure, and percentage of area spalled for the eight (8) samples that were tested at T1 in static ambient furnace testing. The test went according to plan, with all samples accumulating the total number of hours planned. There was no spallation nor any evidence of macroscopic distress on any of the samples. Figure 32 shows photographs of the samples taken before and after the test, confirming this observation.

Table 13. Results for T1 static ambient furnace testing

Exposure	25%		50%		75%		100%	
	Sample ID	**% spalled**	**Sample ID**	**% spalled**	**Sample ID**	**% spalled**	**Sample ID**	**% spalled**
	NH4	0	NH72	0	NH2	0	NH86	0
	NH10	0	NH78	0	NH48	0	NH46	0

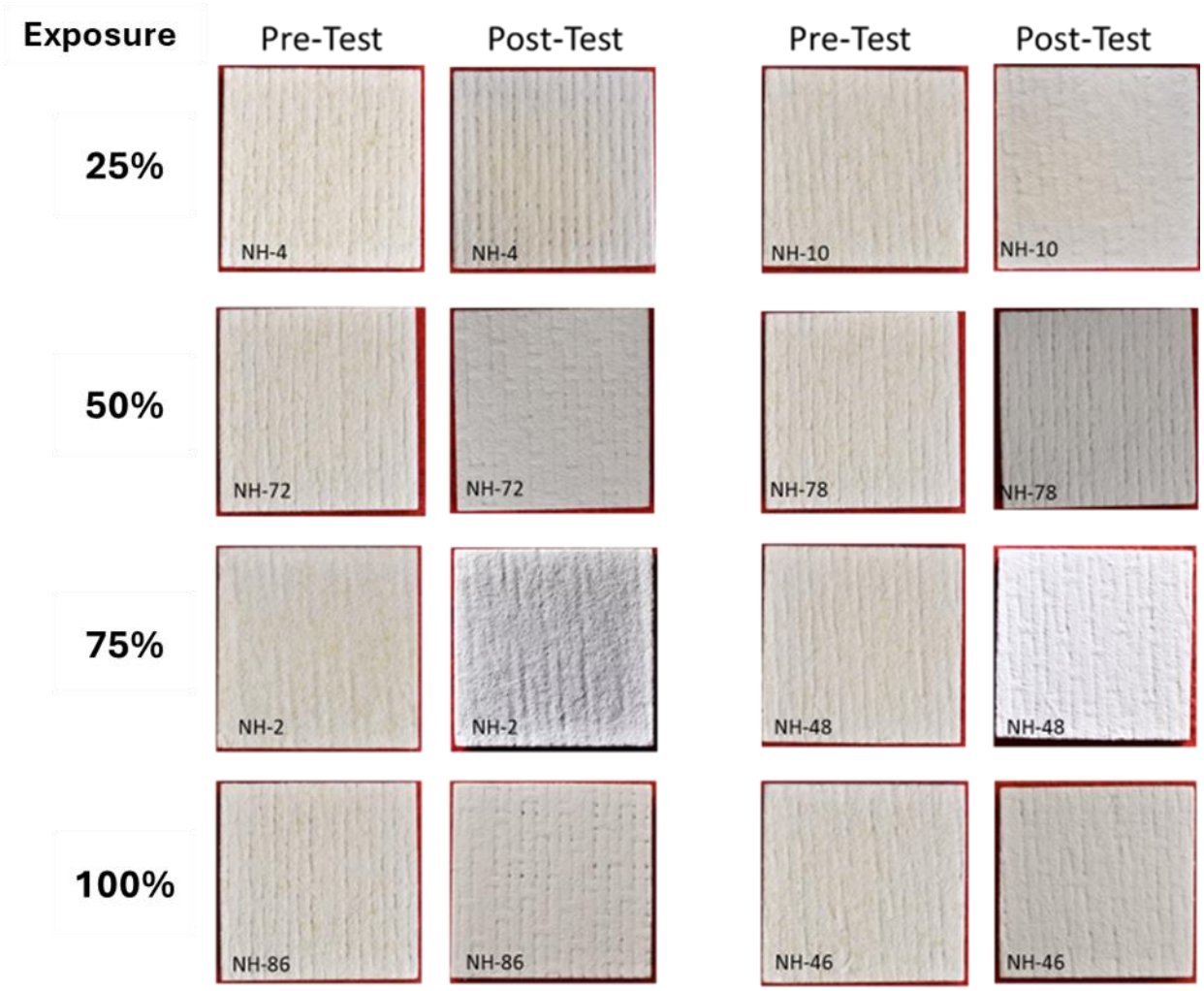

Figure 32. Photographs of samples before and after the T1 static ambient furnace test

Microstructural assessment was completed on all of the post-test samples, and inferences on mechanisms contributing to damage progression in the static ambient furnace test were documented. It was noted that after all exposures, the CMC was fully protected from oxidation

Figure 33 shows the average area percentage of gettering phase and porosity measured using image analysis of at least three (3) images from each exposure in the T1 FCT test, compared to data from an as-processed baseline. The gettering phase data showed a significant reduction in getter phase are percentage in the first 25% of the total planned exposure. Gettering phase area percentage continued to decrease during the next 25% of total planned exposure. There was no further significant reduction in the gettering phase area after the remaining two exposures The error bars for all the porosity measurements overlapped, indicating that there were no statistically significant differences in area percentage of porosity between the as processed bondcoat and any of the exposed bondcoat.

These results suggest that oxidation of the getter phase particles occurred within the first 50% of total planned exposure, but the oxidation rate of those particles slowed significantly for the remaining exposures. This suggests that the initial oxidation formed a protective scale around the gettering phase particles that protected them further oxidation very effectively. These results are similar to the results for T1 F ambient furnace cycle testing. Subtle differences between the two sets of results will be discussed later in this report.

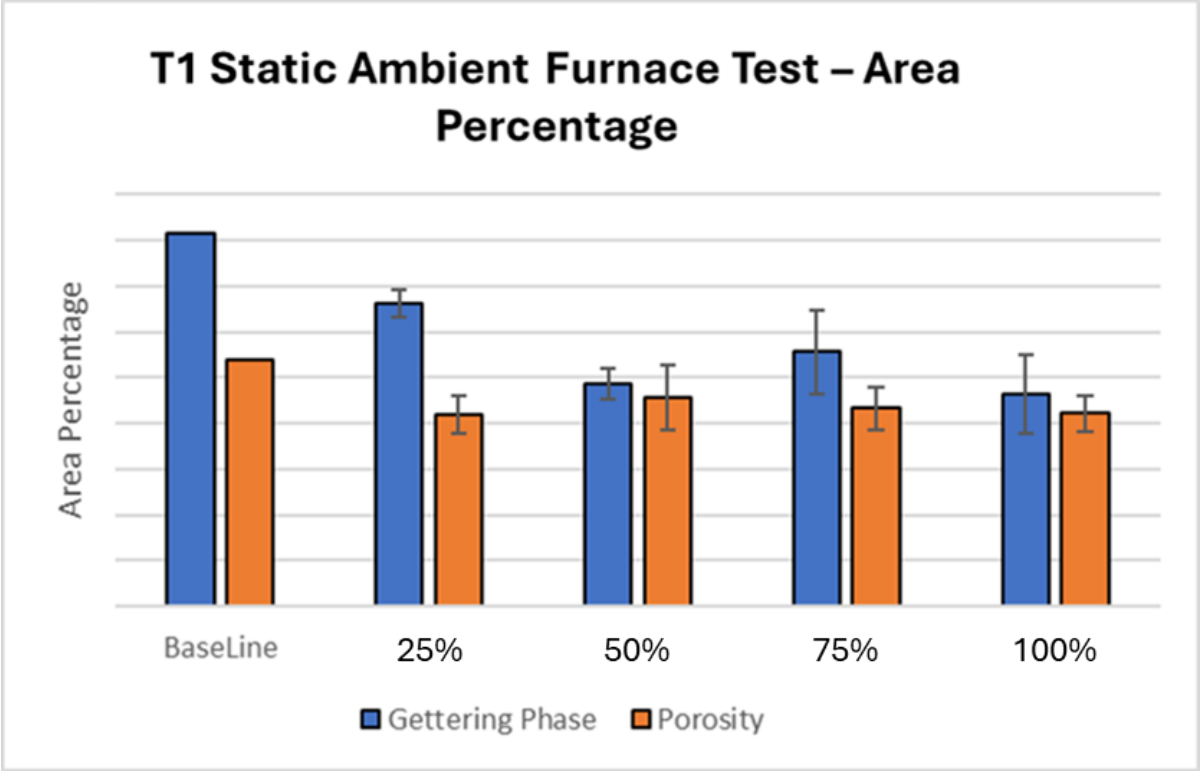

Figure 33. Average area percentages of gettering phase and porosity for each T1 static ambient furnace test duration compared to as-processed baseline measured by image analysis

T2 static ambient furnace testing

Table 14 lists the sample identification numbers, percentage of hours accumulated relative to the longest exposure, and percentage of area spalled for the eight (8) samples that were tested at T2 in static ambient furnace testing. Again, the test went according to plan, with all samples accumulating the total number of cycles planned. There was no spallation nor any evidence of macroscopic distress on any of the samples. Figure 34 shows photographs of samples taken before and after the testing, confirming that no spallation occurred.

Table 14. Results for T2 static ambient furnace testing

Exposure	25%		50%		75%		100%	
	Sample ID	**% spalled**	**Sample ID**	**% spalled**	**Sample ID**	**% spalled**	**Sample ID**	**% spalled**
	NH18	0	NH79	0	NH54	0	NH22	0
	NH67	0	NH82	0	NH70	0	NH80	0

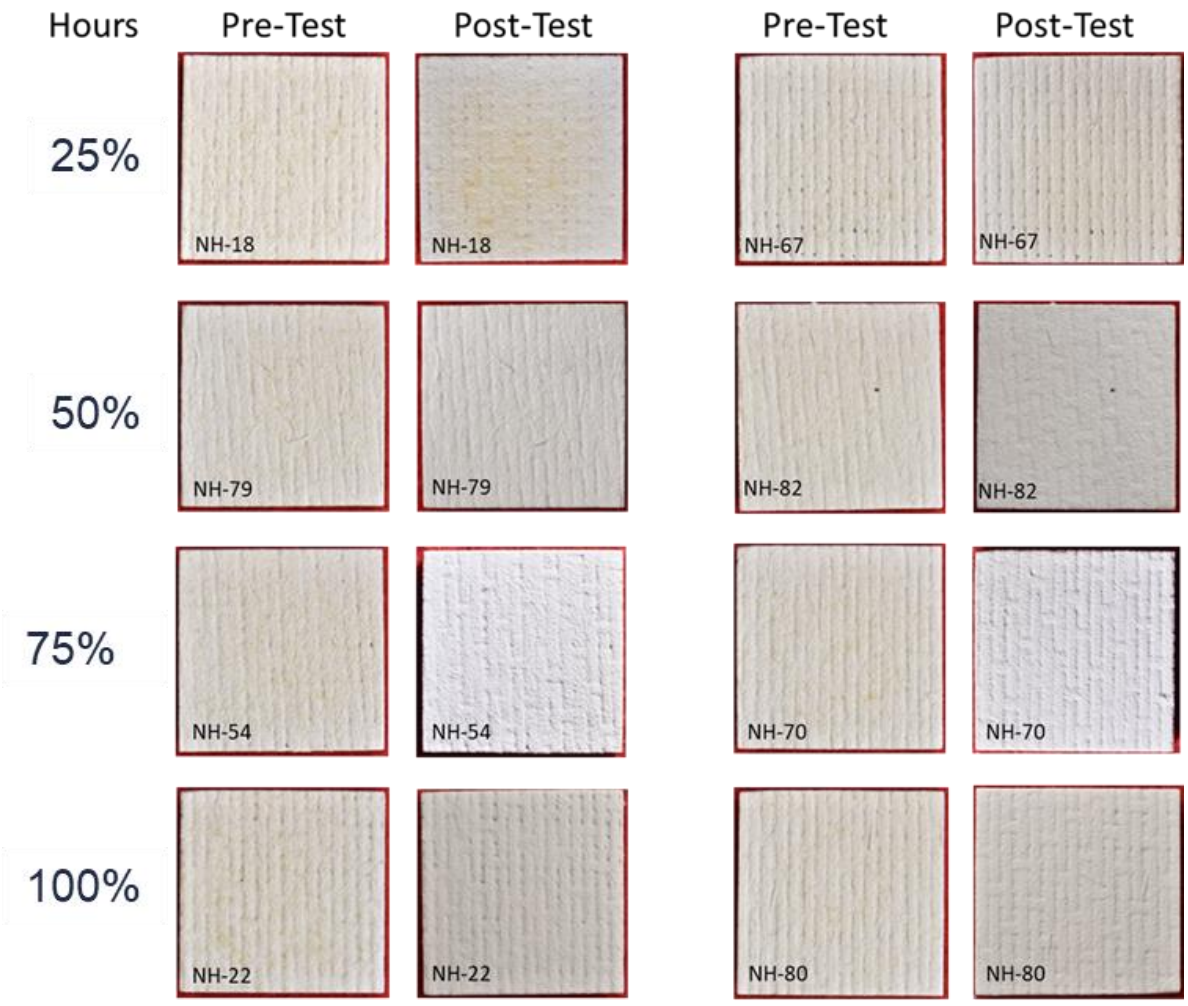

Figure 34. Photographs of samples before and after exposures in the static ambient air furnace test at T2

Microstructural assessment was completed on all of the post-test samples, and inferences on mechanisms contributing to damage progression in the static ambient furnace test were documented. No CMC oxidation was noted after any of the exposures.

Figure 35 shows the average area percentage of gettering phase and porosity measured using image analysis of at least 3 images from each exposure in the T2 static ambient furnace test, compared to data from an as-processed baseline. The average gettering phase area percentage data showed a steady reduction after 25%, 50%, and 75% of the planned exposure, though since the error bars overlapped, this trend was not statistically significant. There was no further reduction in the gettering phase area after the 100% exposures. The error bars for all the porosity measurements overlapped, indicating that there were no statistically significant differences in area percentage of porosity between the as processed bondcoat and any of the exposed bondcoat.

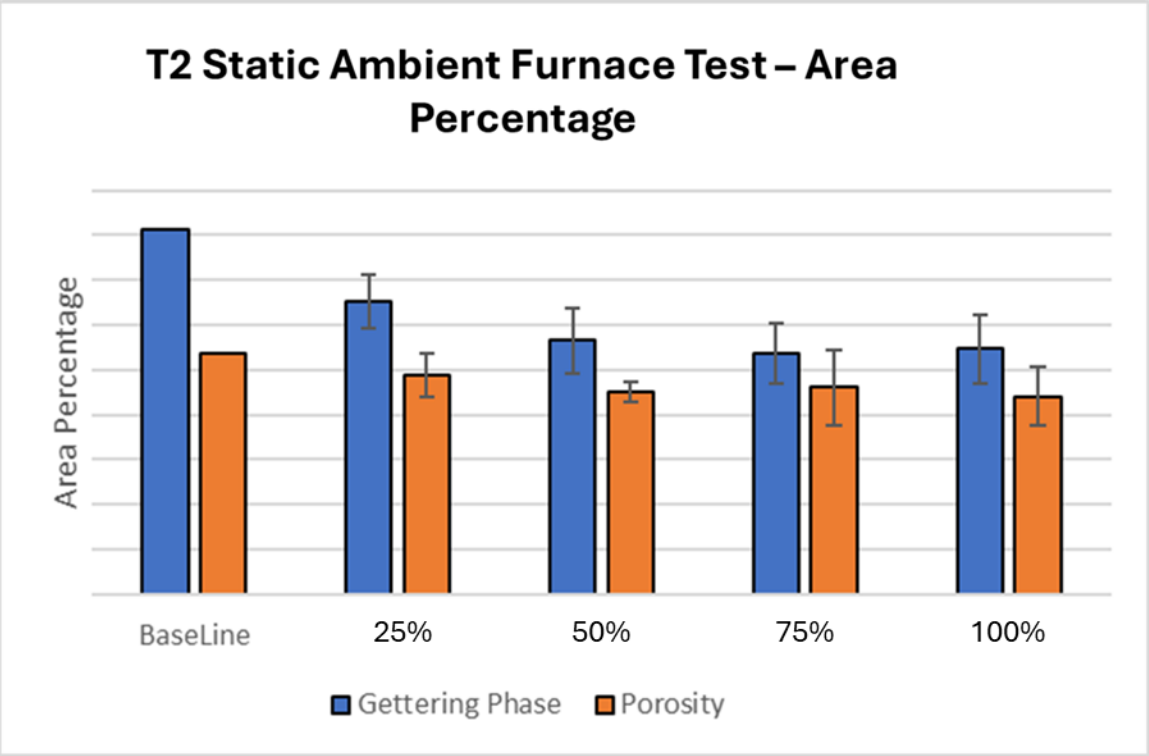

Figure 35. Average area percentages of gettering phase and porosity for each T2 static ambient furnace test duration compared to as-processed baseline measured by image analysis

These results suggest the getter phase oxidation rate was similar to the rate for the T1 static ambient furnace test for the first 25% of the exposure, but then slowed to a lower rate. Getter phase oxidation continued longer in this T2 test. This suggests that it took longer to form the protective scale around the gettering phase particles that protected them further oxidation. Comparisons to other tests will be discussed later in this report.

T3 static ambient furnace testing

Table 15 lists the sample identification numbers, percentage of hours accumulated relative to the longest exposure, and percentage of area spalled for the eight (8) samples that were tested at T3 in static ambient furnace testing. Again, the test went according to plan, with all samples accumulating the total number of cycles planned. There was no spallation nor any evidence of macroscopic distress on any of the samples. No photographs of the samples were taken before nor after the test due to an oversight. This testing was completed at a vendor. After the samples were returned for post-test metallography, it was assumed that post-test images had been taken by the vendor, so metallography was started without completing post-test imaging.

Table 15. Results for T3 static ambient furnace testing

Exposure	25%		50%		75%		100%	
	Sample ID	**% spalled**	**Sample ID**	**% spalled**	**Sample ID**	**% spalled**	**Sample ID**	**% spalled**
	NH33	0	NH32	0	NH51	0	NH12	0
	NH38	0	NH41	0	NH63	0	NH24	0

Microstructural assessment was completed on all the post-test samples, and inferences on mechanisms contributing to damage progression in the static ambient furnace test were documented. It was noted that after all the exposures, the CMC was fully protected from oxidation.

Figure 36 shows the average area percentage of gettering phase and porosity measured using image analysis of at least 3 images from each exposure in the T3 static ambient furnace test, compared to data from an as-processed baseline. The measured gettering phase area percentage data for all of the durations in this testing were more than 30% higher than all of the data discussed so far in this report. Since the samples were chosen at random for each test, the likelihood that the cause of this difference was just sample to sample variation due to bondcoat process variation was extremely unlikely.

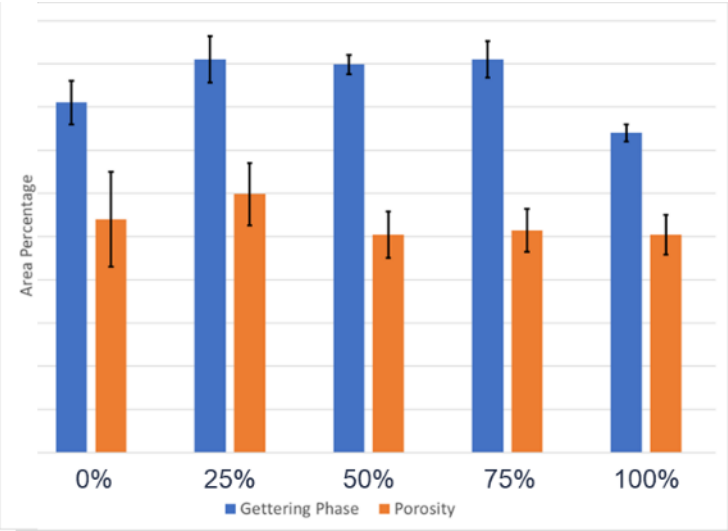

Figure 36. Average area percentages of gettering phase and porosity for each T3 static ambient furnace test duration compared to as-processed baseline measured by image analysis

After careful review of the images that were taken for image analysis, the higher area percentage of gettering phase reported for this test was attributed to the locations at which the images that were analyzed were taken. The microscopist who captured these images tended to focus on certain locations to capture images for image analysis, whereas previous images were captured away from these locations. To demonstrate this rigorously in this report is beyond the scope of the report. However, this attribution is made with high confidence, based on a rigorous review of the data.

We concluded that the T4, T5, and T3 static ambient furnace data should not be compared to the other datasets reported in this document, since images used to generate that data were all predominantly taken in a different location than the other datasets. However, since a similar sampling approach was used for all the images in that data, comparisons within that dataset may be valid.

Comparing the 25% through 75% planned exposure data in Figure 36 for the T3 static ambient furnace test indicates that very little depletion of the gettering phase occurred during these exposures. The area percentage of gettering phase did drop to significantly lower values after the 100% planned exposure. After reviewing the 100% planned exposure images it appears that they were predominantly taken away from the locations where the 25 to 75% planned exposure locations were taken. Thus, we were not able to deconvolute the effect of a different sampling

approach for the bondcoat microstructure from potential evidence that increasing the exposure to 100% planned exposure resulted in some depletion of the getter phase.

The error bars for all the porosity measurements overlapped, indicating that there were no statistically significant differences in area percentage of porosity between the as processed bondcoat and any of the exposed bondcoat.

T5 static ambient furnace testing

Table 16 lists the sample identification numbers, percentage of hours accumulated relative to the longest exposure, and percentage of area spalled for the eight (8) samples that were tested at T5 in static ambient furnace testing. Again, the test went according to plan, with all samples accumulating the total number of cycles planned. There was no spallation nor any evidence of macroscopic distress on any of the samples. No photographs of the samples were taken before nor after the test due to an oversight. This testing was completed at a vendor. After the samples were returned for post-test metallography, it was assumed that post-test images had been taken by the vendor, so metallography was started without completing post-test imaging.

Table 16. Results for T5 static ambient furnace testing

Exposure	25%		50%		75%		100%	
	Sample ID	**% spalled**	**Sample ID**	**% spalled**	**Sample ID**	**% spalled**	**Sample ID**	**% spalled**
	NH31	0	NH39	0	NH20	0	NH26	0
	NH53	0	NH73	0	NH57	0	NH59	0

Microstructural assessment was completed on all the post-test samples, and inferences on mechanisms contributing to damage progression in the static ambient furnace test were documented. It was noted that after all the exposures, the CMC was fully protected from oxidation.

Figure 37 shows the average area percentage of gettering phase and porosity measured using image analysis of at least 3 images from each exposure in the T5 static ambient furnace test, compared to data from an as-processed baseline. The measured gettering phase area percentage data for all the durations in this T5 testing were very similar to those reported in Figure 36 for the T3 testing data. The one exception was the 100% planned duration data, which exhibited less of a drop at the lower T5 test temperature.

After careful review of the images that were taken for image analysis, the higher area percentage of gettering phase reported for this test was attributed to the locations at which the images that were analyzed were taken. The microscopist who captured these images tended to focus on certain locations to capture images for image analysis, whereas previous images were captured away from these locations. To demonstrate this rigorously in this report is beyond the scope of the report. However, this attribution is made with high confidence, based on a meticulous review of the data.

We concluded that the T4, T5, and T3 static ambient furnace data should not be compared to the other datasets reported in this document, since images used to generate that data were all predominantly taken in a different location than the other datasets. However, since a similar sampling approach was used for all the images in that data, comparisons within that dataset may be valid.

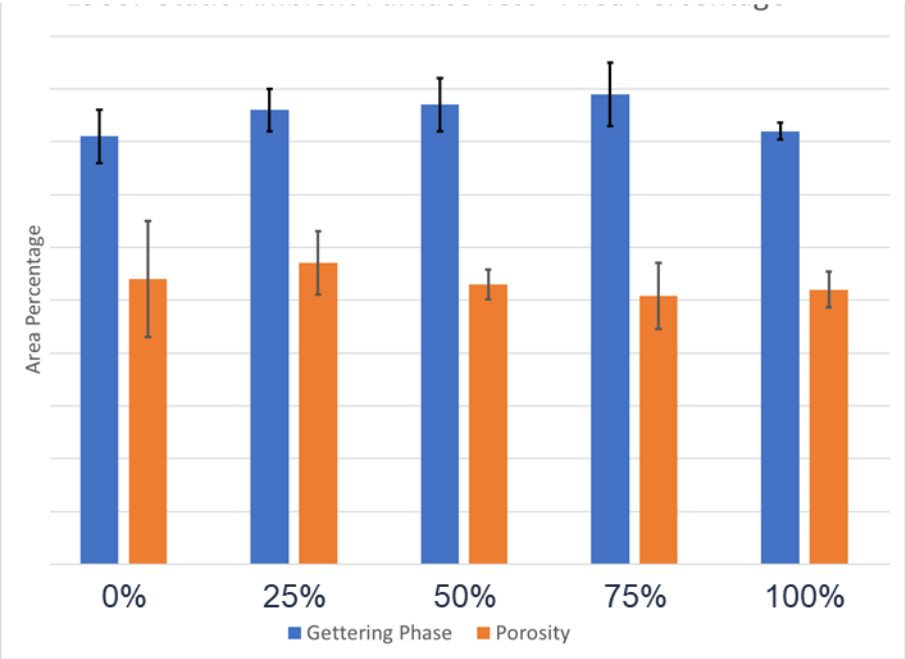

Figure 37. Average area percentages of gettering phase and porosity for each T5 static ambient furnace test duration compared to as-processed baseline measured by image analysis

Comparing the 25% through 75% planned duration data for area percentage gettering particles in the bondcoat for the T5 static ambient furnace test indicates that very little depletion of the gettering phase occurred during these exposures. The area percentage of gettering phase did drop to significantly lower values after the 100% planned exposure. After reviewing the 100% planned exposure images it appeared that they were predominantly taken away from the locations where the 25 to 75% planned exposure locations were taken. Thus, we were not able to deconvolute the effect of a different sampling approach for the bondcoat microstructure from potential evidence that increasing the exposure to 100% planned exposure resulted in some depletion of the getter phase.

The error bars for all the porosity measurements overlapped, indicating that there were no statistically significant differences in area percentage of porosity between the as processed bondcoat and any of the exposed bondcoat.

T4 static ambient furnace testing

Table 17 lists the sample identification numbers, percentage of hours accumulated relative to the longest exposure, and percentage of area spalled for the eight (8) samples that were tested at T4 in static ambient furnace testing. Again, the test went according to plan, with all samples accumulating the total number of cycles planned. There was no spallation nor any evidence of macroscopic distress on any of the samples. Figure 38 shows photographs of the samples before and after the test, providing evidence to support that statement.

Table 17. Results for T4 static ambient furnace testing

Exposure	25%		50%		75%		100%	
	Sample ID	% spalled	Sample ID	% spalled	Sample ID	% spalled	Sample ID	% spalled
	NH19	0	NH29	0	NH03	0	NH05	0
	NH69	0	NH75	0	NH23	0	NH76	0

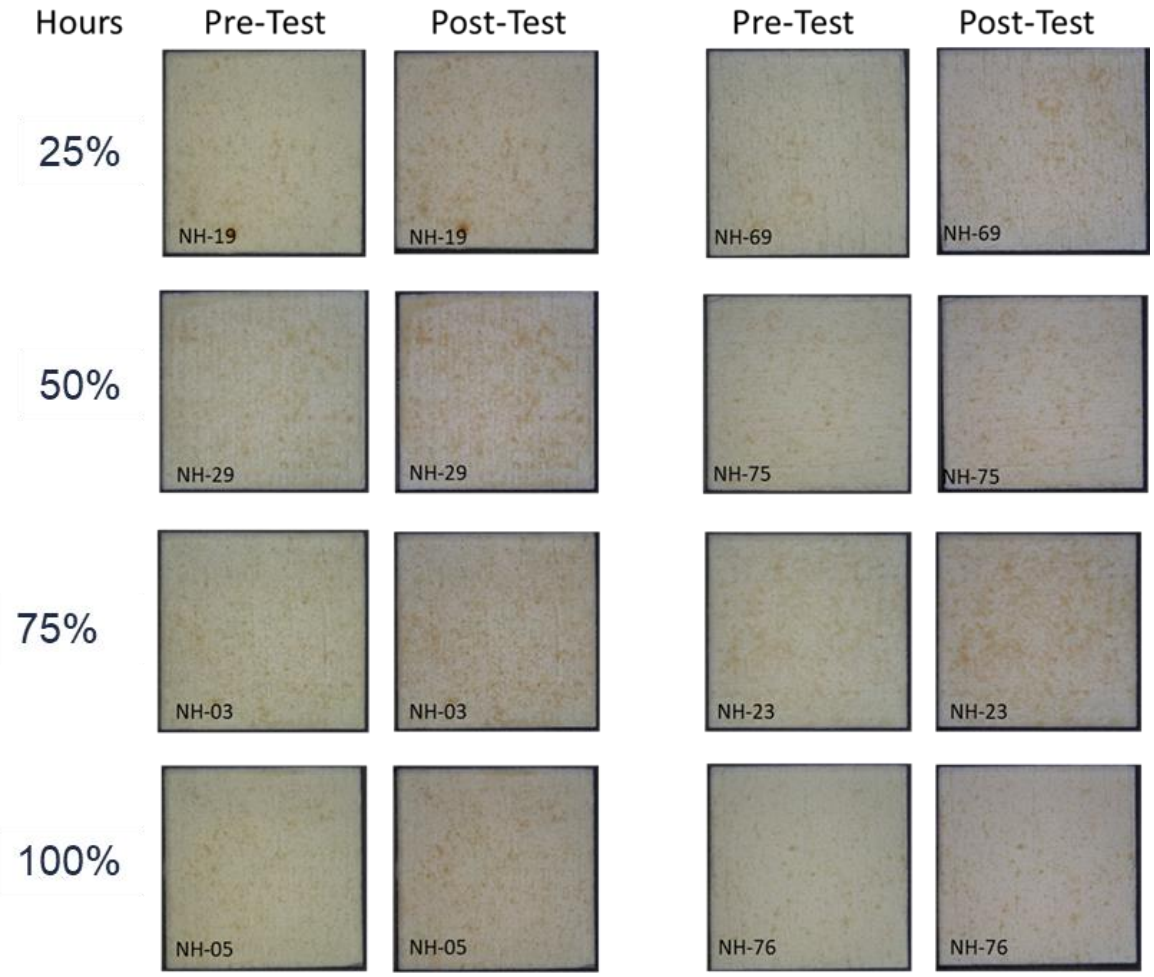

Figure 38. Photographs of samples before and after T5 static ambient furnace testing

Microstructural assessment was completed on all the post-test samples, and inferences on mechanisms contributing to damage progression in the static ambient furnace test were documented. No CMC oxidation was noted after any of the exposures

Figure 39 shows the average area percentage of gettering phase and porosity measured using image analysis of at least three (3) images from each exposure in the T4 static ambient furnace test, compared to data from an as-processed baseline. The measured gettering phase area percentage data for all the durations in this T4 testing were very similar to those reported in Figure 36 for the T3 testing data and in Figure 37 for the T5 testing data. The one exception was the 100% planned duration data, which exhibited less of a drop at the lower T4 test temperature.

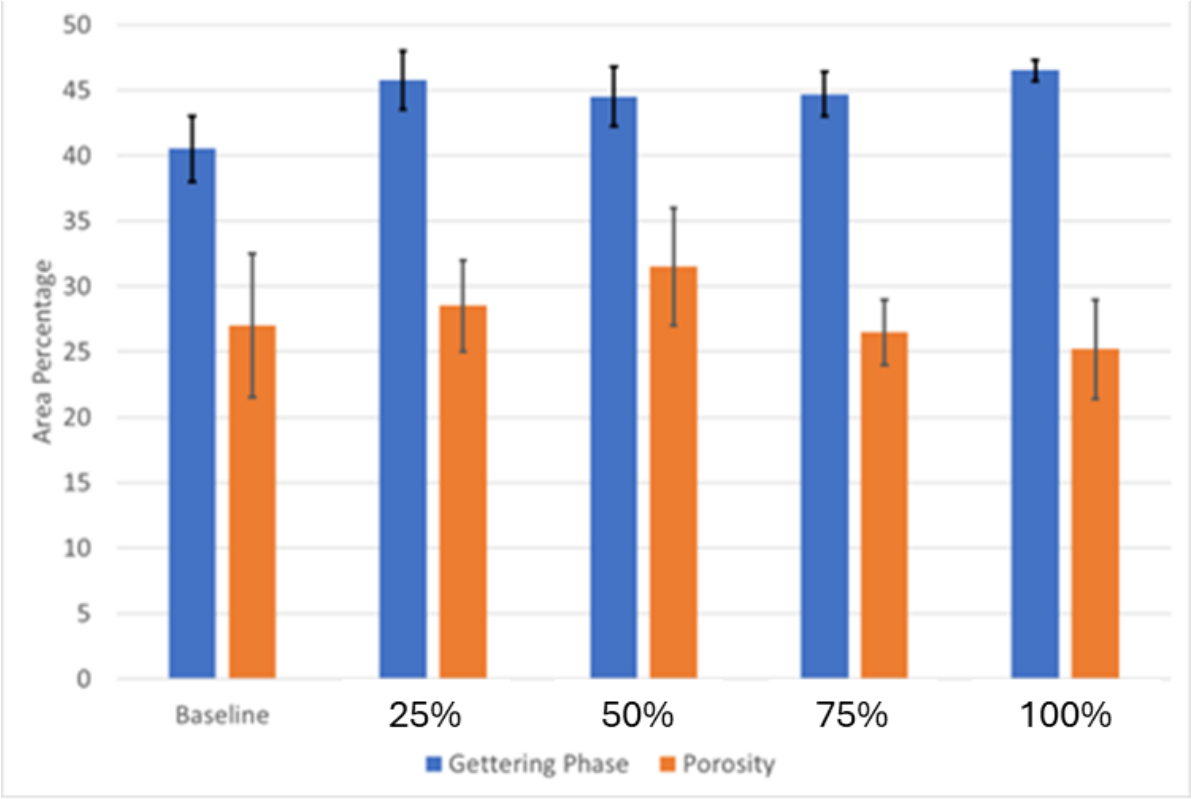

Figure 39. Average area percentages of gettering phase and porosity for each T4 static ambient furnace test duration compared to as-processed baseline measured by image analysis

Comparing the 25% through 75% planned duration data for area percentage gettering particles in the bondcoat for the T4 static ambient furnace test indicates that very little depletion of the gettering phase occurred during these exposures. The area percentage of gettering phase did drop to significantly lower values after the 100% planned exposure. After reviewing the 100% planned exposure images it appeared that that they were predominantly taken away from the locations were the 25 to 75% planned exposure locations were taken. Thus, we were not able to deconvolute the effect of a different sampling approach for the bondcoat microstructure from potential evidence that increasing the exposure to 100% planned exposure resulted in some depletion of the getter phase.

The error bars for all the porosity measurements overlapped, indicating that there were no statistically significant differences in area percentage of porosity between the as processed bondcoat and any of the exposed bondcoat.

3.2.4.2 Ambient furnace cycle testing

T1 ambient furnace cycle testing

Table 18 lists the sample identification numbers, percentage of cycles accumulated relative to the longest exposure, and percentage of area spalled for the eight (8) samples that were tested at T1 in ambient furnace cycle testing (FCT). The test went according to plan, with all samples

accumulating the total number of cycles planned. There was no spallation nor any evidence of macroscopic distress on any of the samples, although some slight discoloration did occur during the test on some samples. Figure 40 shows photographs of the samples taken before and after the test, confirming this observation.

Table 18. Results for T1 ambient furnace cycle testing

Exposure	25%	50%	75%	100%
	Sample ID	**Sample ID**	**Sample ID**	**Sample ID**
	NH35	NH11	NH17	NH15
	NH77	NH27	NH21	NH30

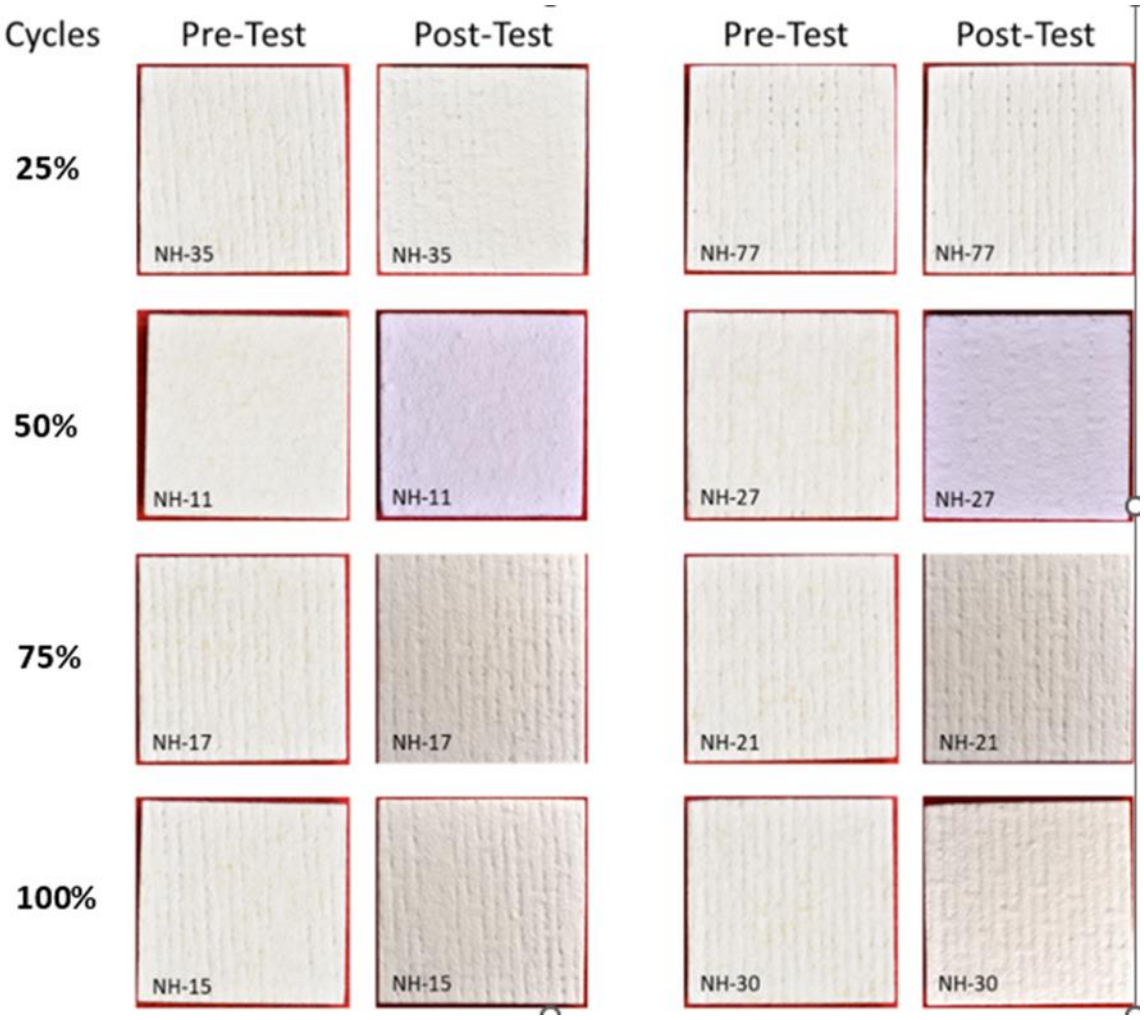

Figure 40. Photographs of samples before and after the T1 ambient furnace cycle test

Microstructural assessment was completed on all the post-test samples, and inferences on mechanisms contributing to damage progression in the ambient furnace cycle test were documented. It was noted that even after testing for 100% of the planned cycles, the CMC was fully protected from oxidation.

Figure 41 shows the average area percentage of gettering phase and porosity measured using image analysis of at least 3 images from each exposure in the T1 FCT test, compared to data from an as-processed baseline. The gettering phase data showed a significant reduction in gettering phase area percentage for the as-processed bondcoat as compared to the 25% exposure However, there was no further reduction in the gettering phase area reduction after the remaining three exposures The error bars for all of the porosity measurements overlapped, indicating that there were no statistically significant differences in area percentage of porosity between the as-processed bondcoat and any of the exposed bondcoat.

These results suggest that significant oxidation of the getter phase particles occurred within the first 25% of exposure, but the oxidation rate of those particles dropped to near zero for the remaining exposures. This suggests that the initial oxidation forms a protective scale around the gettering phase particles that protects them further oxidation very effectively.

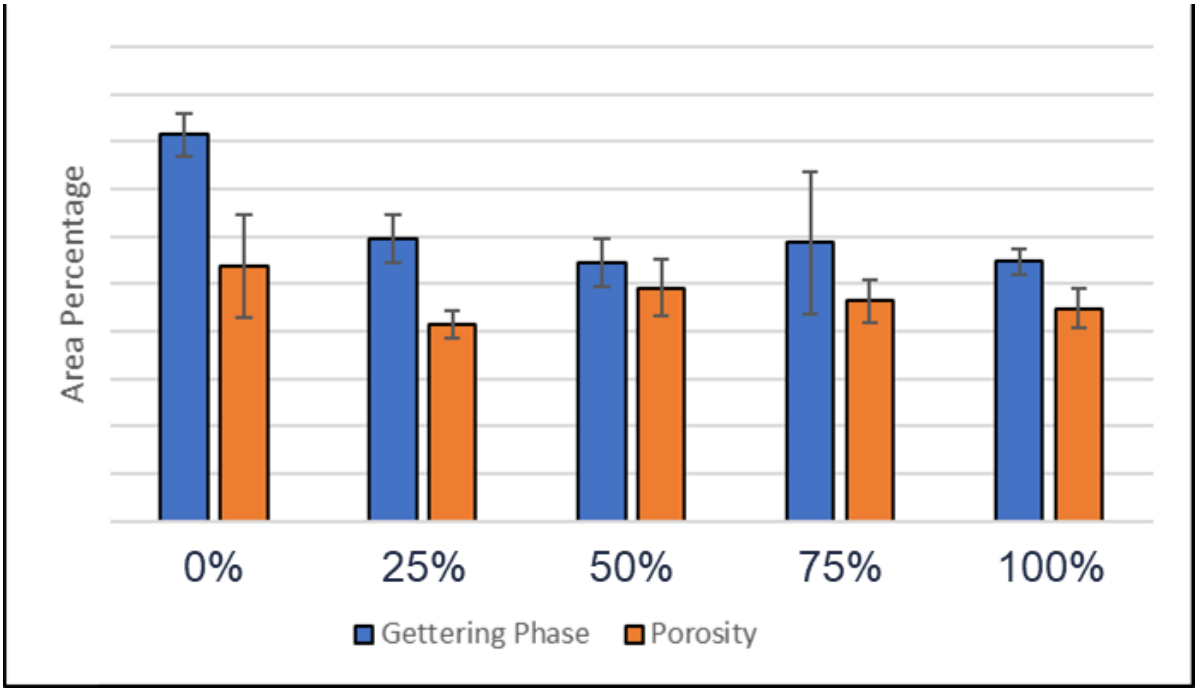

Figure 41. Average area percentages of gettering phase and porosity for each T1 FCT test duration compared to as-processed baseline measured by image analysis

T2 F ambient furnace cycle testing

Table 19 lists the sample identification numbers, and percentage of cycles accumulated relative to the longest exposure for the eight (8) samples that were tested at T2 in ambient furnace cycle testing (FCT). Again, the test went according to plan, with all samples accumulating the total number of cycles planned. Due to an oversight, no photographs of the samples were taken before and after the test. This testing was completed in-house in MPE. After the samples were returned for post-test metallography, it was assumed that post-test images had been taken, so metallography was started without completing post-test imaging.

Table 19. Results for T2 ambient furnace cycle testing

Exposure	25%	50%	75%	100%
	Sample ID	**Sample ID**	**Sample ID**	**Sample ID**
	NH16	NH11	NH47	NH1
	NH43	NH27	NH55	NH8

Microstructural assessment was completed on all the post-test samples, and inferences on mechanisms contributing to damage progression in the ambient furnace cycle test were documented. It was noted that even after testing for 100% of the planned cycles, the CMC was fully protected from oxidation.

Figure 42 shows the average area percentage of gettering phase and porosity measured using image analysis of at least 3 images from each exposure in the T2 FCT test, compared to data from an as-processed baseline. The gettering phase data showed a significant reduction in gettering phase area percentage during the first 25% of the planned test cycles. The mean area percentages continued to decrease steadily through the full test duration. However, the error bars overlapped for all the exposed getter phase area percentage data, so that trend was not statistically significant. The mean porosity area percentage of the exposed samples were all lower than the mean of the as-processed samples. However, the error bars for all the porosity measurements overlapped, so none of these differences were statistically significant.

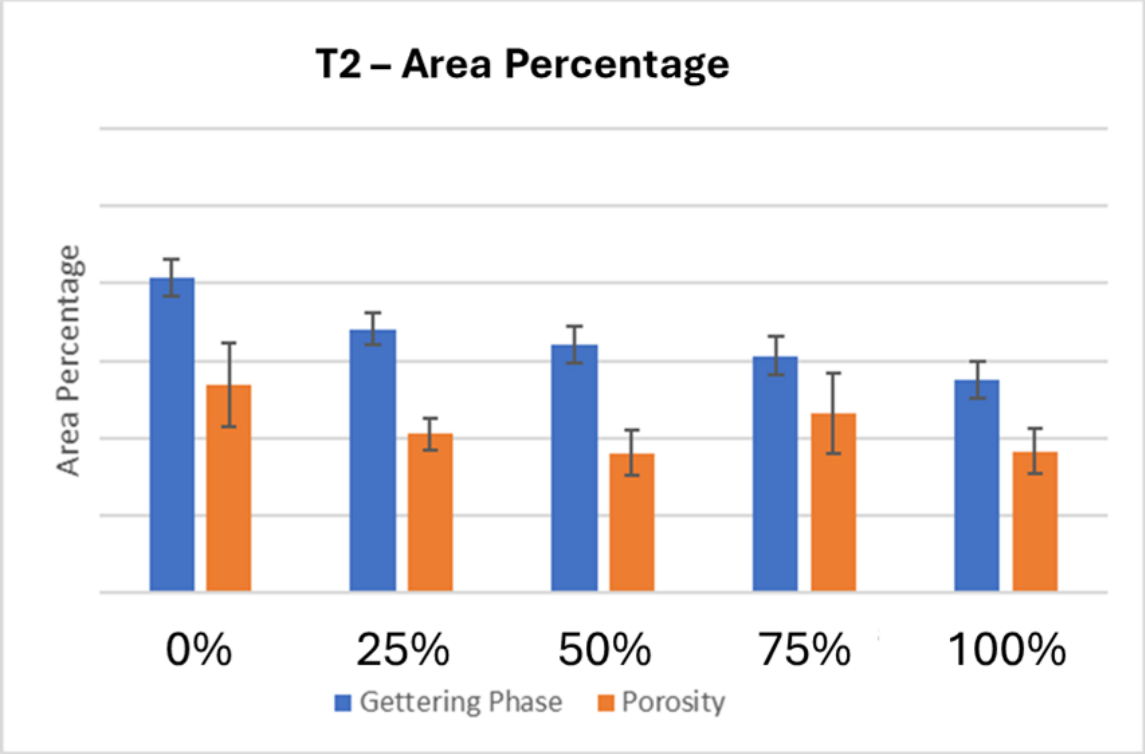

Figure 42. Average area percentages of gettering phase and porosity for each T2 FCT test duration compared to as-processed baseline measured by image analysis

Similar to the results for the T1 FCT test, there was a significant reduction of the getter phase area percentage relative to the as-processed baseline after the first 25% of planned cycles of exposure. Presumably due to slower kinetics at the lower test temperature, the mean area percentage of getter phase after 25% at T2 was higher than the mean after 25% at T1. This suggests that the protective scale formed around the getter particles during this first exposure was thinner for the T2 test as compared to the T1 test. Perhaps the initial thinner scale formed at T2 was less protective, explaining the weak downward trend in the mean area percentage of getter phase in the T2 data. The mean area percentages after 100% of planned exposure at both temperatures were very similar, so despite slower initial oxidation at T2, a higher oxidation rate during further exposure resulted in similar total getter phase loss after the full duration of testing.

Comparing the porosity area percentage data in Figure 42 for the T2 test to the data in Figure 41 for the T1 test, the mean area percentage of porosity was lower after 50% and 100% of planned cycles at T2 as compared to T1 Whereas it was difficult to discern any trends in the T2 data, the T1 data suggest a significant reduction of porosity after the 25% exposure at T2, then little change after further exposure. But the error bars overlap for all data in the T2 test, as they did for the T1 test, so these trends are not statistically significant. The large variability in area percentage of porosity from cross section to cross section confounds interpretation of trends in porosity as a function of exposure in ambient furnace cycle testing.

T3 ambient furnace cycle testing

Table 20 lists the sample identification numbers, number of cycles accumulated relative to the longest exposure, and percentage of area spalled for the eight (8) samples that were tested at T3 in ambient furnace cycle testing (FCT). Again, the test went according to plan, with all samples accumulating the total number of cycles planned. There was no spallation nor any evidence of macroscopic distress on any of the samples, although some slight discoloration did occur during the test on some samples. Figure 43 shows photographs of the samples taken after the test, confirming this observation. No photographs were taken of the samples before the test, due to an oversight.

Table 20. Results for T3 ambient furnace cycle testing

Exposure	25%	50%	75%	100%
	Sample ID	**Sample ID**	**Sample ID**	**Sample ID**
	NH49	NH14	NH36	NH56
	NH83	NH45	NH40	NH60

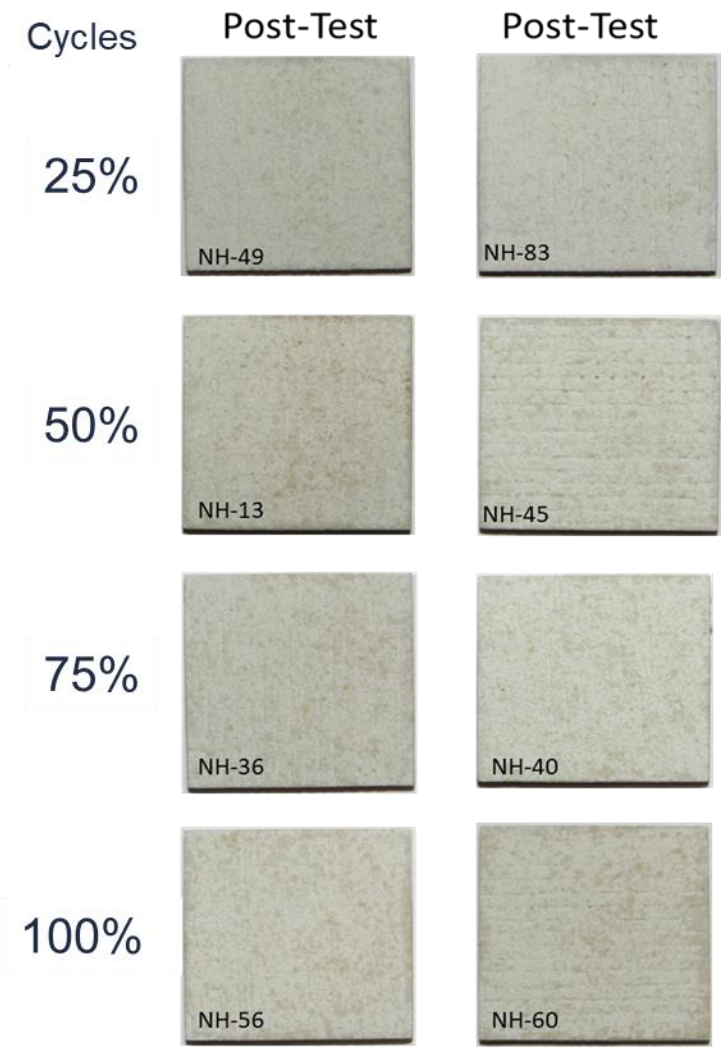

Figure 43. Photographs of samples taken after the T3 ambient furnace cycle test

Microstructural assessment was completed on all the post-test samples, and inferences on mechanisms contributing to damage progression in the ambient furnace cycle test were documented. It was noted that even after testing for 100% of the planned cycles, the CMC was fully protected from oxidation.

Figure 44 shows the average area percentage of gettering phase and porosity measured using image analysis of at least three (3) images from each exposure in the T3 FCT test, compared to data from an as-processed baseline. Contrary to the results for the T2 and T1 tests, there was no change in the mean area percentage of getter phase particles after the 25% and 50% exposures at T3. Slight reductions occurred after 75% and 100% of the planned cycles, such that after 100%, the mean area percentage of getter particles in the T3 test was similar to the values after 25% of the test durations, respectively, at T1 and T2. This suggests a significant reduction in the oxidation kinetics at T3 as compared to T1 and T2.

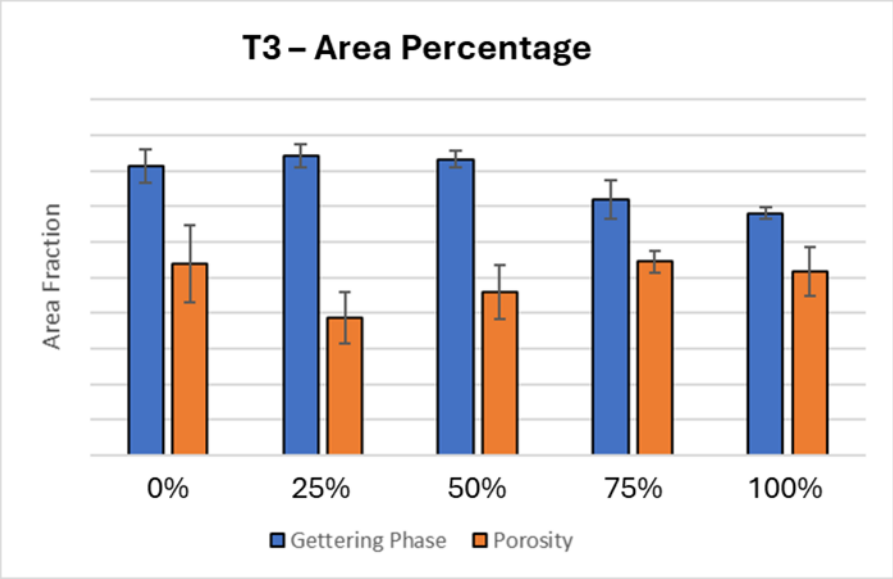

Figure 44. Average area percentages of gettering phase and porosity for each T3 FCT test duration compared to as-processed baseline measured by image analysis

The porosity area percentage data at T3 was similar to the T2 and T1 data. Again, the variability in the porosity area percentage from cross section to cross section makes it difficult to discern any changes in porosity during cyclic furnace exposure in ambient air, even when comparing T3 exposures to T1 exposures.

3.2.4.3 Static steam furnace testing

T1 static steam furnace testing

Table 21 lists the sample identification numbers, percentage of hours accumulated relative to the longest duration, and percentage of area spalled for the three (3) samples that were tested at T1 in static steam furnace testing. Again, the test went according to plan, with all samples accumulating the total number of cycles planned. There was no spallation nor any evidence of macroscopic distress on any of the samples. Figure 45 shows photographs of the samples before and after the test, providing evidence to support that statement. Both sides of the samples were coated for this test, thus the photograph shows both sides of the samples before and after the tests.

Table 21. Results for T1 static steam furnace testing

Exposure	33%		66%		100%	
	Sample ID	**% spalled**	**Sample ID**	**% spalled**	**Sample ID**	**% spalled**
	NH112	0	NH29	0	NH03	0

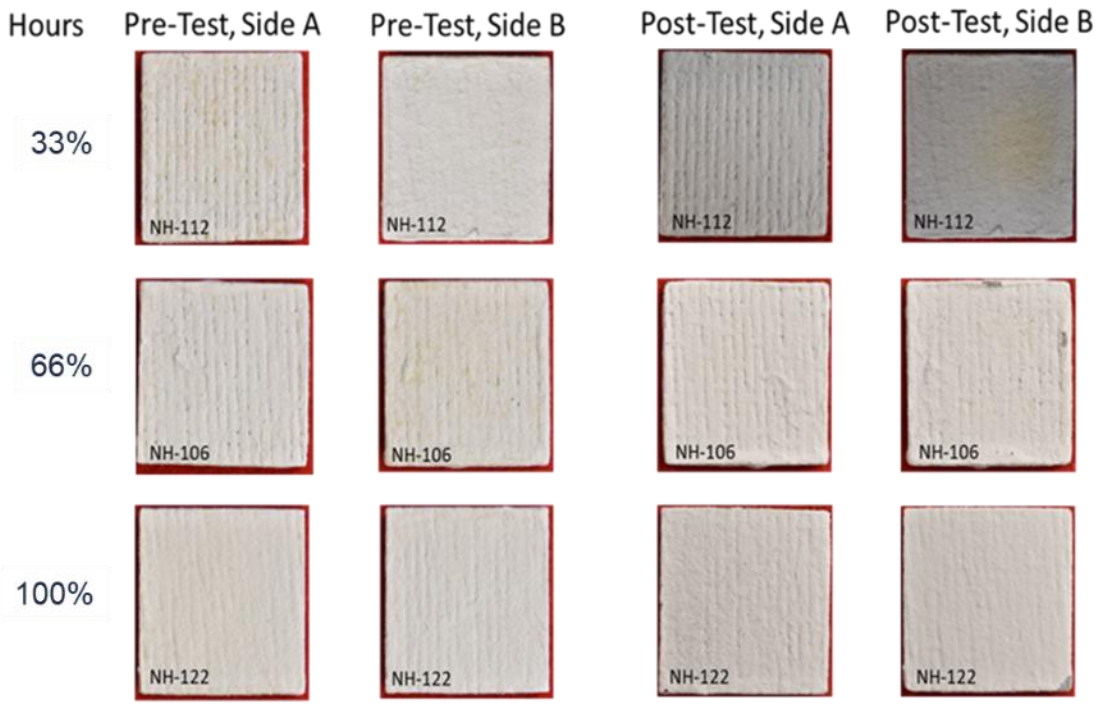

Figure 45. Photographs of both sides of the samples before and after T1 static steam furnace testing

Microstructural assessment was completed on all the post-test samples, and inferences on mechanisms contributing to damage progression in the static ambient furnace test were documented. No CMC oxidation was noted after any of the exposures

Figure 46 shows the average area percentage of gettering phase and porosity measured using image analysis of at least 3 images from each exposure in the T1 static steam furnace test, compared to data from an as-processed baseline. The data show continuous depletion of the SiC particles after all exposures. This underscores the acceleration of oxidation in the presence of saturated steam. The porosity data does not show a clear trend. Porosity variation is thus attributed to variation in porosity from sample to sample.

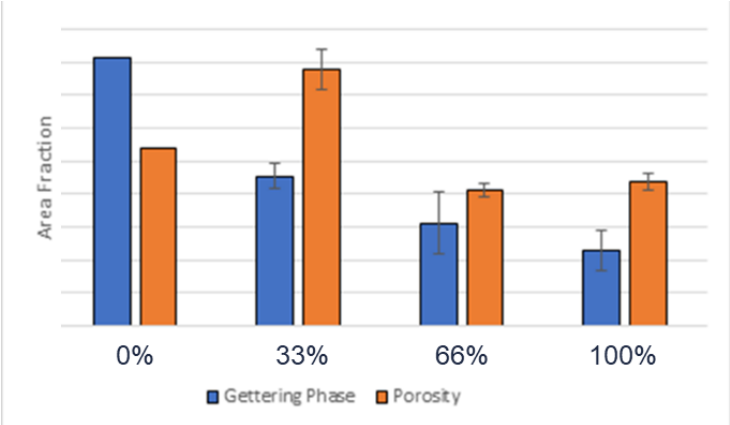

Figure 46. Average area percentages of gettering phase and porosity for each T1 static steam furnace test duration compared to as-processed baseline measured by image analysis

3.2.4.4 Steam furnace cycle testing

T1 +100F steam furnace cycle testing

Table 22 lists the target and actual percentages of life relative to the longest planned exposure, sample identification numbers, and percentage of area spalled for the three (3) samples that were tested at T1 + 100°F in ambient pressure saturated steam furnace cycle testing (FCT). Based on previous P&W experience with steam FCT testing at higher temperatures, there was an expectation that none of the samples would fail during any of the three exposures. However, on average the samples only survived 31.6% of total planned cycles with a very large standard deviation of 22.4%. As shown in the photographs in Figure 47 and listed in Table 22, at failure 100% of the topcoat spalled from the bondcoat.

Table 22. Results for T1 + 100 F steam furnace cycle testing

Target Life	33%		66%		100%	
Actual Life	30%		11%		56%	
	Sample ID	**% spalled**	**Sample ID**	**% spalled**	**Sample ID**	**% spalled**
	NH104	100	NH126	100	NH124	100

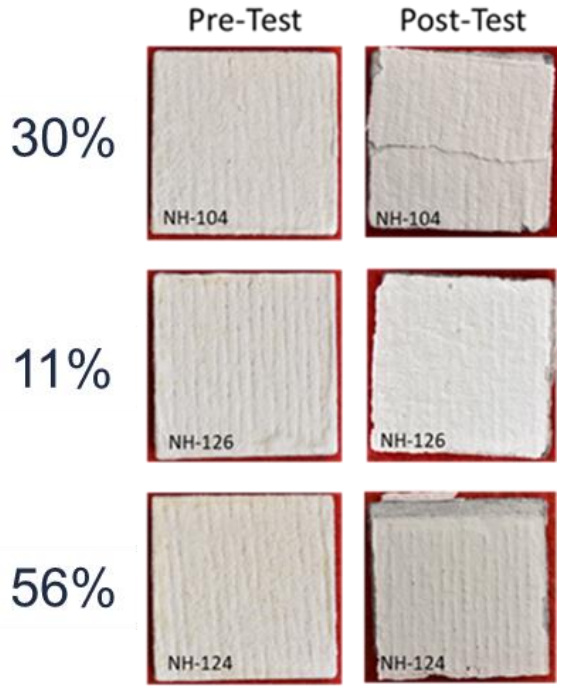

Figure 47. Photographs of samples before and after the T1 + 100 F steam furnace cycle test

Microstructural assessment was completed on all the post-test samples, and inferences on mechanisms contributing to damage progression in the steam furnace cycle test were documented. No CMC oxidation was noted after any of the exposures

T2 steam furnace cycle testing

Table 23 lists the target and actual percentages of life relative to the planned longest duration, sample identification numbers, and percentage of area spalled for the two (2) samples that were tested at T2 in ambient pressure, saturated steam furnace cycle testing (FCT). Both samples failed after 16.7% of the planned test duration. As shown in the photographs in Figure 48 and listed in Table 23, at failure only about 5% of the sample topcoat area was spalled, at corners and edges. However, the technician who was running the test noted that the EBC was only loosely adhered, so the samples was considered to have met the spallation criterion. When mounted in epoxy, the remaining topcoat spalled fully.

Table 23. Results for T2 steam furnace cycle testing

Target Life	33%		66%		100%	
Actual Life	16.7%		Did not run		16.7%	
	Sample ID	**% spalled**	**Sample ID**	**% spalled**	**Sample ID**	**% spalled**
	NH95	5	NH88	-	NH113	5

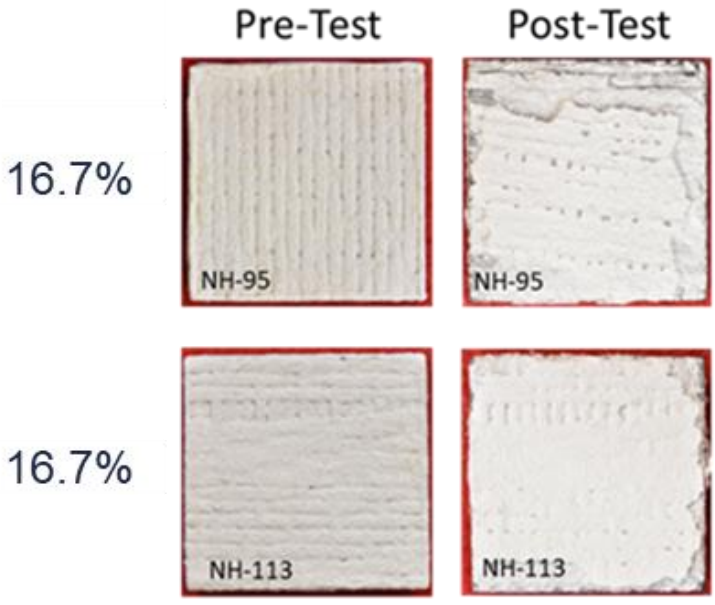

Figure 48. Photographs of samples before and after the T2 steam furnace cycle test

Microstructural assessment was completed on all of the post-test samples, and inferences on mechanisms contributing to damage progression in the steam furnace cycle test were documented. No CMC oxidation was noted after any of the exposures

3.2.4.5 Gradient burner rig testing

Gradient burner rig testing with a topcoat bondcoat interface temperature of T1

Table 24 lists the target and actual percentages of life relative to the planned longest duration, sample identification numbers, and percentage of area spalled for six (6) samples that were tested in the gradient burner rig test. As discussed in the cyclic gradient burner rig testing section, samples were run at interface temperatures relevant to T1 and T2, respectively. The vane design for the NASA HyTEC Vision Engine is uncooled, so the gradient through the EBC is small. For both tests, the gradient burner rig fuel flow and backside cooling were adjusted to achieve the target interface temperature with minimal gradient. The interface temperature was estimated using 1-D heat flow calculations using the thermal conductivities of the CMC and the EBC layers, with the front and backside pyrometer measurements as input. Since the temperature gradient is small, any error in the estimation would be small. For the samples run at the interface temperature relevant to T1 for 25 through 75% of planned cycles, there was no spallation nor any evidence of macroscopic distress after the testing, as shown in the photographs in Figure 49. The sample that was intended to run 100% pf planned cycles at an interface temperature relevant to T1 failed by spallation after 86% of the total planned cycles. The sample that was intended to run 100% of planned cycles at an interface temperature relevant to T2 failed at 56% of total planned cycles due to cracking of the CMC material.

Table 24. Results for gradient burner rig testing

Target Life	25%		50%		75%		100%	
Actual Life	25%		50%		75%		86%	
Interface Temperature	**Sample ID**	**% spalled**	**Sample ID**	**% spalled**	**Sample ID**	**% spalled**	**% spalled**	**% spalled**
T1	NH136	0	NH141	0	NH133	0	NH113	5
	-	-	NH142	0	-	-	-	-
T2					-	-	NH139	0

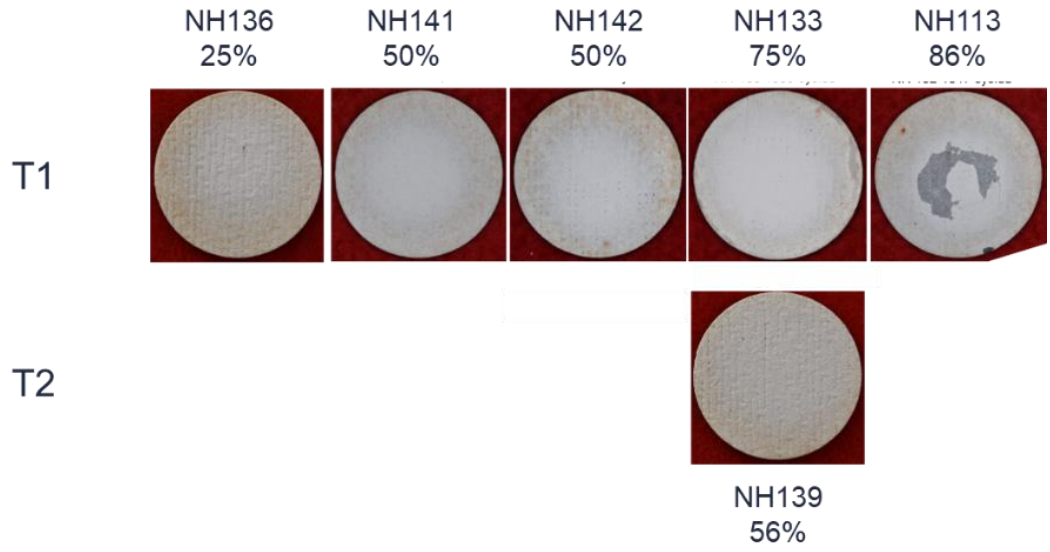

Figure 49. Photographs of samples after gradient burner rig testing

Microstructural assessment was completed on all of the post-test samples, and inferences on mechanisms contributing to damage progression in the gradient burner rig test were documented. No CMC oxidation was noted after any of the exposures. Damage accumulation during the test resulted in an increase in the pyrometer readings on the front side of the sample and on the backside of the sample. This increased the error in the sample temperature control during the test after the damage occurred. However, since the temperature control scheme was to control the interface temperature, which was close to the average of the front and backside temperatures due to the low temperature gradient through the sample, this increase in error in controlling the interface temperature was small.

Gradient burner rig testing with a topcoat bondcoat interface temperature of T2

The test was halted due to a large vertical crack that formed in the CMC material across the diameter of the sample. At the time the test was stopped, there was very little damage accumulated in the EBC.

High velocity steam jet testing

Table 25 lists the temperature, sample IDs, water flow rate and exposure time of the samples that were tested in the high velocity steam jet test rig. There was no spallation on any of the samples, but samples did exhibit recession of the topcoat material due to reaction with the water vapor.

A computational fluid dynamics (CFD) software package was used to predict the velocity distribution of water vapor on the sample surface as a function of the testing parameters listed in Table 25. Figure 50 shows a comparison of BSE SEM images of the surface of the 9 samples that were tested with the higher level of water flowrates to predictions of the size and shape of the recessed area based on the CFD calculations. The recessed zone shows good contrast in BSE SEM imaging, since water vapor recession removes silica from the coating, leaving behind hafnia rich material, which has a higher average atomic number, thus brighter contrast in BSE SEM images. Very good agreement was noted between the CFD prediction and the experimental data.

Table 25. Exposures completed on each sample in the high velocity steam jet test rig

Temperature	Sample ID	Water flow rate	Time (h)
T3+90 F	NH-150	High	Low
T3+90 F	NH-143	Low	Medium
T3+90 F	NH-148	High	Medium
T3+90 F	NH-162	High	High
T2	NH-151	High	Low
T2	NH-157	Low	Medium
T2	NH-161	High	Medium
T2	NH-149	High	High
T1	NH-145	High	Low
T1	NH-155	Low	Medium
T1	NH-144	High	Medium
T1	NH-146	High	High

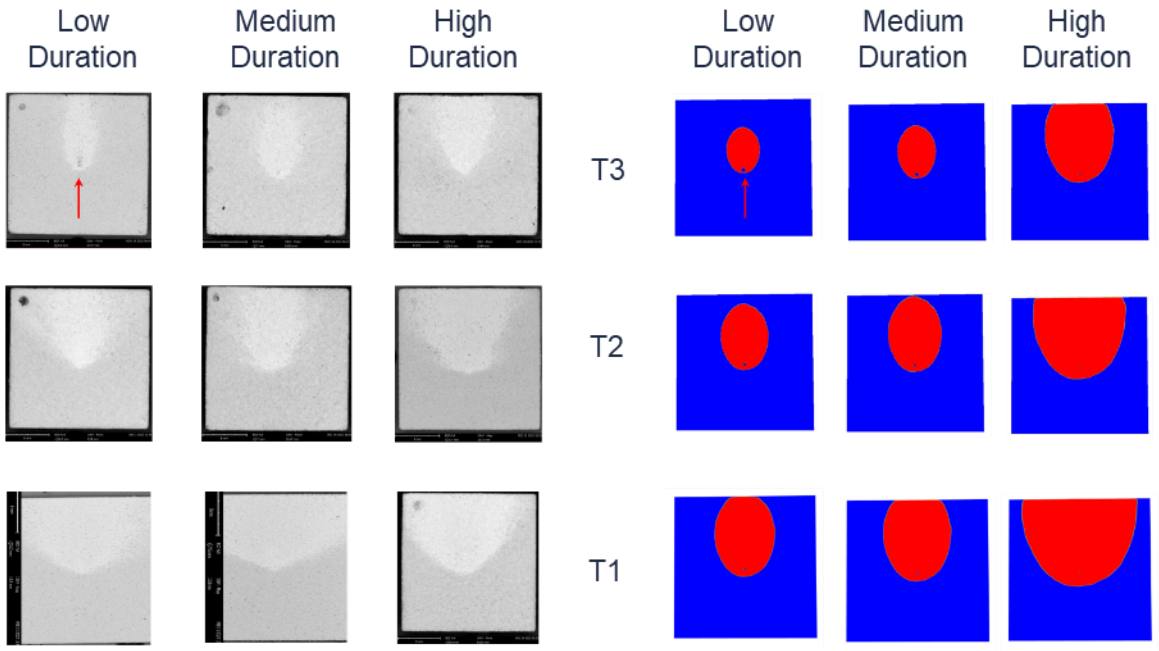

Figure 50. Comparison of BSE SEM images of samples that were tested in the high velocity steam jet rig with the higher water flowrates (left) to CFD-predicted recessed areas (right)

To determine the maximum depth to which recession of the topcoat occurred, tested samples were sectioned through the middle of the recessed zone, mounted, and polished for metallography. BSE SEM micrographs were taken on all of the cross sections and an image analysis routine was used to determine the average penetration depth in the location on each cross section that had the deepest recession. The recessed zone of the APS topcoat appears to have excellent mechanical integrity.

The CFD model was used to predict the penetration depth of recession using the classic model of gas-phase diffusion-controlled recession of $SiOH_4$. The mass loss due to recession predicted by that classic model is listed in equation 1. The recession depth measured by image analysis after a low duration exposure with the sample held at T2 and the high level of water flowrate was used to calibrate the CFD model to enable it to predict recession penetration depth.

Equation 1

$$\Delta M = \sim v^{0.8} \frac{exp\left(\frac{-\Delta G^{\circ}}{RT}\right) p_{H2O}^{2} a_{SiO2}}{P^{0.2}} \cdot t$$

Figure 51 shows the comparison between the penetration depth that was measured experimentally to the penetration depth predicted by the CFD code, for the T2 exposures that were run with the high level of water flow rate. The agreement between experiment and the CFD model is quite good. The model overpredicts water vapor recession, especially after longer exposures. This is attributed to the assumption in the model of a perfectly symmetric velocity distribution on sample surfaces. Effects such as surface roughness and chemical heterogeneity likely lead to spreading of the steam velocity distribution, which would then lead to reduced depth of penetration over long term exposures. Figure 51 provides evidence for this, in that the imaged recessed areas are clearly wider than the areas predicted by CFD.

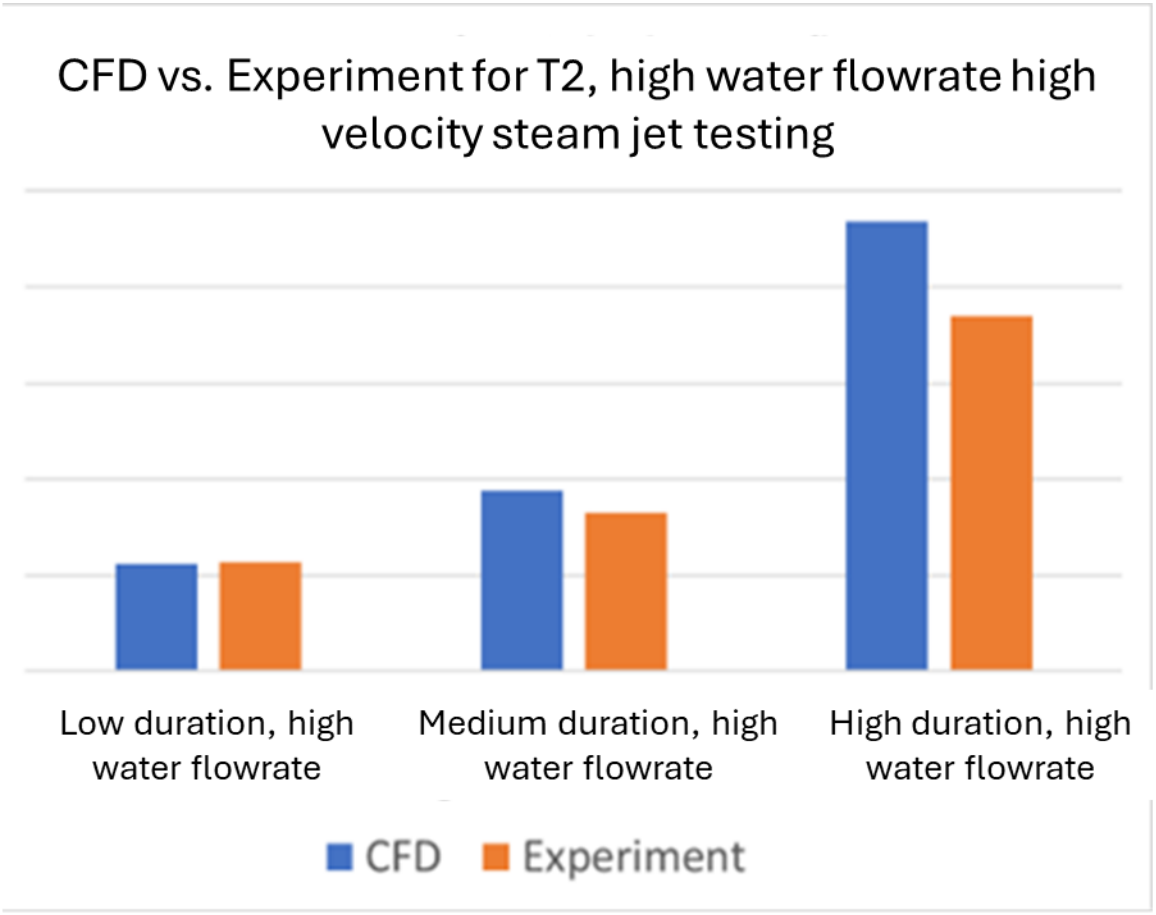

Figure 51. Comparison of experimentally measured penetration depth at T2 and the high level of water flowrate to the penetration depth predicted by the calibrated CFD model

Figure 52 shows the comparison of experimentally measured penetration depth at T1 and the higher level of water flowrate to the penetration depth predicted by the calibrated CFD model. The sign and magnitude of the difference between the CFD model prediction and the experimental measurements varied from condition to condition at this higher temperature condition. Further investigation beyond the scope of this report would be necessary to better understand this variation. Nevertheless, the overall agreement between the CFD model is quite good, validating the assumption of gas-phase diffusion controlled water vapor recession of the topcoat.

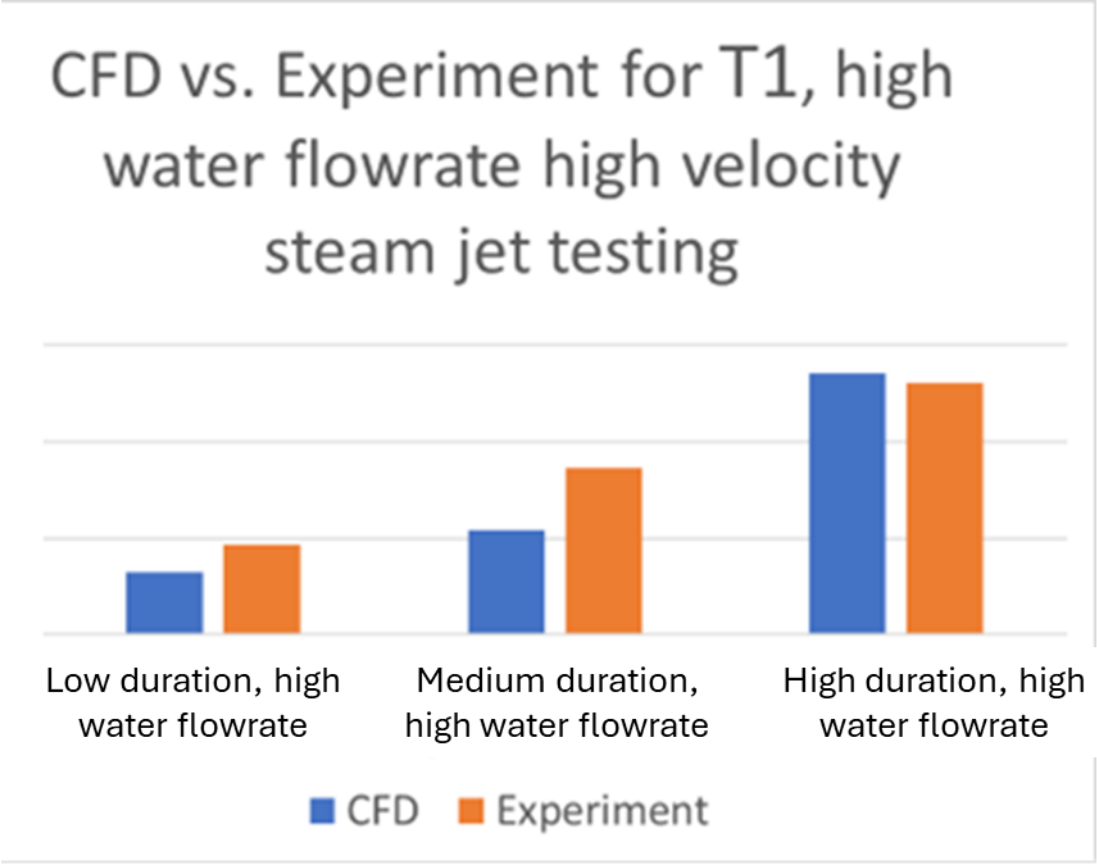

Figure 52. Comparison of experimentally measured penetration depth at T1 and the higher level of water flowrate to the penetration depth predicted by the calibrated CFD model

3.2.4.6 Task 2.2.5 Steam furnace cycle testing of P&W EBCs in the NASA Steam FCT rig

T1 + 100 F Steam furnace cycle testing of P&W EBCs in the NASA Steam FCT rig

As shown in Table 26, all 3 samples for which t1 hours and cycles were planned in the T1+100 F test were tested for t1 hours. Similarly, all 3 samples for which 2.7*t1 hours and cycles were planned were tested for that duration. However, none of the three samples that were planned to run for 5*t1 hours and cycles at T1+100 F survived that long. 1 sample failed after 2.6*t1 hours and cycles, and the other two failed after 4.2*t1 hours and cycles. The 3 samples that had been planned to test to failure were not run, since the failure life for the Gen 1.2 P&W EBC appears to be less than 5*t1 hours and cycles under these conditions. Failure in this longest duration group consisted of spallation of the EBC from the CMC. Prior to spallation, the EBC protected the CMC substrate from oxidation well.

Table 26. Results for Task 2.2.5 T1 + 100 F NASA steam furnace cycle testing of P&W EBCs

Target Life	t1 hours and cycles		2.7*t1 hours and cycles		5*t1 hours and cycles	
	Sample ID	Life demonstrated (hours and cycles)	Sample ID	Life demonstrated (hours and cycles)	Sample ID	Life demonstrated (hours and cycles)
	NH-91	t1	NH-114	2.7*t1	NH-94	2.6*t1
	NH-105	t1	NH-123	2.7*t1	NH-115	4.2*t1
	NH-116	t1	NH-99	2.7*t1	NH-121	4.2*t1

Based on a comparison of the post-test microstructures of all the samples listed in Table 26 to previously reported post-test microstructures of samples tested under similar conditions in the RTRC Steam FCT rig under Task 2.2, the failure modes and damage accumulation rates observed in T1+100 F Steam FCT testing were similar in both rigs. There were some subtle differences observed in damage accumulation rates that were attributed to the differences in cycling frequency. This suggests that longer exposures between cycles is slightly more damaging for the P&W EBC bondcoat.

T2 Steam furnace cycle testing of P&W EBCs in the NASA Steam FCT rig

Table 27 lists the target life, actual life, and sample identification numbers for the samples that were tested at T2 in the Steam furnace cycle testing (FCT) rig at NASA Glenn Research Center. All samples survived the planned exposures with only minor damage. In contrast, in Task 2.2 the topcoat had spalled from the bondcoat after the longest exposures. Samples that were planned to run to failure in Task 2.2.5.1 failed after only slightly longer exposures than the 3.75*t2 group, so no additional characterization was completed.

Table 27. Results for Task 2.2.5 T2 NASA steam furnace cycle testing of P&W EBCs

Target Life	t2 hours and cycles		1.75*t2 hours and cycles		3,75^t2 hours and cycles	
	Sample ID	Life demonstrated (hours and cycles)	Sample ID	Life demonstrated (hours and cycles)	Sample ID	Life demonstrated (hours and cycles)
	NH-101	t2	NH-96	1.75*t2	NH-92	3.75*t2
	NH-109	t2	NH-97	1.75*t2	NH-100	3.75*t2
	NH-117	t2	NH-113	1.75*t2	NH-102	3.75*t2

Based on post-test microstructural comparisons, the failure modes and the rate of damage progression was very similar between the NASA rig used in Task 2.2.5.1 and the RTRC rig used in Task 2.2 for testing at T2.

3.2.4.7 Task 2.2.5 Steam furnace cycle testing of NASA EBCs in the NASA Steam FCT rig

T3 Steam furnace cycle testing of NASA EBCs in the NASA Steam FCT rig

All samples were tested for the full durations planned as listed in Table 12 with no full-scale spallation. Predominantly, the NASA EBC exhibited little distress after all exposures Some damage to the EBC topcoat was visually evident after the 5*t3 exposure at edges of elevated fiber tows in the CMC. In other words, the steep and deep features on the CMC surface due to the weave of the CMC fabric tended to damage the EBC layer. Cross sections through the EBC indicated that at locations where the EBC was damaged due to the CMC surface roughness, there was also damage of the CMC material.

After the 10*t3 exposure, the damaged locations at the edges of fiber tows and in deep valleys between the tows progressed into spalls of the EBC from fiber tows on the surface. Again, microstructural characterization indicated that in locations unaffected by deep and steep surface features, the NASA EBC showed very little damage and protected the CMC well. There was evidence of interaction with the water vapor environment at the surface of the EBC in the microstructural cross sections, but only a small fraction of the EBC thickness was affected.

Task 2.2.5 T2 Steam furnace cycle testing of NASA EBCs in the NASA Steam FCT rig

All samples were tested for the full durations planned as listed in Table 12 with no full-scale spallation. Predominantly, the NASA EBC exhibited little distress after all exposures Some damage to the EBC topcoat was visually evident after the 5*t3 exposure at edges of elevated fiber tows in the CMC. In other words, the steep and deep features on the CMC surface due to the weave of the CMC fabric tended to damage the EBC layer. Cross sections through the EBC indicated that at locations where the EBC was damaged due to the CMC surface roughness, there was also damage of the CMC material.

In contrast to the result discussed above for testing at T1, after the 10*t3 exposure at T2, the damaged locations at the edges of fiber tows and in deep valleys between the tows did not progress into spalls of the EBC from fiber tows on the surface. Again, microstructural characterization indicated that in locations unaffected by deep and steep surface features, the NASA EBC showed very little damage and protected the CMC well. There was evidence of interaction with the water vapor environment at the surface of the EBC in the microstructural cross sections. Again, only a small fraction of the EBC thickness was affected. Compared to the result from the T1+100 testing discussed above, the volumes of EBC affected by this mechanism appeared to be larger and thicker after T2. However, this observation was based on only a few micrographs, so more investigation is warranted to confirm this.

3.2.5 Conclusions and key takeaways

- In all testing completed in Task 2.2, no significant TGO growth occurs on the CMC SiC layer
- Saturated steam conditions dramatically accelerate oxidation and depletion of gettering phases as compared to ambient air testing under the same conditions
- Gettering phase depletion rates in ambient air exposures are higher at higher temperature
- Gettering phase depletion rates are higher for FCT testing vs. static exposures at the same temperature for ambient air exposures

- Image analysis indicates that none of the exposures that were completed in Task 2.2 had a measurable effect on the percentage of porosity in the bondcoat, since the variability in the porosity from sample to sample overwhelmed any systematic effects.
- Careful measurement of the area and penetration depth of the recessed volume of the topcoat provides the data needed to calibrate a CFD model to predict water vapor recession as a function of location on the part

Comparison of NASA Steam FCT testing of P&W EBCs under Task 2.2.5 to RTRC Steam FCT testing of P&W EBCs under Task 2.2.

The failure modes that were observed in both the NASA and RTRC test rigs were very similar. At both temperatures tested, the P&W EBCs exhibited significant damage after even the shortest exposures in the test plan, as had been observed in Task 2.2. As had been the case in Task 2.2, the damage accumulation rate in both rigs was much faster at the lower temperature (T2). Especially at the higher temperature, the rate of damage accumulation was marginally higher in the RTRC rig as compared to the NASA rig. This was attributed to the slower cycling frequency in the RTRC rig as compared to the NASA rig.

Comparison of NASA Steam FCT testing of NASA EBCs under Task 2.2.5.2 to NASA Steam FCT Testing of P&W EBCs under Task 2.2.5.

On the majority of the sample surface area, the NASA EBC was well adhered and exhibited very little damage after the longest durations at both temperatures. The CMC was well protected in those locations. There was some evidence of interaction with the steam environment on the surface of the NASA EBC after the longest exposure. The volume of EBC at the surface that was affected by this interaction appeared to be higher at the lower test temperature.

Steep and deep features due to the weave of the CMC preform fabric led to damage of the NASA EBC layers. Damage of the CMC was evident at these locations after the 5*t3 exposures at both temperatures. After the longest exposure at the higher temperature, the NASA EBC spalled from several surface most fiber tows, leading to apparent damage of the CMC. This spallation mode did not occur after the longest exposure at the lower temperature.

Going forward, the failure mechanisms of the P&W EBC in the temperature regime that was tested in this task must be eliminated. Either the deep and steep features on the CMC surface need to be eliminated to leverage the NASA EBC, or its processing must be made more robust to surface features.

3.3 TASK 2.3 HIGH TEMPERATURE CMC VANE DESIGN & VALIDATION

3.3.1 Task Overview

For Task 2.3, the objective of testing and analysis was to (1) identify the onset of CMC failure modes, confirm degradation mechanisms, and quantify their rate of progression, (2) to provide further insight into critical CMC material and design parameters that affect the durability of CMC turbine vanes, and (3) understand how parameters can be optimized for improved CMC durability. Specifically, testing under the HyTEC program was intended to investigate the operational regimes of the oxidation mechanism over a range of temperatures and determine how oxidation interacts with thermomechanical degradation (cracking and creep).

3.3.2 Test planning and pre-test analysis

The key performance metric of this task is to demonstrate that a CMC component can meet the efficiency requirements of the HyTEC concept engine for a static high-pressure turbine (HPT) component, specifically the second turbine vane (HPT 2V) in the next generation single aisle (NGSA) engine offering. The key performance metrics of 10% fuel burn reduction, >50 overall engine pressure ratio, and meeting or exceeding 20k operating hours between refurbishments are accomplished by the component-level technical merits. The component-level technical metrics of this task is to demonstrate operability and durability of a CMC turbine airfoil at increased temperature capability, reduced cooling flow, and weight reduction versus equivalent metal alloy components.

To demonstrate and validate these metrics, P&W and RTRC has designed and built the High-Pressure Thermal Cycling (HPTC) rig for testing HPT airfoil-shaped articles at engine-relevant pressures and temperatures and cyclic thermodynamic excursions typical of commercial and military aircraft engines, with matched Reynolds, Biot, and Mach numbers. This rig was originally designed and fabricated for high pressure and high temperature durability/endurance testing of straight teardrop-shaped CMC sub-elements under a previous NASA contract (NNC15BA06B / NNC16TA04T). The current turning vane configuration was designed and fabricated by RTRC and funded by P&W to achieve aircraft engine-relevant turbine operating conditions, flowpath, and geometry. The HPTC has a single element cascade geometry for testing a single 2D-extruded CMC turbine airfoil shape or sub-element. A solid (CAD) model of the rig is shown in Figure 53. In this figure, flow is from left to right. High pressure electrically heated air is supplied to the rig centerline and mixed with compressed natural gas through a fuel-air manifold and burner (blue-green) which consists of a 3x5 array of mixing tubes. The fuel-air mixture is ejected into the downstream region of the mixing flange (light-green) and ignited. The combustion products enter the pressure vessel test section (orange) and are accelerated by a water-cooled inlet duct (light purple) to the desired Mach number. The CMC airfoil test article (gray) sits in an air-cooled vane holder (cyan). The vane holder and CMC turn the core flow 20-deg where the side walls of the vane holder were designed to match the Mach number, temperature, and pressure distributions of the NGSA's 2nd turbine vane. The core flow past the test article is expanded by the water-cooled exit diffuser (blue) and leaves the test section where it passes through a flange to the dump section (yellow), quenched, and ejected to atmosphere. This figure also shows 6 pyrometer ports and sight tubes for monitoring the temperature of the CMC test article as well as tubes for fuel intake, igniter, water cooling inlet and outlet, and instrumentation ports for gas temperature and pressure measurements with thermocouples (TCs) and pressure transducers.

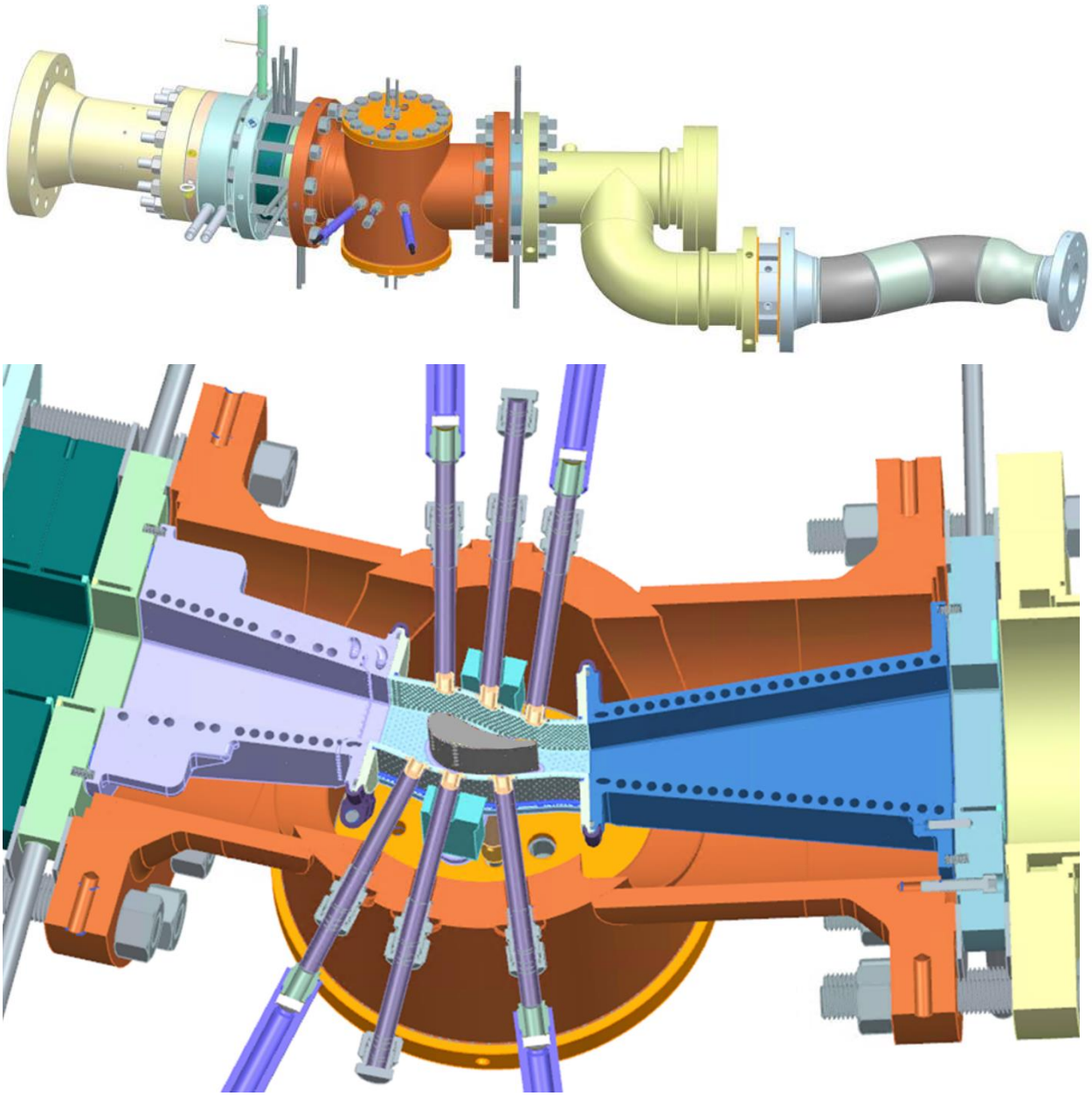

Figure 53. Solid model of HPTC rig overview (top) and cross-section (bottom)

The objective of testing and analysis is to (1) demonstrate the enhanced temperature capability of CMCs, an increase of 300 to 500F over the single crystal metal vanes, 2) demonstrate reduced cooling air flow, a reduction of ~2.5%, 3) identify the onset of CMC failure modes and confirm degradation mechanisms observed in coupon testing task 2.1 under engine operating conditions as well Specifically, testing under the HyTEC program was intended to investigate the operational regimes of the oxidation mechanism over a range of temperatures and determine how oxidation interacts with thermomechanical degradation (cracking and creep). Figure 54 illustrates the various regimes of damage/ degradation mechanisms of P&W's CMC material as a function of temperature and stress. This figure identifies the degradation mechanisms of oxidation, creep, crack growth, and IFC recession, as well as the self-healing

mechanism of crack sealing. A thermomechanical cycle from A to B with a short exposure to high temperature may result in limited creep with crack sealing by oxidation which prevents further ingress of oxygen. However, a thermomechanical cycle from C to B with rapid heating may build thermal stress and advance cracks through the matrix below its softening temperature. HPTC test points will be chosen after predicting temperatures and stresses at each of the relevant engine conditions that include both normal HyTEC operating conditions and accelerated conditions to test out the failure modes.

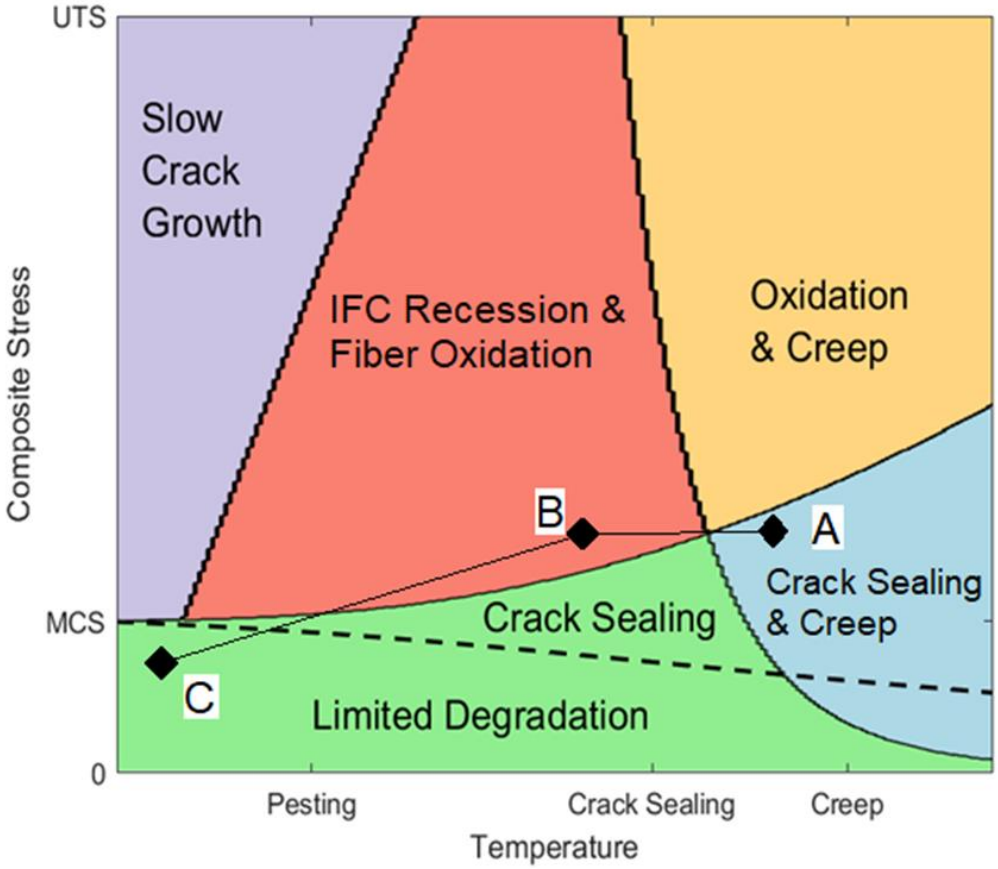

Figure 54. Illustration of regimes of CMC damage mechanisms as a function of temperature and composite stress and thermo-mechanical cycles

The CMC test articles were fabricated using P&W's Gen 1.2 (TRL/MRL-4) SiC-SiC CMC material with 8HS weave architecture, CVI interface coating, and CVI SiC matrix and seal coat. This phase I testing program leverages prior P&W CMC testing through TRL4. The material properties (thermal conductivity, coefficient of thermal expansion and modulus of elasticity) of this material system were measured and are provided in Figure 55. Here, _x represents in-plane (fiber tow or ply direction) properties and _z represents transverse through-wall (interlaminar) properties. Mass density of the CMC was measured as 0.09429 lbm/in^3. Poisson's ratio was measured as 0.092 in-plane and 0.100 through-wall. The stress-strain curves of this material at various temperatures and exposure times are shown in Figure 56. The vertical axis is the composite stress. Notice that thermal exposure results in improved tensile strength and strain to failure suggesting there is a beneficial oxidation mechanism. Material properties were normalized by values for a reference nickel alloy material and temperature was normalized by a maximum value, Tmax.

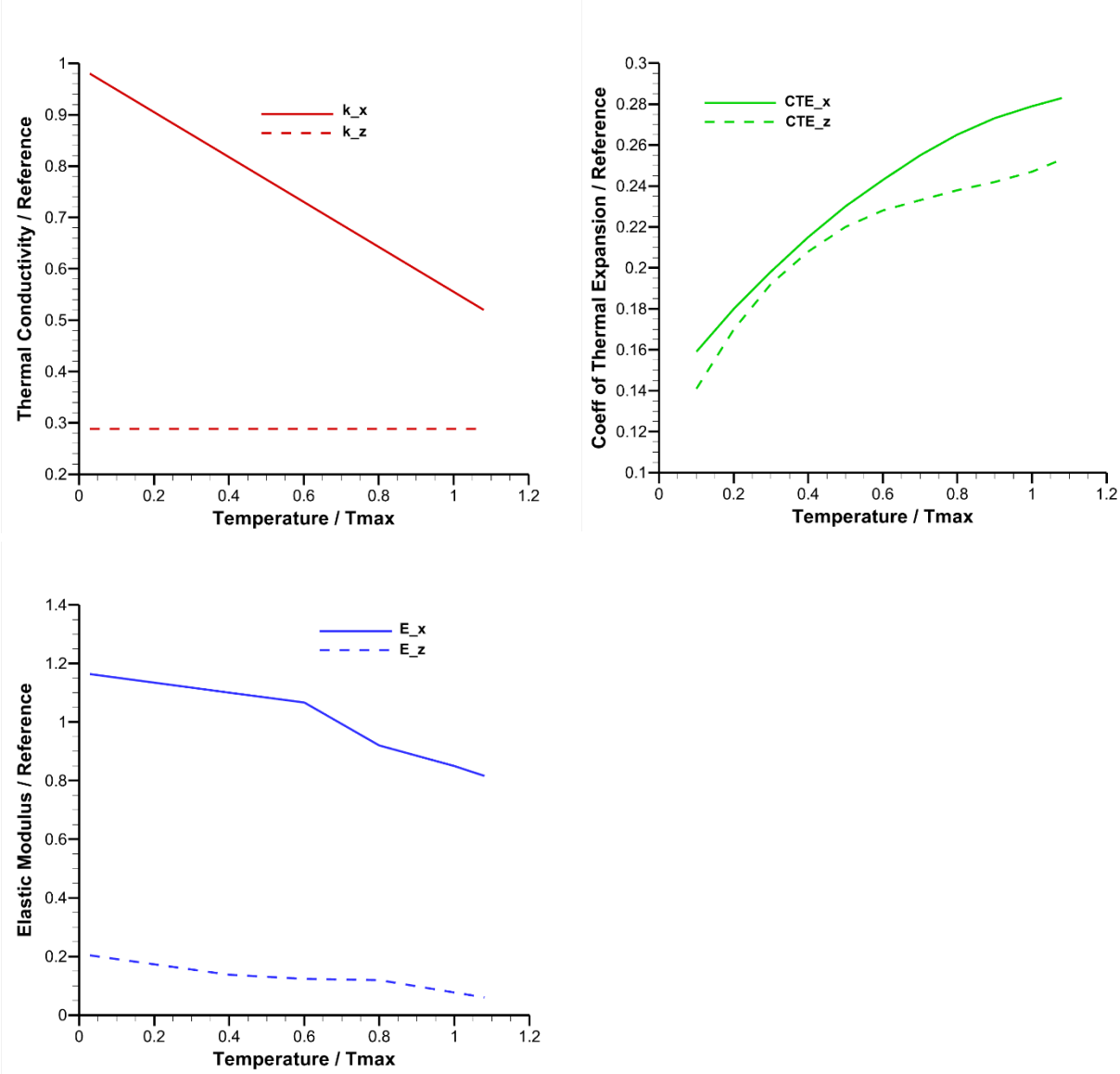

Figure 55. Materials properties of P&W's Gen1.2 (TRL/MRL4) SiC-SiC CMC normalized by a reference alloy property versus temperature normalized by maximum CMC temperature

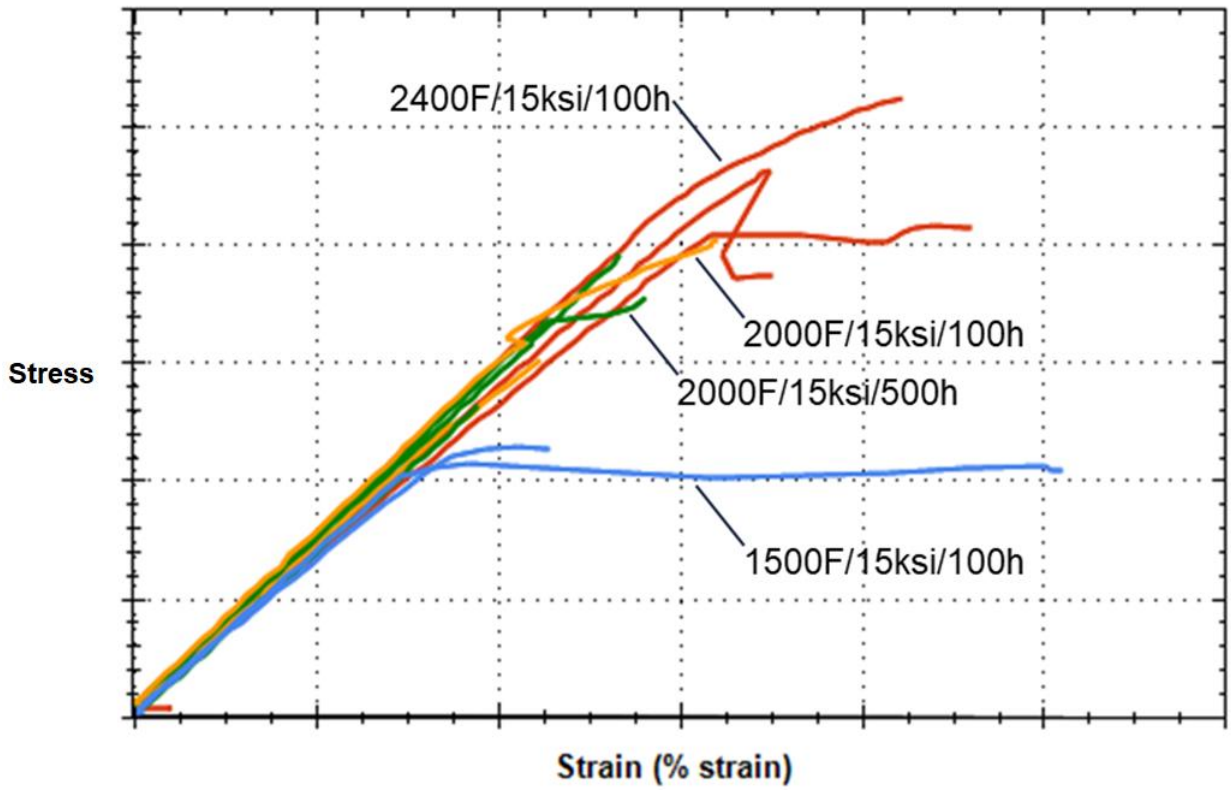

Figure 56. Stress-strain curves of P&W's Gen 1.2 (TRL/MRL-4) SiC-SiC CMC

The solid model of the CMC test article is shown in Figure 57. All CMC plies (green/blue) were modeled explicitly as 8 layered bodies with a nominal ply thickness and meshed with brick (hexahedral) finite elements. Two overwrap plies (blue) and the remaining internal plies (green) were differing weave architectures. This model has separate bodies to fill in gaps between the plies at the rib and trailing edge which were filled with fiber tows called noodles (orange). The model also included the outer and inner layers of SiC (dark gray). Orthotropic material properties were applied locally within each body-conforming coordinate system. Figure 57 also shows the outer environmental barrier coating (EBC) layer (light gray). This EBC consisted of a bond coat and $HfSiO_4$ topcoat with respective thermal conductivities.

The airfoil shape of the CMC test article was derived from the 2nd stage turbine vane of the NGSA HyTEC concept engine. The airfoil section at the midspan was extruded to a test article that spanned the HPTC test section. The model of the airfoil wall consisted of multiple layered plies of the CMC with SiC inner and outer layers. The airfoil's internal structure consisted of one structural support rib which separated the leading and trailing edge cavities.

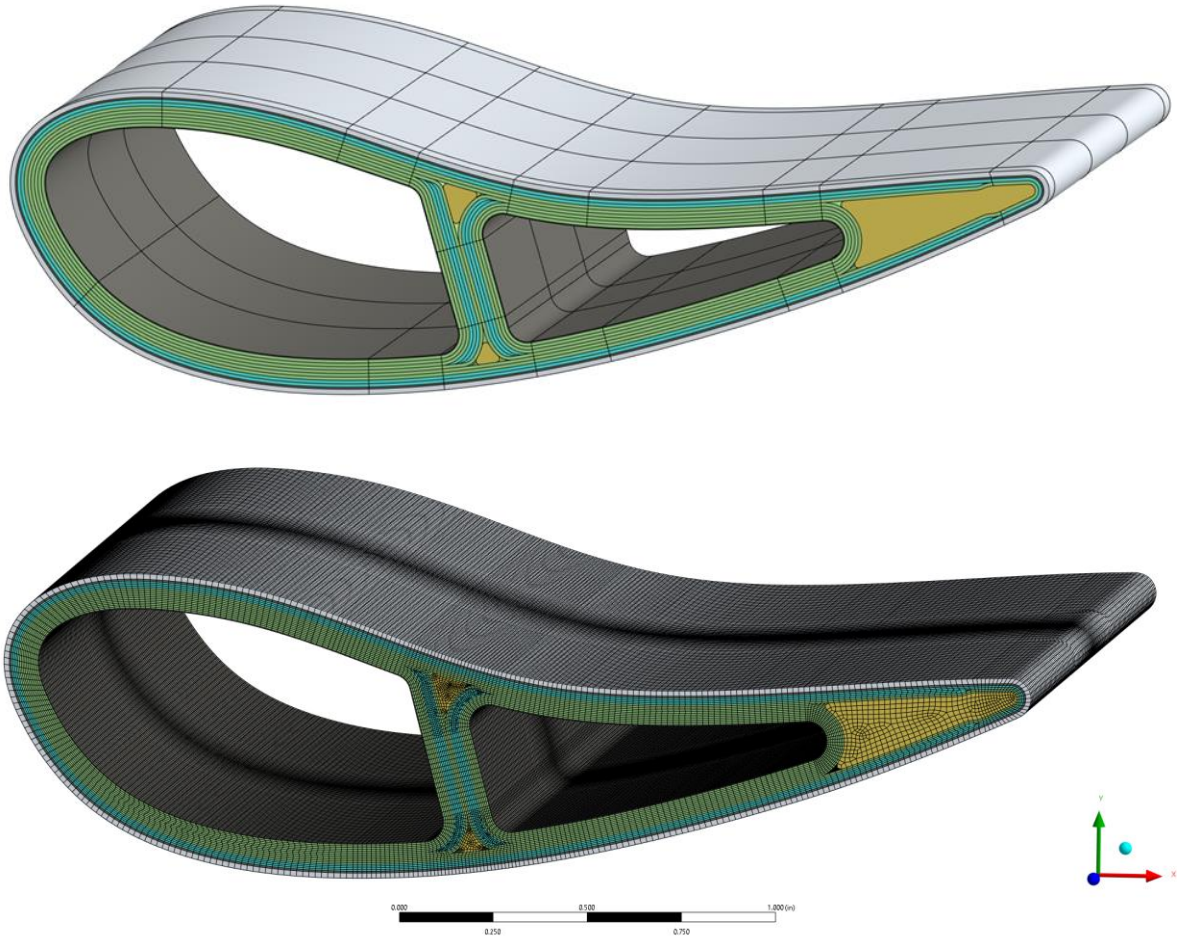

Figure 57. CAD model and finite element mesh showing plies, fillers, and layered bodies of CMC vane for HPTC rig testing.

Thermomechanical simulations of CMC test articles were done to predict the material response at rig conditions for design validation, risk reduction, and learning to improve materials. To accomplish these goals, we used the same design methods, analysis procedures, and computer simulation software of rig test articles as P&W turbine airfoils. The intent of the pre-test predictions was to determine requirements and effects of internal cooling, to predict locations and severity of damage mechanisms for instrumentation placement, to compare predictions with rig measurement data, and to better understand damage seen in post-test inspections.

The operating conditions for a commercial mission for the HyTEC Vision Engine Cycle are provided in Table 28. Here, P and T are flow-weighted averaged station total pressure and total temperature, W is the total core flow rate. The values in this figure have been non-dimensionalized by pressures, temperatures, and flow rates at the takeoff (TO) condition. Station 3 is compressor exit/combustor inlet, 4 is combustor exit/turbine inlet, and 45 is between the high and low turbine. Values with the subscript gas are the core gas pressures and temperatures at the inlet to the 2nd stage turbine vane. Values with the subscript cool are the cooling air pressures and temperatures to the 2nd stage turbine vane. These are shown in columns labeled idle, cruise, takeoff (TO) and durability design point (DDP) operating points, the latter being TO conditions of a deteriorated engine on a hot day.

Table 28. HyTEC Vision Engine Cycle

	Engine			
Condition	**Idle**	**Cruise**	**TO**	**DDP**
P3	0.099	0.370	1.000	0.968
P4	0.093	0.348	0.940	0.909
P45	0.031	0.081	0.224	0.217
Pgas	0.055	0.183	0.497	0.480
Pcool	0.061	0.229	0.620	0.600
P3/P4	1.062	1.064	1.064	1.064
T3	445	1005	1187	1271
T4	0.614	0.867	1.000	1.100
T45	0.391	0.537	0.642	0.716
Tgas	0.487	0.679	0.796	0.882
Tgas,hotspot	0.543	0.742	0.868	0.962
Tcool	0.147	0.340	0.402	0.492
Tcool/T3	0.924	0.945	0.948	1.082
(T4-Tgas)/(T4-T3)	0.279	0.371	0.354	0.339
W3 full	0.138	0.400	1.000	0.942

Gas temperatures, pressures and flow rates for CMC vane testing in the HPTC rig were derived from this commercial mission. The goal was to match (as closely as possible) the aerothermodynamic conditions of HPTC rig testing to the vision engine, specifically hot gas path temperatures, pressures, Mach numbers, flow turning and geometry, and consequently, heat loads, and hence testing the CMC material response and durability at the same or similar temperatures, temperature gradients, and stresses. This was accomplished through comparative modeling of the 2nd stage CMC turbine vane in the engine and in the HPTC rig.

The procedure for thermal-stress predictions in the CMC test articles is shown in Figure 58. Given engine or HPTC rig operating conditions and geometry model of the engine or rig flow path and airfoil, a CFD analysis of the hot gas (core) flow was executed. The model included the mixing region downstream of the burner, inlet contraction, vane holder, exit diffuser, and dump (see Figure 59). ANSYS Workbench and Fluent were used for this purpose. Each domain was meshed with mainly hexahedral elements and swept downstream with 18 elements for boundary layer inflation. The Reynolds Averaged Navier Stokes (RANS) equations were solved with the k-ω turbulence model. Total pressure and temperature were applied to the inlet from the burner and mass flow at the exit, and their profiles were initially specified to be constant. Thermal boundary conditions to the rig side walls and airfoil were generated by running 2 cases; the first with adiabatic wall boundary conditions where the CFD solves for the adiabatic wall temperature distribution, T_{aw}, and the second with applied wall temperature, T_w, where the CFD solves for heat flux density distribution, Q'', on the walls. Combining the 2 solutions was used to determine convective heat transfer distribution, $h=Q''/(T_{aw}-T_w)$.

Heat transfer models of the rig side walls and CMC airfoil test articles were analyzed with 3D FEM in ANSYS Mechanical. The finite element mesh consisted of 3M nodes and 1.1M quadratic elements. The plies were meshed primarily with hexahedral elements while the filler regions of the noodles were mostly tetrahedrons. The aerothermal heat load to the CMC airfoil and rig side walls was augmented by running P&W's proprietary thermal boundary layer solver which captures additional physics of turbine flow paths for heat transfer augmentation, h_{aug}, due to surface

roughness, and airfoil curvature, and mixing of hot gas with cooling air downstream of effusion/film cooling holes and slots using a P&W proprietary model for film effectiveness, $\eta_{film}=(T_{aw}-T_{film})/(T_{aw}-T_{cool})$, where applicable. Here, T_{film} is the film temperature due to the injection and T_{cool} is the local cooling air temperature. Thermal FEMs used the CFD-derived and augmented convective heat transfer boundary conditions, $Q''=h_{aug}(T_{film}-T)$. Thermal radiation between the CMC airfoil surface to the rig side walls was also included with constant surface emissivity, $\varepsilon_r=0.7$, for the thermal barrier coated rig side walls and $\varepsilon_r=0.8$ for the environmental barrier coated CMC.

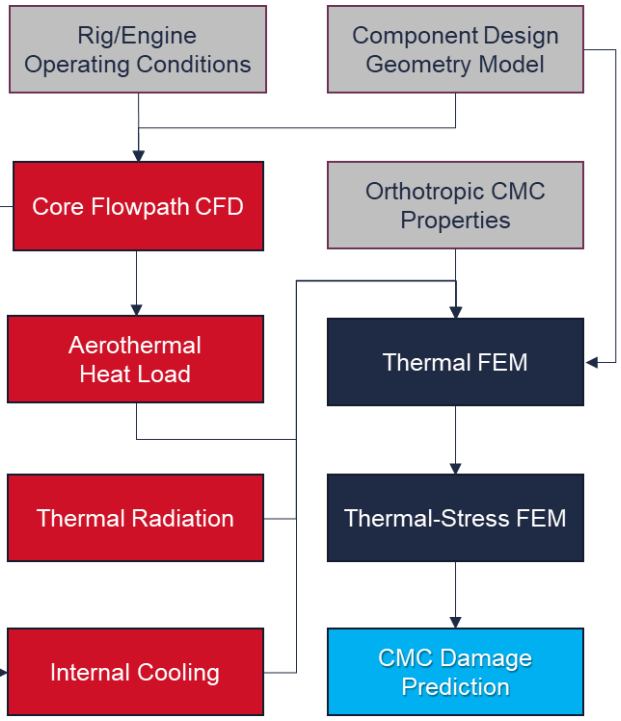

Figure 58. Procedure for thermal-stress predictions in CMC test articles

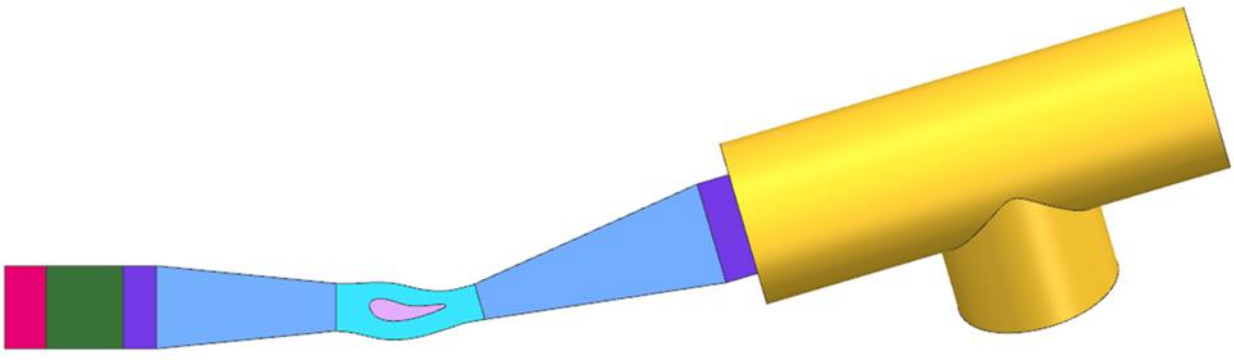

Figure 59. Zones of CFD model for HPTC rig

The internal convective cooling structure shown in Figure 60 was designed to evaluate the technical performance metrics of cooling air reduction and the potential for an uncooled CMC turbine vane. The CMC test article was supplied with cooling air through 2 inlet tubes to the leading and trailing edge internal cavities and exited the test article on the opposite side. The tubes had a throat diameter of 0.305” and 0.256” and passed through 13 and 8 0.100” diameter holes in the inserts to the leading and trailing edge passages, respectively. The inserts were offset 0.060” and 0.050” from the leading and trailing CMC internal surfaces. Heated cooling air was supplied from an 80 kW heater upstream and throat pressure and temperature were measured so cooling flow rates could be calculated. The design was intended to allow for precise control of relatively small cooling air flow rates by monitoring the pressure drop between the inlets and outlets and by a downstream venturi valve. The CMC vane’s internal cooling system was modeled using a P&W proprietary flow network solver. The nodes and elements of this cooling network including leading and trailing edge inlet and outlet tubes, passages, and leakages is shown in Figure 60. The dump pressures of the leading and trailing passages were controlled by the downstream valve, while those of the leakage paths were taken from the pressure distribution derived from the CFD solution of the rig flow path. The internal cooling network solver provided predictions for internal cooling air pressures, temperatures, and flow rates for each passage as well as distributions of gas temperature and heat transfer coefficients which were used as boundary conditions for the internal surfaces of the thermal FEM.

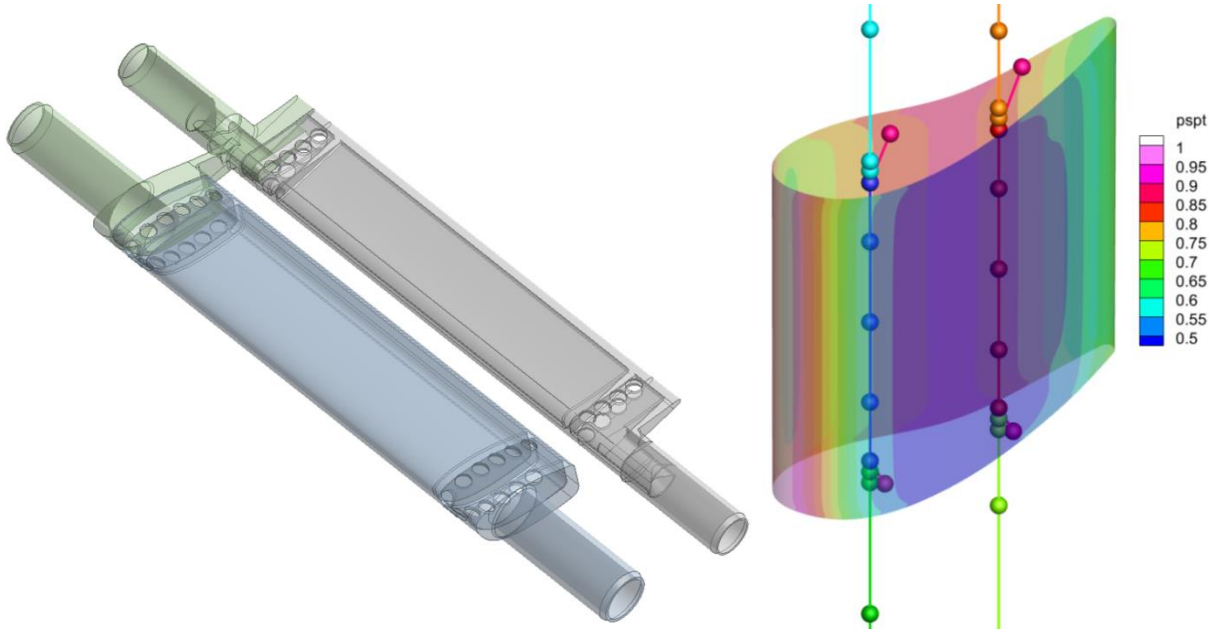

Figure 60. Internal cooling flow model and static pressure distribution on CMC airfoil surface

Pretest thermal and thermal stress models of CMC airfoil test articles were developed to derive HPTC rig test conditions. The pretest modeling process involved modifying the HPTC rig operating conditions until predicted temperatures, temperature gradients, and thermal stresses in the CMC test article matched, as closely as possible, those of the CMC 2nd turbine vane in the HyTEC concept engine at the cruise, climb, takeoff, and DDP operating conditions shown in Table 28. Specifically, supply total pressure, P3, total temperature, T3, air flow rate fuel, W1, and equivalence ratio, ϕ_{eqv}, were adjusted, resulting in derived values for total pressure, P4, and total temperature, T4, downstream of the burner. Pressure and temperature profiles at the inlet to the test section were derived from predicted values of heat transfer and injection of cooling air to the

rig side walls. Note that HPTC rig operability was limited by air flow to the burner, pressure losses in the piping system and across the burner, combustion stability, and lean blow out. Therefore, HPTC rig operating conditions were not known until they were verified by recently executed shakedown tests. This was ultimately an iterative process that involved HPTC rig shakedown testing by gathering information from thermocouples (TC), pressure taps (PT) and venturi meters (W), as shown in the instrumentation diagram, Figure 67, and listed in Table 30 , and which are described in the next section on instrumentation.

Pressure, temperature, and flow rate measurements during HPTC rig shakedown were applied as operating condition inputs for the generation of thermal and mechanical boundary conditions to the pretest thermal and thermal stress models of the CMC test articles. These pretest analyses were done to provide feedback and target operating conditions to the rig operators for HyTEC testing of the CMC vane test articles.

The plan for HyTEC testing consists of 3 test cases each replicated twice for 6 CMC vane test articles. The test cases were selected to study various CMC damage modes which would be activated during commercial aircraft engine operation. The HPTC rig operating conditions that correspond to the HyTEC Vision Engine cycle are shown in Table 30 . Compare to Table 28 for the engine cycle.

HPTC rig operating conditions are shown in Table 29 for the test cases and equivalent engine conditions, which are labeled Climb (1A), DDP (2B), Takeoff (3B) and Cruise (3B). Here, DDP is the durability design point, which is a takeoff point at a deteriorated high temperature state. Since the main purpose of using a high temperature CMC airfoil in the 2nd stage turbine vane is to minimize the cooling air requirements, two internal cooling schemes were derived for HPTC rig testing called nominal (A) and minimal (B) cooling. Nominal cooling corresponds to an internal cooling flow rate typical of metal alloy turbine airfoil. Minimal cooling corresponds to an uncooled CMC turbine airfoil. In the latter, a small amount of cooling air will be supplied to the CMC vane to account for the cooling air bypass and engine vibration. Pressures in this table have been non-dimensionalized by the supply pressure at takeoff conditions (P3). Temperatures were non-dimensionalized by the maximum CMC temperature (Tmax). Flow rates have been non-dimensionalized by the air flow rate at takeoff conditions (W1).

Test 1A corresponds to the damage mode of CMC matrix cracking without oxidation (pesting) at the Climb operating point with nominal internal cooling. Test 1A is characterized by a moderate material temperature (internal CMC surface), high thermal gradient (through CMC wall), and high thermal stress (tensile hoop stress at innermost CMC ply). Test DDP 2B corresponds to the damage mode of CMC matrix oxidation at the DDP operating point with minimal internal cooling and is intended to demonstrate the potential for matrix crack healing. Test DDP 2B is characterized by a high material temperature, moderate thermal gradient, and moderate thermal stress. Test 3B involves thermal cycling between cruise and takeoff operating points with minimal internal cooling. Test 3B is characterized by moderate (Cruise) to high (Takeoff) material temperature and from low (Cruise) to moderate (Takeoff) thermal stress but below the CMC matrix cracking limit. Tests involving minimal cooling remain below the matrix cracking limit.

Table 29. HPTC Rig Operating Conditions for HyTEC Testing

	HPTC Rig			
Condition	**Climb (1A)**	**DDP (2B)**	**Takeoff (3B)**	**Cruise (3B)**
P3	0.833	1.000	1.000	0.533
P4, Pgas,avg	0.800	0.967	0.967	0.500
Pcool	1.000	1.105	1.105	0.600
P3/P4	1.042	1.034	1.034	1.067
T3	0.320	0.320	0.320	0.320
ϕ_{eqv}	0.52	0.57	0.54	0.38
T4, Tgas,avg	1.108	1.1748	1.134	0.9076
Tcool	0.300	0.300	0.300	0.300
W1	0.760	1.000	1.000	0.400
Wcool	0.076	0.029	0.029	0.054

Figure 61 illustrates pretest aerothermal predictions for the CMC test article in the HPTC rig at the Climb 1A operating condition. Figure 62 illustrates pretest aerothermal predictions for the CMC test article in the HPTC rig at the DDP 2B operating condition. These figures show the CMC/EBC interface temperature, TEMP non-dimensionalized by the maximum CMC temperature, Tmax, external EBC (topcoat) temperature, TWALL /Tmax, temperature difference in CMC between outer (airfoil) and inner (cooling) surfaces, DELTAT, total surface heat flux, QW=CONV1*(CONV2-TWALL), applied external heat transfer coefficient, CONV1, and applied adiabatic wall temperature, CONV2. These figures also show the location of the pyrometer focal areas on the airfoil surface as black outlined elements. Post-processing of temperatures TEMP and TWALL in these regions provides comparisons to pyrometer measurements.

The Climb 1A operating condition is the test point with the highest thermal stresses in the CMC test article due to the high gas temperature (CONV2) and nominal internal cooling. As a percentage of the maximum allowable CMC temperature, the CMC/EBC interface temperature (TEMP) reaches 87% at the midspan leading and 92% at the trailing edge and the EBC topcoat temperature (TWALL) reaches 96% at these locations. Through-wall thermal gradients (DELTAT) are the highest of all tests (excluding rib and trailing edge). The DDP 2B operating condition is the test point with the highest temperatures in the CMC test article due to the highest gas temperature (CONV2) and minimal internal cooling. The CMC/EBC interface temperature (TEMP) reaches 10 0 % at the midspan leading and exceeds it at the trailing edge and the EBC topcoat temperature (TWALL) reaches 95% of its limit at these locations. Through-wall thermal gradients (DELTAT) are about half as much as the Climb 1A condition (excluding rib and trailing edge).

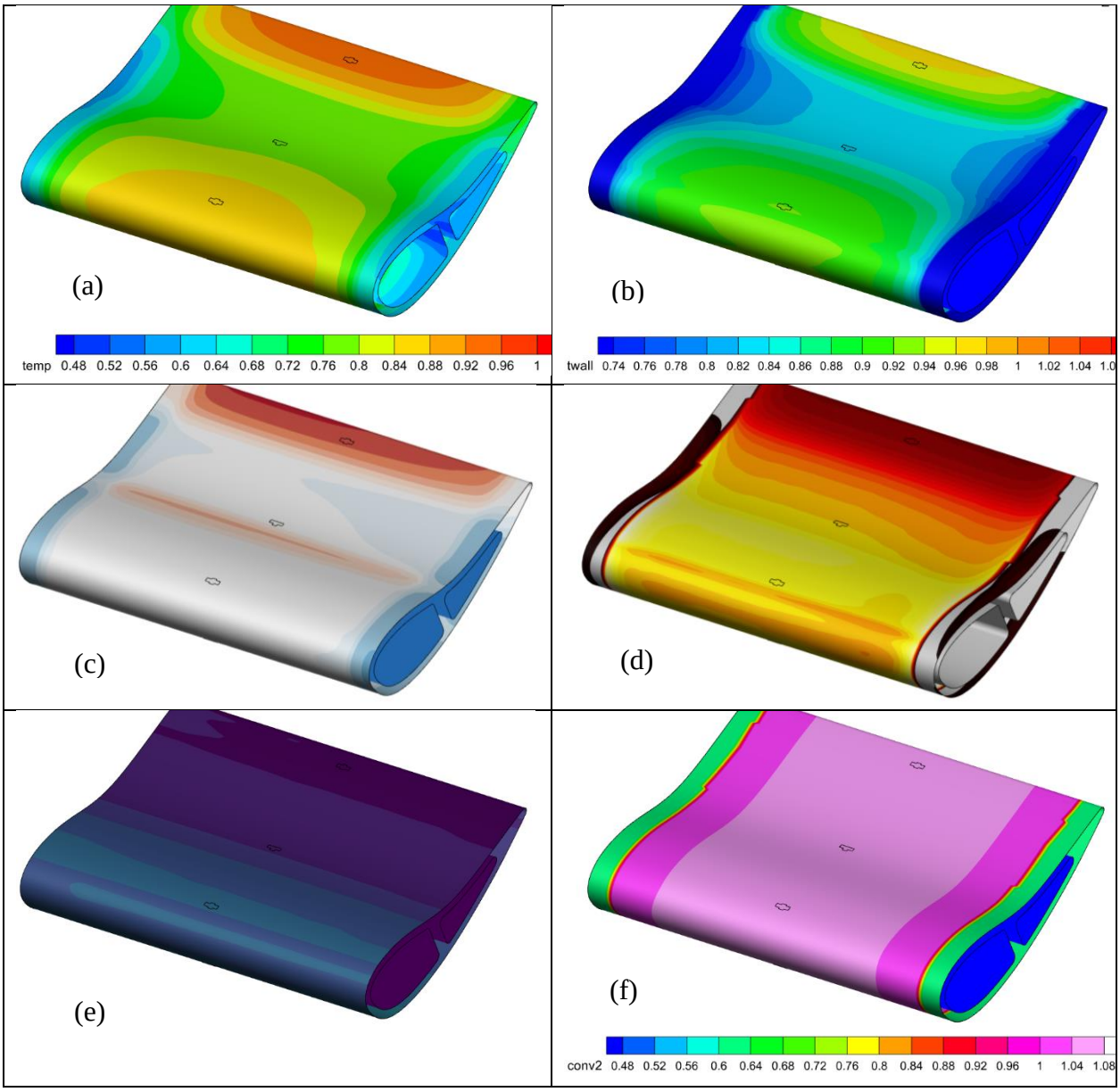

Figure 61. Results of thermal analysis of CMC test article in HPTC rig at the Climb 1A operating condition; (a) CMC/EBC interface temperature, (b) EBC topcoat temperature, (c) temperature difference between inner and outer surface of CMC, (d) wall heat flux, (e) convective heat transfer coefficient, (f) convective hot gas temperature.

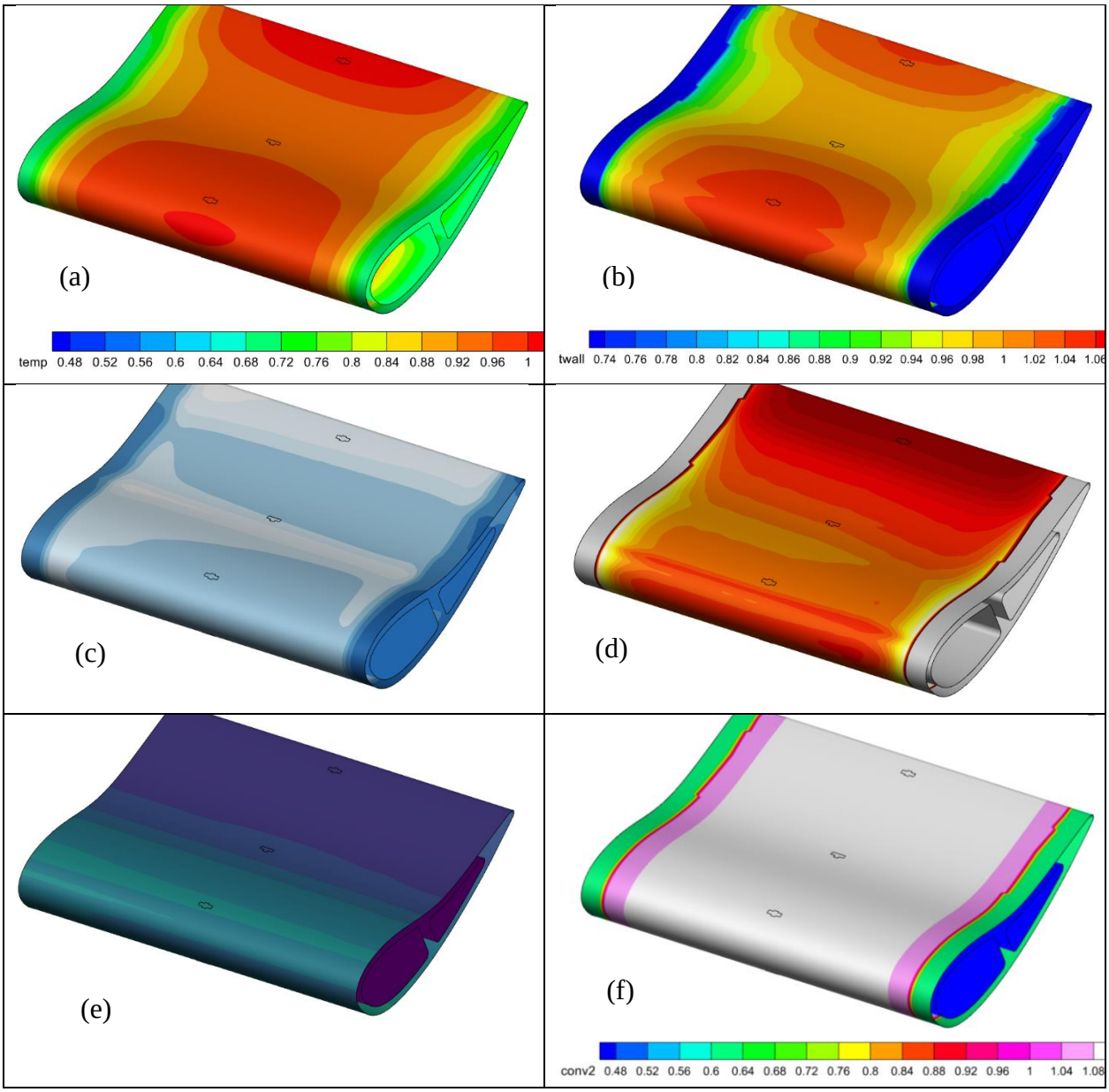

Figure 62. Results of thermal analysis of CMC test article in HPTC rig at the DDP 2B operating condition; (a) CMC/EBC interface temperature, (b) EBC topcoat temperature, (c) temperature difference between inner and outer surface of CMC, (d) wall heat flux, (e) convective heat transfer coefficient, (f) convective hot gas temperature.

The steady-state thermal FEM solution was mapped in ANSYS Workbench for linear elastic thermal-stress analyses in ANSYS Mechanical. The same mesh was used for both thermal and structural analyses, with orthotropic properties applied and locally oriented to bodies of the ply layups and fillers as shown in Figure 57. This FEM used orthotropic properties of the CMC oriented to the ply directions where the x-direction was in the plane of the plies in spanwise (radial) direction across the test section, the y-direction was in the plane of the plies in the around the airfoil and internal cavities (hoop) direction, and the z-direction was normal to the plies through the airfoil wall (interlaminar). The airfoil was elastically supported at the ends where the airfoil was

inserted 0.1” into pockets at rig side walls. The hot gas pressure distribution from the CFD solution was applied to the external airfoil surface and cooling air pressures were applied to the internal cavity surfaces from the internal cooling network model (see Figure 63).

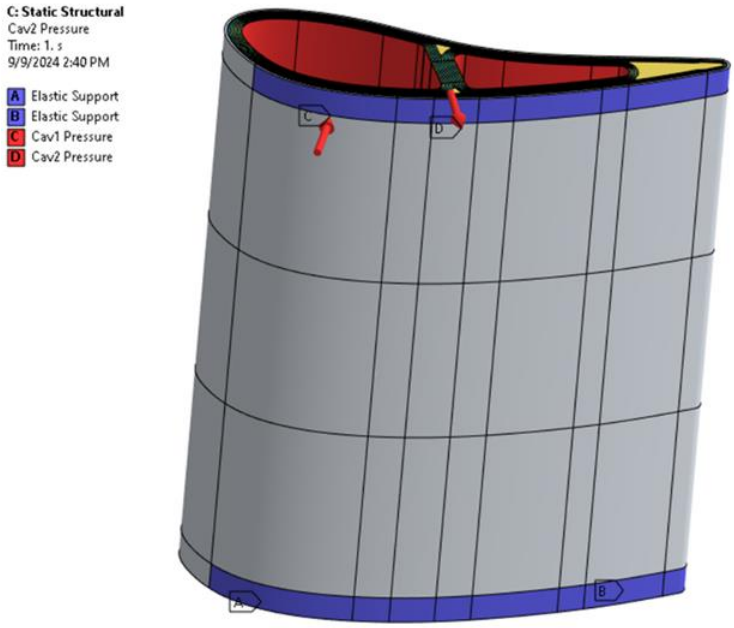

Figure 63. Boundary conditions applied to thermal stress analysis of CMC airfoil.

Results for predicted linear elastic stress in the 3 body-fitted orthotropic directions are shown in Figure 64 for the Climb 1A condition and in Figure 65 for the DDP 2B condition. The stress scales have been non-dimensionalized by their proportional limits (matrix cracking and interlaminar tensile maximum). The Climb 1A condition results in the highest stress states out of all test cases because of its high temperature, heat transfer, and thermal gradient produced by the high temperature combustion gases as well as highest internal convection cooling flow rate. The plot of radial (x-direction) stress indicates that the external CMC plies are in compression while the internal plies are in tension. This is due to the difference in thermal expansion between the hot outer airfoil surface and cooler internal surfaces and rib. Radial tensile thermal stress exceeds the proportional limit in the aft cavity, especially in the relatively cooler rib and hotter trailing edge. Tensile stresses in the radial and hoop directions remain below the ultimate tensile strength throughout most of the vane test article except for localized regions in the rib and trailing edge fillet corners. Our analyses predict significant tensile hoop (y-direction) stress at the internal CMC surface at the vane leading edge. This location has been identified as an area of concern needing more detailed investigation, post-test inspection, and instrumentation.

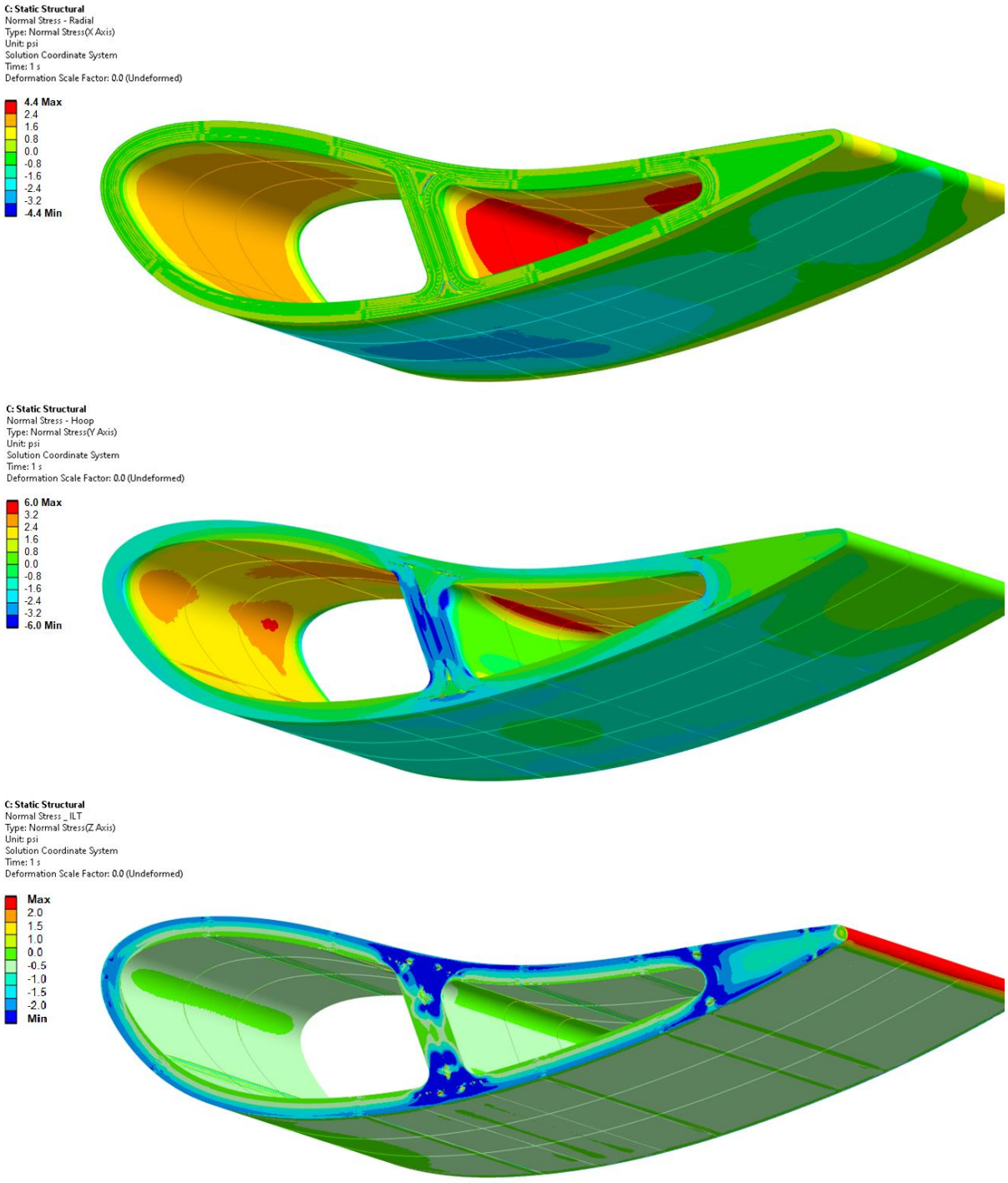

Figure 64. Linear elastic stresses in CMC vane test article in HPTC rig at the Climb 1A operating condition with nominal cooling. Shown are the normal stresses in the locally radial/spanwise (x), hoop (y) and interlaminar (z) directions

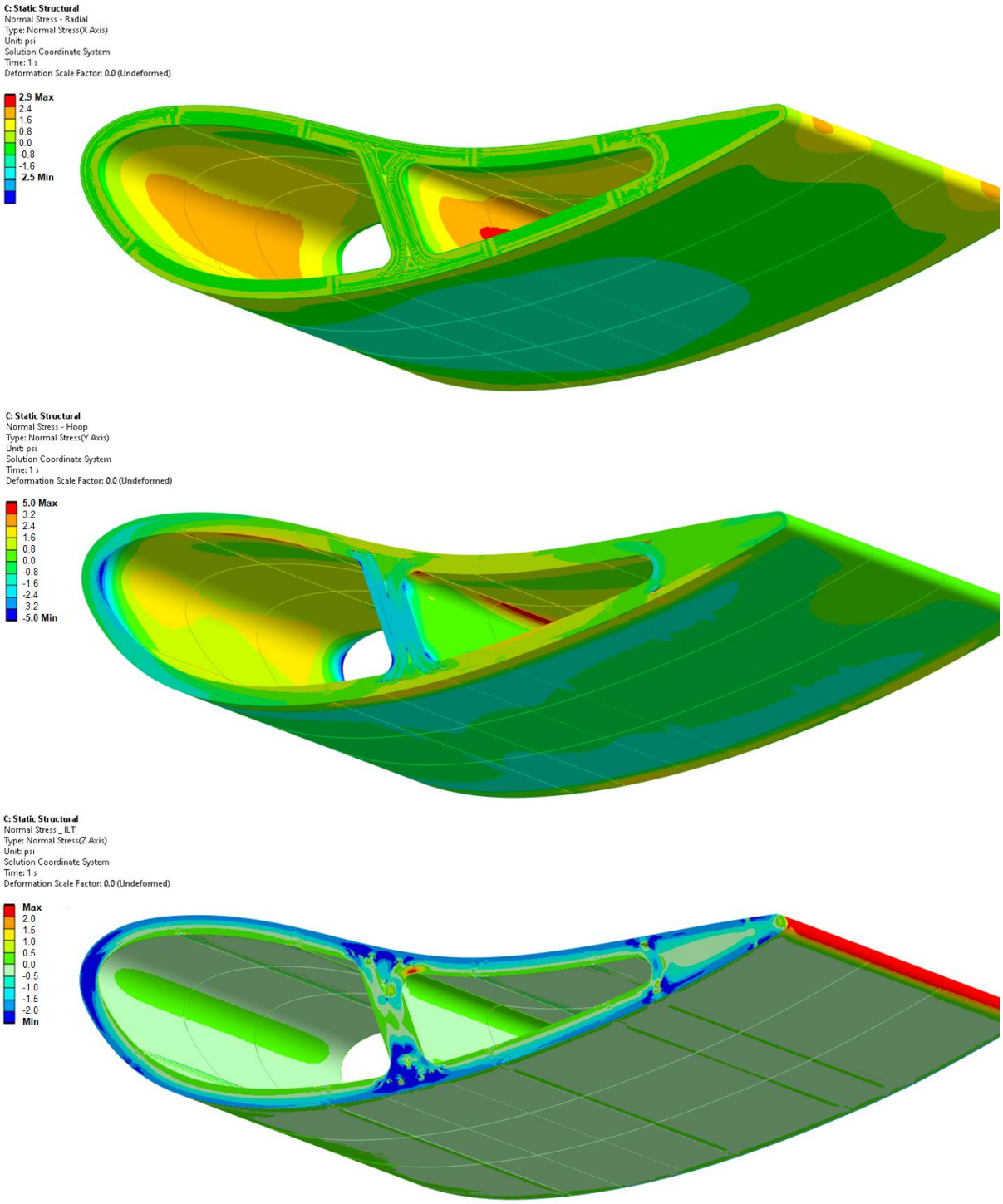

Figure 65. Linear elastic stresses in CMC vane test article in HPTC rig at the DDP 2B operating condition with nominal cooling. Shown are the normal stresses in the locally radial/spanwise (x), hoop (y) and interlaminar (z) directions

Figure 66 shows the hoop stress through the CMC at the vane leading edge, which varies from tensile at the internal surface to the compressive at the external surface. Note that this plot excludes the SiC layers at the inner and outer surfaces. Shown are predictions at the proposed HPTC rig test conditions; Climb 1A, DDP 2B, Cruise 3B, and Takeoff 3B. An additional operating condition, called Lightoff, is shown because shakedown testing in the HPTC rig established that a high fuel equivalence ratio (ϕ_{eqv}>0.7) was necessary to ignite the burner, which results in a high core gas temperature and heat load to the CMC test article, thus requires additional internal cooling to prevent overheating, that ultimately generate thermal stresses that may exceed the ultimate tensile strength in the CMC (see Figure 58) during the brief period before the fuel flow rate and gas temperature can be reduced to the intended test conditions.

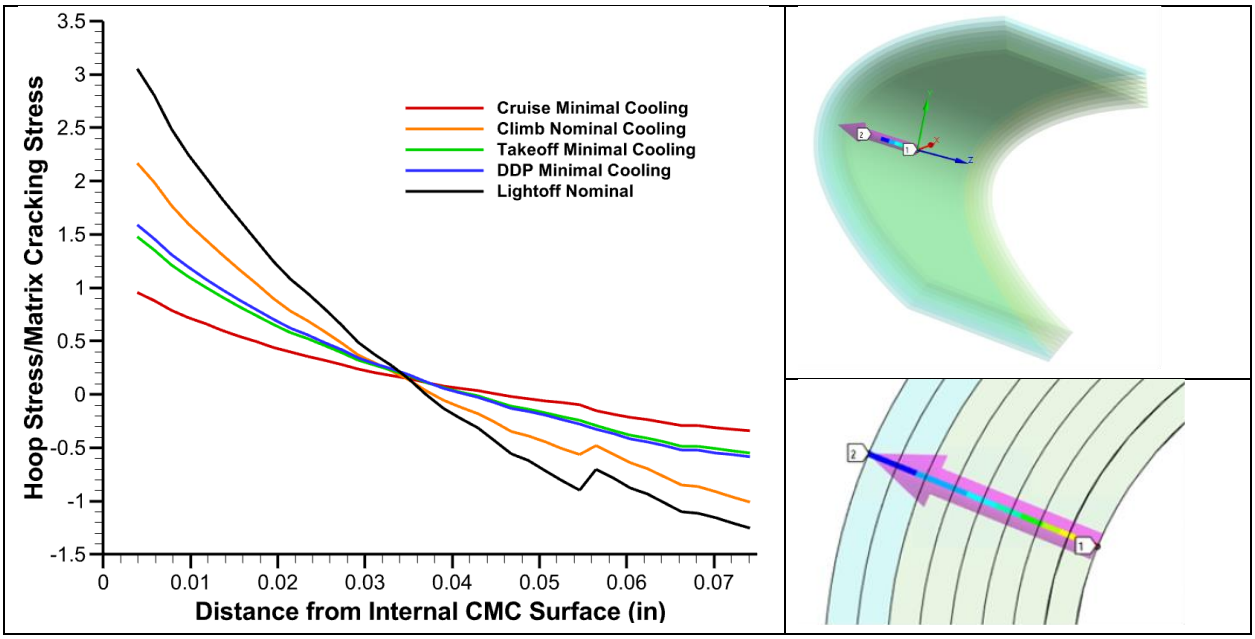

Figure 66. Variation of hoop stress through CMC plies at vane leading edge at test conditions in HPTC rig

Figure 67 is a plot of all pretest predictions of hoop stress versus temperature at the internal midspan leading edge surface (innermost CMC ply). In this figure, hoop stress was normalized by matrix cracking strength and temperature was normalized by maximum CMC temperature (Tmax). The figure provides a comparison between the predicted material responses of the CMC vane test article in the planned tests at the verified by HPTC rig shakedown testing versus responses for a nominally cooling and a minimally cooled CMC 2nd vane in the HyTEC Vision Engine. The blue circles represent results for a nominally cooled CMC 2nd vane at the cruise, climb, takeoff and DDP conditions, where internal cooling flow rate is equivalent to a metallic component. These predictions indicate accelerated damage since the hoop stress is above the matrix cracking limit. The green circles represent results for the CMC 2nd vane at the cruise, climb, takeoff and DDP conditions but with minimal internal cooling. Notice the entire mission of the engine operation is below the matrix cracking limit. The red circles represent results for the test article in the HPTC rig at equivalent cruise, climb, takeoff and DDP conditions as demonstrated by shakedown testing. The planned tests for each of the 3 pairs of CMC vane test articles are labeled with numbers indicating test cases Climb 1A, DDP 2B and thermal cycling between Cruise 3B and Takeoff 3B. The predictions for the material response of the CMC test article in the HPTC

rig at Lightoff is also shown on the plot. Also shown in this figure are lines for the matrix cracking (black) and creep (light blue) limiting stress curves which were derived from coupon testing of the TRL4 CMC material.

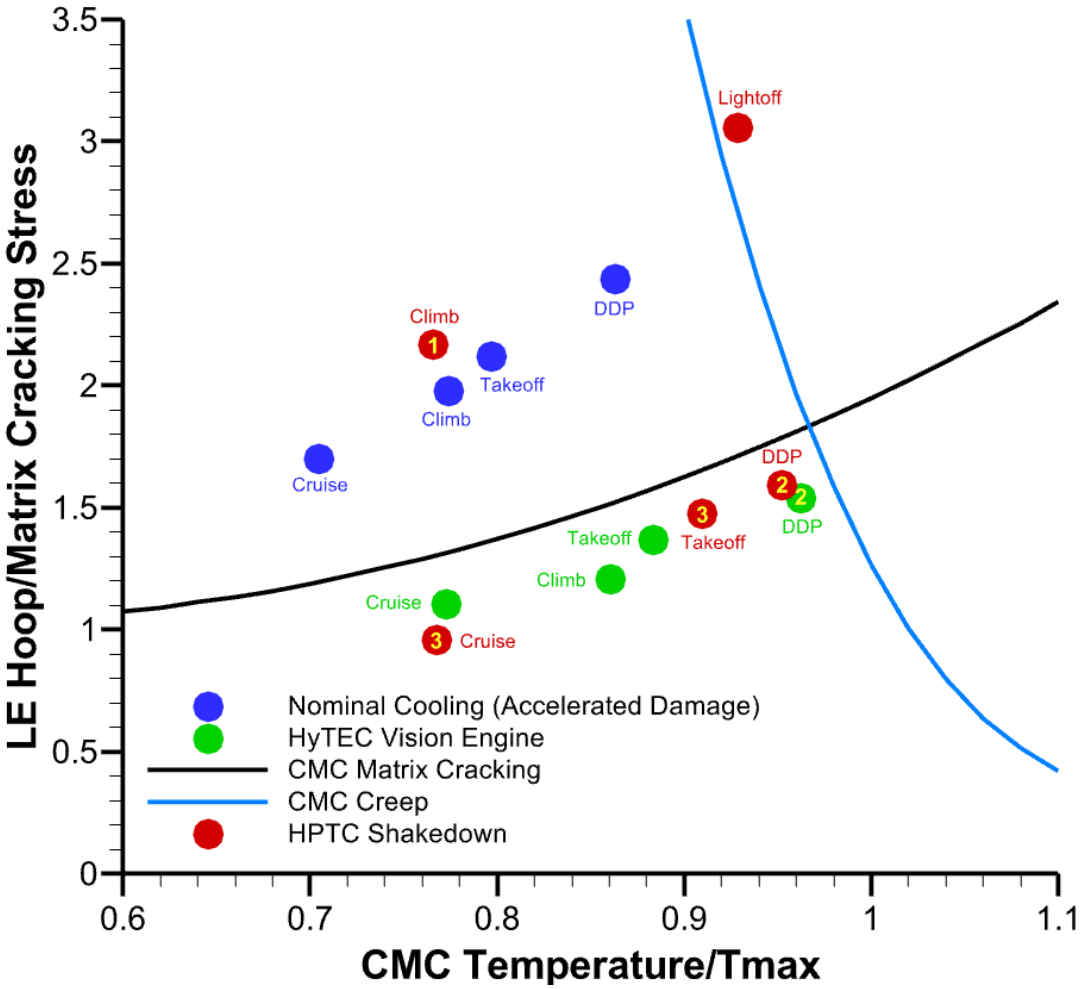

Figure 67. Summary of pretest predictions for hoop stress versus temperature at the internal surface of the CMC vane leading edge. Shown are results for the HyTEC Vision Engine cycle for both nominally cooled and minimally cooled CMC 2nd vanes and the equivalent test points planned for the HPTC rig

Summary of Test Planning and Pre-test Analyses

Pretest thermal and structural analysis of the CMC vane test articles predict the following:

- The highest stresses in the CMC vane test article will be demonstrated during HPTC rig testing at the Climb 1A operating point. Tensile stresses at the internal CMC surfaces generated by the thermal gradient through the airfoil wall and CMC plies are significant enough to cause matrix cracking, delamination, fiber exposure, embrittlement, and degradation due to oxidation. Damage is expected to occur in the innermost CMC plies at the airfoil leading edge, rib fillets, trailing edge. Damage should be localized to these regions and with load transfer to the fibers, the component should avoid abrupt brittle failure.

- We have focused on damage at the vane leading edge where thermal load is great and because delamination can impede heat flow and redistribute temperature, inducing potentially greater interlaminar tensile and shear thermal stress.
- The highest temperatures in the CMC vane test article will be demonstrated during HPTC rig testing at the DDP 2B operating point. The stress in the composite remains just below the proportional and creep limits, thus avoiding significant matrix cracking and maintaining creep resistance. In this operational regime, oxidation of the SiC matrix can lead to crack healing.

Note: The testing portion of this contract was cancelled prior to execution. The following details the proposed testing.

A total six tests will be conducted. All six test articles will be P&W CMC vane sub-elements. Three of them will use P&W's EBC and the remaining three will have NASA's EBC. The first test was to be at accelerated test condition with higher cooling to generate a larger thermal gradient and stress state. The stress states will test resistance against the pesting or active oxidation failure mode observed under intermediate temperatures. The second test was cycling between pesting and creep dominated crack healing condition. Here the effect of crack healing observed in Task 2.1 will be validated. The third test (Test C) will test the vane sub-element under normal HyTEC engine condition with reduced cooling (and thermal gradient). The stress states at these conditions should be lower than the threshold stresses for matrix or fiber damage. The test conditions are illustrated in Figure 68.

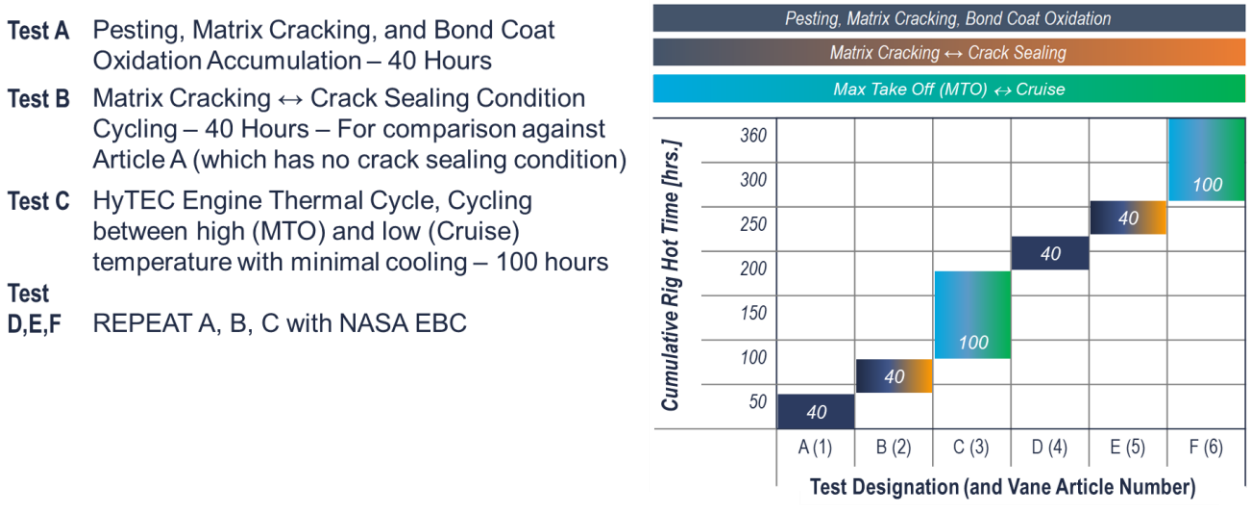

Figure 68. Planned test approach in the HPTC test rig

Instrumentation

A schematic of the air, fuel and water tanks, piping, valves, and instrumentation of the HPTC rig is shown in Figure 69. In this figure, the dark blue lines illustrate the high-pressure room temperature (RT) air that is used to supply the secondary cooling systems. High-pressure and high-temperature air lines from the facility's T-Thermal supply and 80 kW heater are shown in orange. Methane fuel supply lines are shown in red. Cooling water liners are shown in purple (boosted water) and light-blue-green (city water). This figure shows valves, thermocouples (TC), pressure transducers (PT), Coriolis, and venturi flow meters.

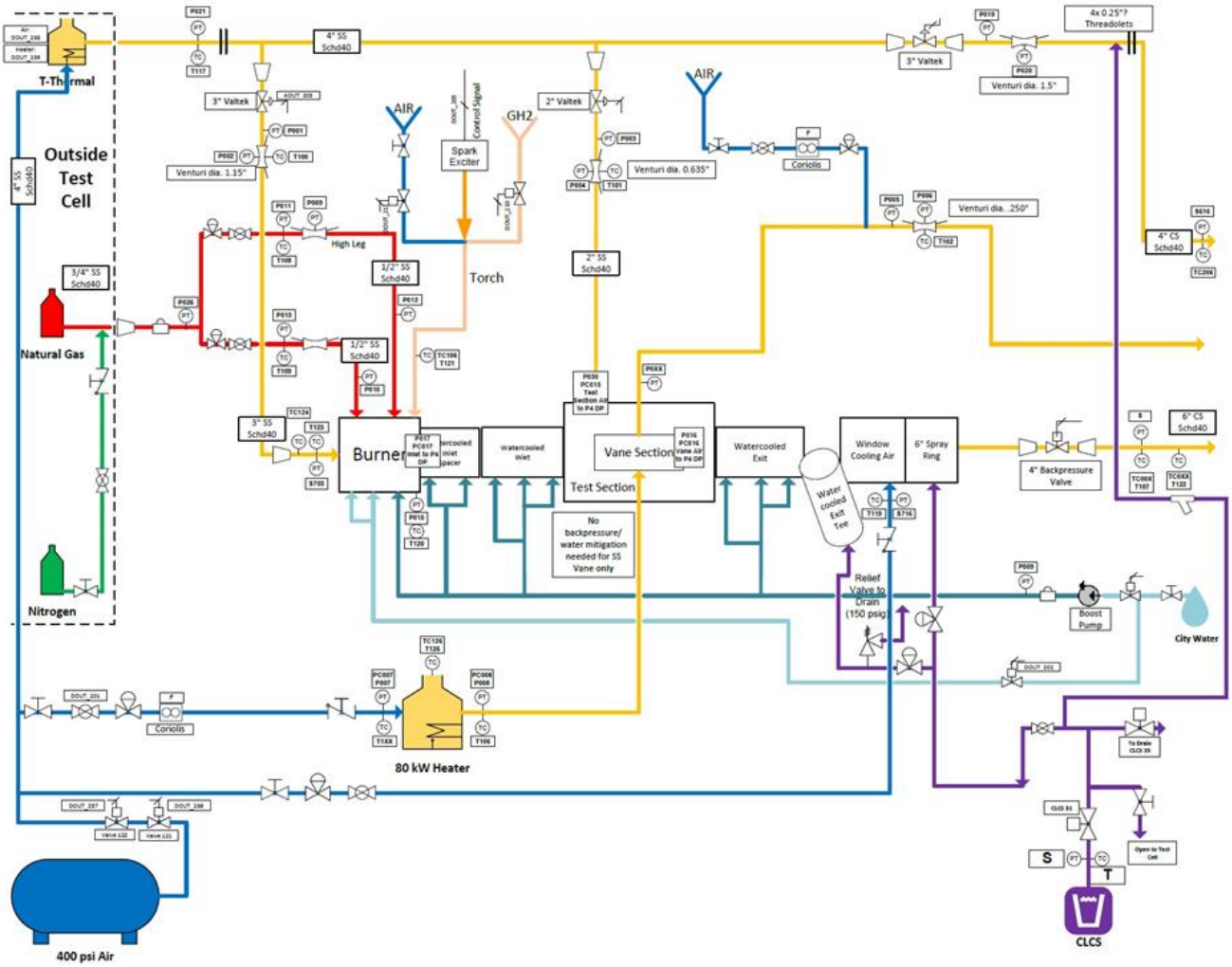

Figure 69. Air, fuel, and water task, piping, valves, and instrumentation of HPTC rig.

Table 30 lists the HPTC rig operating conditions and associated instrumentation identifiers. In this table, T3 is the total temperature and P3 is the total pressure of the compressed and heated air supplied to the burner, which are measured by thermocouple T123 and pressure transducer S703, respectively. The total pressure of the combustion product gases downstream of the burner, P4, is measured by pressure transducer, P015. W3 is the air flow rate delivered to the burner which is derived as W001 determined from measurements of pressures, P001 and P002, and temperature, T100, at the 1.15" venturi meter. The total temperature of the combustion product gases downstream of the burner, T4, was derived from a calculation of adiabatic flame temperature [Gulder, 1986] using fuel equivalence ratio, ϕ_{eqv}=PHI_Overall, P3, and T3. The total pressure at the inlet to the test section, Pgas, and its variation across the profile of the test section, were determined from the CFD model of the core test section given inlet conditions, W3, P4 and T4. Pshroud, Tshroud and Wshroud are the total pressure, total temperature, and flow rate of the cooling air supplied to the test section liner and vane holder. Pshroud is determined by measuring the change in pressure, DP=PC015, from the liner cooling air supply inlet to the test section. Wshroud is derived as W003, which is determined from measurements of pressures, P003 and P004, and temperature, T101, at the 0.635" venturi meter. Pcool, Tcool and Wcool are the total

pressure, total temperature, and air flow rate to the internal cooling system of the CMC vane. Wcool is derived as W007, which is determined from measurements of pressures, P007 and P008, and temperature, T106, from the 80 kW heater that supplies the CMC vane cooling air.

Table 30. HPTC Rig operating conditions and instrumentation.

Operating Condition	Instrumentation Identifier	Description	Units
T3	T123	Burner inlet total temperature	F
P3	S703	Burner inlet total pressure	psia
P4	P015	Burner outlet total pressure	psia
W3	W001	Core test air flow rate from 1.15” venturi meter calculated using P001, P002 and T100.	pps
ϕ_{eqv}	PHI_Overall	From fuel flow meters calculated using P011, P009 and T108 (high) and P013, P010 and T109 (low)	1
T4	N/A	Burner outlet total temperature calculated using T123, S703 and PHI_Overall	F
Pshroud	P015+PC015	Total pressure of cooling air supplied to the test section liner and vane holder	psia
Tshroud	T101	Total temperature of cooling air supplied to the test section liner and vane holder	F
Wshroud	W003	Test section liner air flow rate from 0.635” venturi meter calculated using P003, P004 and T101.	pps
Pcool	P008	Vane cooling supply total pressure	psia
Tcool	T106	Vane cooling supply total temperature	F
Wcool	W007	Vane cooling air flow rate from 80kW heater	pps

The variation of gas temperature across the test section will be measured using a vane-shaped Kiel probe.

Thermocouples (TCs) will be embedded at 3 locations in the CMC wall via a through holes that were laser drilled at an approximate 30° angle relative to the external surface and potted within a high temperature ceramic paste. The intent of these TCs is to measure the SiC-SiC CMC/EBC interface temperature (TEMP). The TCs will be installed such that their hot junctions will be below the exterior surface. The TCs will be installed after the CMC test article is coated with the EBC. The TCs will be positioned adjacent to but outside of the pyrometer focus areas such that the CMC/EBC surface emissivity and consequently the pyrometer reading is not significantly affected by the TCs or ceramic paste. These measurements can be extrapolated to EBC surface (topcoat) temperature having knowledge of the local conditions (through-wall heat flux, location of hot junction within CMC, and coating thickness).

TC measurements will suffer from imprecise knowledge of the true positions of the TC hot junctions and the thermal contact with the CMC. RTRC performed an error analysis for the TC instrumentation and expects that the temperature measurement uncertainty will be +/-25^{o}F. This estimate for TC measurement variation was derived from uncertainties in the locations where the TC is embedded into the CMC wall, quality of contact of the TC with ceramic paste and CMC material, and heat transfer at the TC location. Pretest modeling predicts up to 250^{o}F temperature difference across the CMC wall (between CMC/EBC interface and internal surfaces) and up to 135^{o}F across the EBC (between CMC/EBC interface and topcoat. A more detailed error analysis

will be performed once the TCs are installed into the test article and the true TC hot junction locations and quality of the thermal contacts are determined. This analysis will provide conversions of TC measurements to EBC topcoat temperature, CMC/EBC interface temperature, and internal CMC temperature, with uncertainties derived from measurements of TC hot junction locations, local thicknesses, and thermal contact areas.

Williamson dual wavelength fiber-optic ratio pyrometers (DWF-08-65F-FOV4in/50-A-G06-CF020) will be used to measure the CMC/EBC surface temperature. They have a spectral response of 2 narrow and distinct bands, λ_1=0.8 and λ_2=0.9 um, with an operational range of 1600-3200^{o}F, and field of view of 0.080-in diameter target size at 4-in distance. The temperature range and wavelengths were selected to minimize errors due to transmission through combustion gasses. RTRC will use 4 of these pyrometers during CMC testing in the HPTC rig, with 2 focused on each pressure and suction side of the CMC airfoil, where 3 will be focused on areas adjacent to the TCs described previously. These instruments were selected to compensate for variable emissivity, temperature gradients, optical obstructions, and misalignment.

Dual wavelength pyrometers have an e-slope setting, $E_1E/_2$, which is the ratio of 2 emissivities at the 2 wavelengths, λ_1 and λ_2. Since the condition of the CMC surface is expected to change during the rig testing, the e-slope setting will be different from $E_1E/_2$, which is unknown and varies in time, thus the true temperature of the surface will be different from the pyrometer reading. For example, the true emissivity ratio, $\varepsilon_1\varepsilon/_2$, of an eroded surface may be higher than the pyrometer's e-slope setting that matches the true temperature of a pristine surface, and the pyrometer reading will be higher than the true temperature of the eroded surface. Therefore, e-slope will be set to a base value and the pyrometer temperature readings will be adjusted using Planck's law and the measured $E_1E/_2$ of that surface condition.

RTRC developed a custom experimental procedure to determine the emissivity ratio, $E_1E/_2$, for EBC coated and bare CMC surfaces. RTRC's high-heat flux burner rig was used to heat button-style coupons (1-in diameter 0.100-in thick) with a natural gas and oxygen torch. The back sides of the coupons were cooled with forced air to establish a thermal gradient through CMC and EBC coated coupons. A high emissivity paint (Aremco HiE-Coat 840-CX) was applied to the back (cool, uncoated) sides of the coupons to provide accurate temperature measurements with a Fluke Modline 2-color SWIR pyrometer and a Raytek MI-3 SWIR camera. The temperature of the front (heated, coated) side was measured using an Microepsilon LWIR pyrometer and a FLIR LWIR camera simultaneously with the Williamson dual wavelength pyrometer. The LWIR instruments were selected because the $HfSiO_4$ topcoat has a high stable emissivity (0.9-0.95) in their wavelength range (10-14 um). However, coated side emissivities are likely vary during HPTC rig testing due to sintering, delamination, and coating spallation. Therefore, an iterative procedure was developed to determine emissivity of front side surfaces using coupons at 4 states of deterioration (pristine CMC substrate + bond coat + topcoat, CMC substrate + bond coat with spalled topcoat, bare SiC-SiC CMC substrate, and SiC-SiC CMC oxidized substrate). These coupons were heated on the front side to a measured range of hot side temperatures and cooled on the backside to a measured range of temperature gradients. Thermal gradients were established to assess the effect of transmittance of infrared radiation through the topcoat. Coupons were then removed from the heat source and as they cooled the emissivity settings of the LWIR instruments were adjusted until the heated and cooled side temperature versus time curves converged. This procedure was repeated several times until a reliable value for emissivity was established thus allowing the LWIR instrument to provide a true temperature measurement of the front side +/-10^{o}F. Given true front side temperature, Williamson dual wavelength pyrometer readings at a fixed e-slope setting were recorded for each coupon, front side temperature, and temperature gradient. Data for pyrometer reading versus true temperature with an e-slope setting of 0.976 is shown in Figure 70. Symbols show measurements of the pyrometer reading versus the LWIR camera true temperature for the $HfSiO_4$ topcoat and bond coat coupons. The lines show

predicted transformations from readings to true temperature for various values of the unknown emissivity ratio, $\varepsilon_1/\varepsilon_2$ (true e-slope). The filled circles below the orange line indicate that the e-slope setting of 0.976 is too high for the topcoat, while the open circles above the orange line indicate that it is too low for the bond coat. The e-slope setting of the Williamson pyrometers were iteratively adjusted until the pyrometer reading matched the true temperature. RTRC found an emissivity ratio, E_1/E_2=0.970 for the surface pristine SiC-SiC CMC substrate + bond coat + topcoat and E_1/E_2=1.085 for the surface pristine SiC-SiC CMC substrate + bond coat. Values for e-slope could not be determined for the bare SiC-SiC coupons due to the large and inconsistent drift in the LWIR temperature readings. RTRC is exploring further options to measure emissivity of these surfaces.

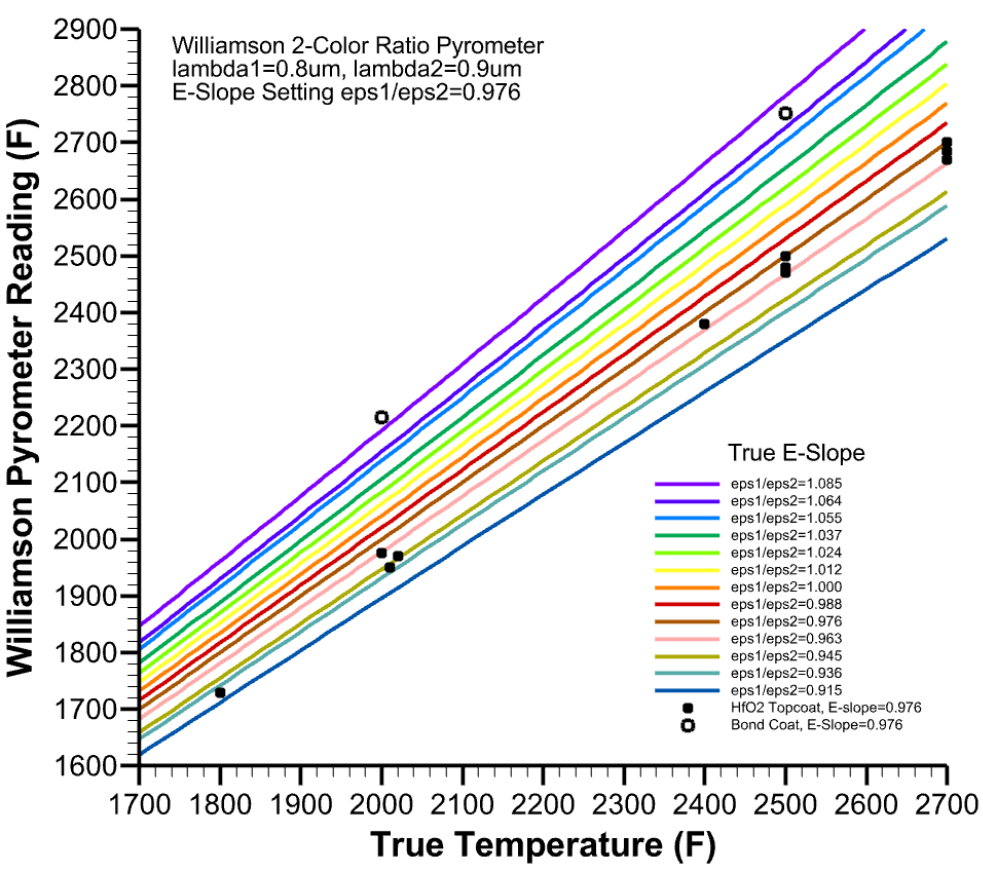

Figure 70. Data from RTRC procedure for measuring CMC and EBC emissivity and e-slope for Williamson dual wavelength pyrometers

The high temperature emissivity and reflectivity in the spectral range 2-20 um was measured on the four coupons by a spectral emissometer at Advanced Fuels Research. A selection of the recorded data is shown in Figure 71:

1. Sample 10-3 as-received SiC/SiC CMC
2. Sample 20-1 SiC/SiC CMC oxidized for 100-hr in air at 2500°F
3. Sample 30-3 Sintered bond coat on SiC/SiC CMC
4. Sample 40-3 $HfSiO_4$ topcoat on bond coat on SiC/SiC CMC.

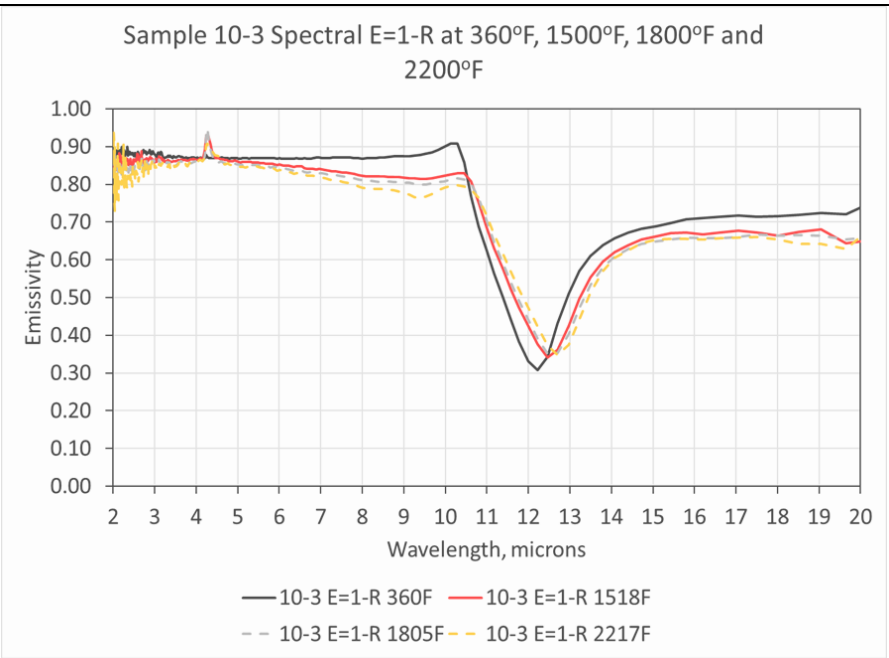
Sample 10-3 Spectral E=1-R at 360°F, 1500°F, 1800°F and 2200°F
Emissivity
1.00
0.90
0.80
0.70
0.60
0.50
0.40
0.30
0.20
0.10
0.00
2 3 4 5 6 7 8 9 10 11 12 13 14 15 16 17 18 19 20
Wavelength, microns
10-3 E=1-R 360F
10-3 E=1-R 1518F
10-3 E=1-R 1805F
10-3 E=1-R 2217F

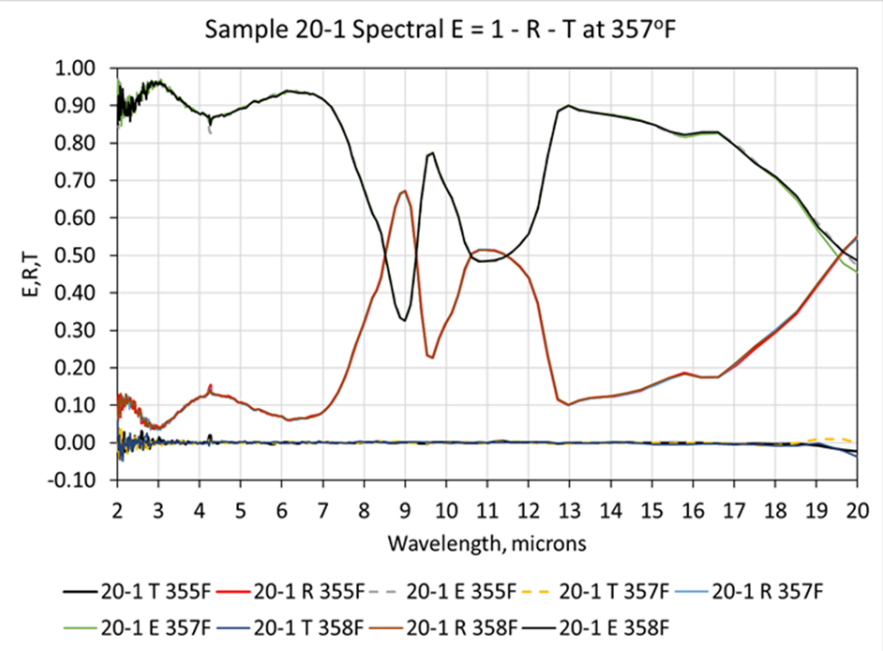
Sample 20-1 Spectral E = 1 - R - T at 357°F
E,R,T
1.00
0.90
0.80
0.70
0.60
0.50
0.40
0.30
0.20
0.10
0.00
-0.10
2 3 4 5 6 7 8 9 10 11 12 13 14 15 16 17 18 19 20
Wavelength, microns
20-1 T 355F
20-1 R 355F
20-1 E 355F
20-1 T 357F
20-1 R 357F
20-1 E 357F
20-1 T 358F
20-1 R 358F
20-1 E 358F

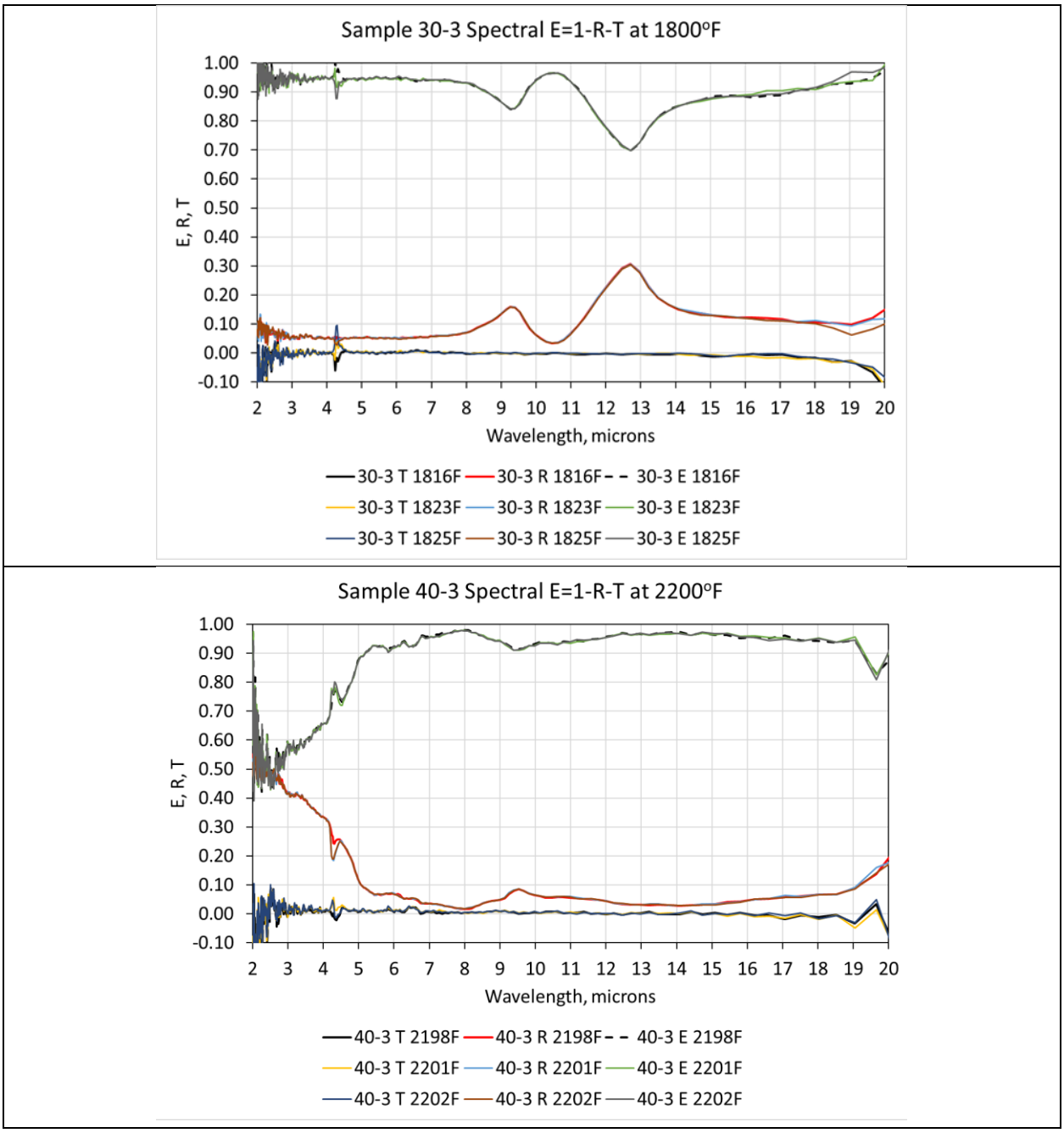

Figure 71. Spectral emittance, E, reflectance, R, and transmittance, T, of bare and coated CMC coupons measured by a spectral emissometer in 2-20 μm optical range.

It is understood that the spectral emittance data provided in Figure 106 is outside the spectral range of the dual wavelength pyrometers (0.8/0.9 μm) that are used in the HPTC rig. Measurements below 2 μm are needed for emittance, reflectance and transmittance at 0.8 and 0.9 μm. RTRC attempted to measure the emissivity of the same coupons in the 0.5-1.0 mm optical range using the FMP2 spectral pyrometer provided by FAR Associates. The emissivity data, however, was inconclusive.

Furthermore, none of the coated samples (Samples 30-3 and 40-3) are freestanding, which means that transmittance of the bond coat and EBC topcoat were not measured. Specifically, for the EBC coated coupon (Sample 40-3 in Figure 106), reflectance increases as wavelength decreases in the shorter wavelengths and is 0.5 at 2 μm. It is possible that the reflectance of the EBC may continue to increase below 2 μm, and following the trend, reflectance can be 0.6 in the 0.8/0.9 μm range. In addition, the EBC topcoat may have some unknown amount of transmittance. Combining reflectance and transmittance, the emittance of the topcoat can be very low, perhaps 0.3. The concern here is that the dual wavelength pyrometers would be reading primarily reflected radiation plus some radiation transmitted through the EBC.

The sources of reflected radiation include emissions from the air-cooled and water-cooled rig side walls and the hot combustion product gas in the test section. During HPTC testing, the EBC surface temperature runs at 2550°F (see Figure 97b) while the air-cooled rig side walls are on average 1300°F and the water-cooled rig side walls are on average 750°F. Using Planck's law, blackbody radiation intensity in the optical range 0.8/0.9 μm from a 2550°F surface is 400-900x larger than a surface at 1300°F, and 10^6x larger than a surface at 750°F. RTRC quantified the effect of reflection of thermal radiation within the HPTC rig test section and its expected influence on the pyrometer readings. For this analysis, the model considered the water-cooled and air-cooled side walls at their highest temperature. These walls are coated with air plasma sprayed (APS) 7% yttria-stabilized zirconia (7YSZ) thermal barrier coating (TBC) that have a low emissivity. The ray-based model considered the emissivity of the TBC and the reflectivity of the EBC with combined spectral radiances. We predicted that the radiation emitted by the side walls and reflected by the EBC topcoat will have a very small effect on the dual wavelength pyrometer readings. The ray-based model predicted that the worst-case uncertainty in the temperature measurement would be about 2°F cooler. The combustion product gases in the test section, however, will be as high as 2900°F and can be a significant source of reflected thermal radiation and error in the temperature measurement of the dual wavelength pyrometers.

Using Wien's radiation equation,

$$I_{r,\lambda} = E_{r,\lambda} I_{r,b,\lambda} = E_{r,\lambda} C_1 \lambda^{-5} \exp\left(-C_2/\lambda T\right)$$

the 2-color measurement of temperature, T, of a graybody surface is

$$T = \frac{C_2\left(\frac{1}{\lambda_2} - \frac{1}{\lambda_1}\right)}{\ln\left|\frac{I_{r,\lambda,1}}{I_{r,\lambda,2}}\right| - \ln\left|\frac{\mathrm{E}_{r,1}}{\mathrm{E}_{r,2}}\right| + 5\ln\left|\frac{\lambda_1}{\lambda_2}\right|}$$

Here, $I_{r,\lambda,1}$ and $I_{r,\lambda,2}$ are the measured intensities of thermal radiation at wavelengths λ_1 and λ_2, and $\mathrm{E}_{r,1} = \mathrm{E}_r(\lambda_1)$ and $\mathrm{E}_{r,2} = \mathrm{E}_r(\lambda_2)$ are the emissivities, C_1=1.19104×10^{-16} kg*m^4/s^3, C_2=0.014388 m*K. Consider a surface that is both emitting and reflecting thermal radiation which is transmitted through an absorbing medium with wavelength-dependent absorptivity. According to the Beer-Lambert law, the intensity ratio of an emitting and reflecting graybody is

$$\frac{I_{r,\lambda,1}}{I_{r,\lambda,2}} = \frac{\left(\mathrm{E}_{r,1} I_{b,\lambda,1} + \mathrm{P}_{r,\lambda,1} \sum_j \mathrm{E}_{r,j,1} I_{b,j,\lambda,1}\right) \exp\left(-\alpha_{r,1} L\right)}{\left(\mathrm{E}_{r,2} I_{b,\lambda,1} + \mathrm{P}_{r,\lambda,2} \sum_j \mathrm{E}_{r,j,2} I_{b,j,\lambda,2}\right) \exp\left(-\alpha_{r,1} L\right)}$$

Here, $\alpha_{r,1}=\alpha_r(\lambda_1)$ is the absorption coefficient at λ_1, $\alpha_{r,2}=\alpha_r(\lambda_2)$ is the absorption coefficient at λ_2, L is the length of the absorbing medium. $\mathrm{E}_{r,\lambda}$ is emissivity, $\mathrm{P}_{r,\lambda} \geq 1-\mathrm{E}_{r,\lambda}$ is reflectivity, and $I_{b,\lambda}$ is blackbody intensity of the measured surface at wavelength λ. $\mathrm{E}_{r,j,\lambda}$ is the emissivity and $I_{b,j,\lambda}$ is the blackbody intensity of the jth reflected graybody radiation at wavelength λ.

RTRC used the software application RADCAL, a narrow-band model for quantifying thermal radiation transmission through a combustion environment (nist.gov), to study the emissivity and absorptivity of the natural gas combustion product gases in the wavelength band (λ_1=0.8um to λ_2=0.9um) at the HyTEC operating conditions in the HPTC rig. This analysis assumed combustion product mole fractions of methane combustion in air, x_{CH4}=0.010, x_{CO2}=0.076, x_{H2O}=0.102, x_{O2}=0.072, and x_{N2}=0.740, and a small soot volume fraction, 1e-7, for gases at 1750K. RADCAL predicted constant total gas emissivity and absorptivity, $\mathrm{E}_1=\mathrm{E}_2=\mathrm{A}_1=\mathrm{A}_2$=0.03 over a L=3-in beam length, and a variation of gas transmissivity from $\mathrm{T}_1=\exp(-\alpha_1 L)$=0.9358 at λ_1=0.8μm to $\mathrm{T}_2=\exp(\alpha_2 L)$=0.9426 at λ_2=0.9μm.

Wien's formula was used to predict thermal radiation intensity ratio for the true CMC surface temperature, T, given gas absorption coefficients, α_1 and α_2.

$$\frac{I_{r,\lambda,1}}{I_{r,\lambda,2}} = \frac{\mathrm{E}_{r,1}}{\mathrm{E}_{r,2}} \left(\frac{\lambda_1}{\lambda_2}\right)^{-5} \exp\left(\frac{C_2}{T}\left(\frac{1}{\lambda_2}-\frac{1}{\lambda_1}\right)+\left(\alpha_{r,2}-\alpha_{r,1}\right)L\right)$$

This analysis predicts that gas absorption along the optical path will have a negligible effect on the pyrometer reading.

A similar exercise was done to determine the amount of thermal radiation generated by the hot gas and reflected by the EBC topcoat. For the hottest test case in the HPTC rig (DDP) with a gas temperature of 2900°F, a constant gas emissivity of 0.03, and topcoat temperature of 2550°F and reflectance of 0.6 in the 0.8/0.9 μm spectral range, the reflected hot gas radiation would account for about 25% of the thermal radiation intensity to the dual wavelength pyrometer. Accounting for all sources of reflection for the hottest test condition, the dual wavelength pyrometer will read up to 50°F hotter than the true EBC topcoat temperature.

Given that the temperature measurement of a dual wavelength pyrometer is determined by the ratio of 2 radiation intensities, the most concerning source of error in the EBC surface temperature measurement is the ratio of the emissivities, $\mathrm{E}_1\mathrm{E}/_2$, at the pyrometer wavelengths λ_1 and λ_2. Reflection of the hot combustion product gas radiation by the EBC topcoat surface is significant and is the 2nd largest source of error. The 3rd largest source of error is the transmittance of radiation from the bond coat through the $HfSiO_4$ topcoat.

Since we have measurements of only emittance and reflectance, not transmittance, RTRC derived a method for determining $\mathrm{E}_1\mathrm{E}/_2$ using only the optically opaque coupons. We understand that the EBC topcoat can transmit thermal radiation especially in the short and mid-wave ranges and this effect remains a source of error in our optically based measurement. Pretest modeling of the CMC vane during HPTC rig testing predicts thermal gradients within the EBC (bond coat + topcoat) during HPTC rig testing. The transmissive layer, the topcoat, is approximately ¼ of the thickness of the EBC and is assumed to have a transmissivity of 0.05-0.25, and the remaining bond coat likely has a transmissivity less than 0.05. Therefore, due to transmittance of the radiation from the CMC and bond coat substrate through the EBC topcoat, the pyrometer

measurement of the topcoat surface will be lower than the true temperature by at most 10°F. The procedure for measuring emissivity of the opaque coupons under different thermal gradients supports this estimate of measurement uncertainty.

Furthermore, RTRC performed experiments and analysis to determine the effect of the quartz windows on the dual wavelength pyrometers over a range of angles of incidence. Here, blackbody painted SiC coupons were heated to HPTC rig temperatures. The pyrometers focused on the coupons through a quartz window, both normal to and at different angles of incidence up to 45°, which is greater than the incidence angles of the pyrometers' focal lines upon the CMC vane in the HPTC rig (see Figure 53). Results indicated that quartz windows had a negligible effect on the pyrometer readings.

Summarizing everything in this section, RTRC has chosen to use dual infrared pyrometers in the 0.8/0.9 μm spectral range for continuous online measurements of the CMC test article during HPTC rig testing. These pyrometers were selected due to their low cost, easy implementation, and high transmissivity through quartz windows. Due to the expected error and drift observed in the pyrometer temperature measurements in prior HPTC rig tests, the initial intent was that the test articles were to be coated only with the optically opaque TBC bond coat but not include the highly reflective EBC topcoat. Later, RTRC and P&W decided to run the CMC test articles with the topcoat and use the optical testing and analysis to correct the temperature readings. In future work, RTRC has recommending using LWIR pyrometers or cameras. Those measurement systems will require specially designed and cooled optical ports, windows and lenses with high transmissivity in the LWIR spectral range such as ZnSe and including nonreflective coatings.

3.3.3 Manufacturing Plan and Test Execution

P&W manufactured six (6) CMC vane sub-elements for testing under Task 2.3. The Task 2.3 vane sub-elements followed same CMC manufacturing steps as coupons for Task 2.1 and 2.2. Vane sub-elements were inspected at P&W CMC Center of Excellence (COE) by xCT, blue light and thermography to check uniformity and density. Based on results from Task 2.2 EBC durability testing, the decision was made to use P&W EBC on half of the vanes and NASA EBC on the other half. The contract was modified accordingly, and CMC vanes were sent to NASA for EBC coating.

Turning Vane sub-element fabrication followed standard P&W processes that have been refined over multiple years of internal CMC technology development. The majority of the processes were performed in-house, with the exception of fiber manufacturing, weaving and preforming. Fibers and preforms were sourced from vendors the P&W CMC team has extensive experience with, including a Joint Technology Development Agreement, allowing P&W to leverage learning across various programs for HyTEC turning vane sub-element fabrication.

Vanes were delivered to RTRC for bondcoating in an automated bondcoat slurry spray system. The vanes were bondcoated one at a time, followed by whitelight inspection to determine how well the bondcoat thickness met tolerance. In general, results were acceptable, with room for improvement. Adjustments were made to the bondcoat process to improve the thickness distribution after each inspection. A similar approach was used to apply the topcoat by air plasma spraying. Vanes were coated then inspected by whitelight. Rework was required for two of the four 4 vanes due to variation in the bondcoat process that led to poor adhesion. Rework was successful for both vanes. These vanes were then scanned using xCT to capture pre-test scans for comparison to future post-test scans. Three coated vanes were delivered to RTRC for instrumentation prior to testing in the HPTC rig.

The test plan for CMC vanes in the HPTC rig was not executed.

3.3.4 Results and Discussion

The engine conditions at the normal operation and accelerated conditions are analyzed and the corresponding test conditions at the HPTC rig are established. The accelerated test conditions (Tests A and B) are determined such that the failure modes of interest (cracking at pesting condition and crack healing at creep conditions) are generated and compared with observation in Task 2.1 coupon testing. This achieves one of the three objectives of test campaign, namely failure mode initiation and validation. The test condition C will validate all the three primary objectives of the HyTEC objectives: 400F higher temperature capability, 2.5% less cooling, stresses below the threshold for damage indicating possibility of achieving the targeted lifetime of the engine. Based on pre-test analysis, while not validated by HPTC rig testing, we would expect to meet the success criteria established representative of a commercial engine cycle.

4 CONCLUSIONS

4.1 SUMMARY

During the course of the HyTEC High Temperature CMC Vanes contract, P&W gained significant learning regarding both CMC and EBC material systems which will help guide the company's TRL progression. CMC material degradation and crack healing mechanisms were confirmed during testing under commercial engine cycles conditions. EBC durability testing highlighted a key limitation in the current P&W EBC system at HyTEC vision engine test conditions which instigated a root cause investigation and drove a change to the existing EBC material development plan. While pre-test vane analysis was unable to be validated with rig testing, expected vane component performance falls within program success criteria. Pre-test analysis demonstrates a minimal durability equivalent to current SOA with an un-cooled CMC vane.

4.2 PERFORMANCE TO TPMS

High temperature CMC vane technology is directly relevant to the HyTEC program goals through increased thermal efficiency. The increased temperature capability enables higher turbine inlet temperatures, which can deliver the same thrust or power at smaller core sizes, or a higher power density core. Additionally, increased turbine inlet temperatures and smaller core sizes lead to fuel burn benefits as compared to current State of the Art (SOA).

The HyTEC Vision propulsion system is based on the PW1500G/A220 with several technology concepts which includes coupled low fan pressure ratio with a short inlet, planetary fan drive gear system, ultra-light weight composite fan blade with larger diameter and integrated lightweight structures and mounts, new fan containment system, low-noise propulsor fan and exit guide vanes, smaller core, higher overall pressure ratio (OPR) with a 5 stage low pressure compressor (LPC) and 9 stage high pressure compressor (HPC) with coatings and rub systems for higher temperature capability, ultra-low emission combustor with a novel configuration for reduced pattern factor and low noise swirler, high-temperature advanced CMCs and coatings in the high pressure turbine (HPTC), modified work split with a low rim speed, and a 4 stage higher speed low pressure turbine (LPT) with a steep duct and high aspect ratio turbine exhaust case (TEC). The thrust and takeoff requirements were the same as the PW1500G. Various engine configurations and operating conditions were studied to find the optimal Vision Engine configuration.

TPM's are measured for the current P&W CMC / EBC material system (2500°F CMC) from the testing in the HyTEC work scope. In future studies, TPM's will also be calculated for the next generation CMC / EBC material system (2700°F CMC), which will be required by the HyTEC Vision Engine system to meet the program goals. The durability testing and understanding of failure mechanisms will translate directly between the two generations of material systems as the improvement in material capabilities is the major technical gap to maturing the next generation's capabilities. NPSS was used in all engine cycle analyses. The testing, mission analysis and lifing predictions could be repeated in the future for the next generation material system. The specific TPM's are outlined below, and are captured in tabular form in Table 31, including full and minimum success criteria for the high temperature CMC vane technology. It is understood that the benefits of the technology will be evaluated against each metric to ensure compatibility as an overall system in the Vision Engine Model.

Table 31. HyTEC KPPs and Related TPMs addressed during P&W CMC contract

Key Performance Parameters			Technical Performance Measures		
KPPs	**Full Success Single Aisle ~2035 EIS**	**Min. Success Single Aisle ~2035 EIS**	**TPMs**	**Full Success Single Aisle ~2035 EIS**	**Min. Success Single Aisle ~2035 EIS**
KPP1 Fuel burn reduction attributed to high-power density-core of the original equipment manufacturer's vision turbofan engine	10%	5%	1) Turbine Cooling Air Reduction	-2.5% W25	-2.0% W25
KPP3 Engine Overall Pressure Ratio (defined at top of climb)	>50	>45	2) T3 Capability	T3 Required by Vision Engine Model	T3 Required by SOA baseline
KPP4 Durability, measured in operating hours between major refurbishment	Exceed SOA by 5%	Meet SOA	3) Max use Temperature at SOA Life	Exceed SOA Life by 5%	Meet SOA Life
			4) Predicted Vane Trailing Edge Life	Exceed SOA Life by 5%	Meet SOA Life

Turbine Cooling Air Reduction

The first TPM is a calculation of the reduction in turbine cooling air (TCA) required to meet the state of the art (SOA) baseline life requirements enabled by the high temperature CMC vane technology. This TPM was determined by evaluating the SOA baseline cycle and mission to determine the time and temperature requirements for two key flight conditions: max takeoff (MTO) and cruise. Based on these temperature and time buckets, the CMC and EBC material capabilities evaluated in Task 2.1 and 2.2 were used to calculate the amount of turbine cooling air that is required to meet the overall mission requirements. In summary, TCA was reduced from 31.6% to 22% of the engine core air flow (W25). Most of the TCA reduction was due to the introduction of 2500°F capable CMC static components, specifically, 1st and 2nd turbine vanes and 1st blade outer air seal (BOAS). The reduction of TCA and resulting high core flow rate provided for a 150°F reduction of the turbine inlet temperature (T4) to the target LPT temperature (T45) for an uncooled low turbine while providing the same thrust at MTO and cruise.

The optimal configuration resulted a 6% reduction in fuel burn derived from a 6% increase in engine thermal efficiency. This improvement met the minimum success criterion but fell short of the full metric due to the requirement of an uncooled low turbine. The core size was reduced which increased the fan bypass ratio but the additional weight and drag of the larger fan counteracted some of the TSFC improvements and resulted in some component efficiency penalties. Higher thermal efficiencies and further fuel burn reductions might be achieved by increased temperature (T3, T4 and T45) but with accompanying cooling of the LPT. Note that NPSS predicts thrust specific fuel consumption (TSFC) not fuel burn. Normally fuel burn is determined from a weighted sum of missions, instead trade factors were used since that information was not available.

Increased Overall Pressure Ratio and T3 Capability

KPP #3 is the target increase in engine overall pressure ratio (OPR). TPM #2 is the ability of the high temperature CMC vanes to support the higher compressor exit temperatures (T3). KPP #3 was met by increasing OPR from baseline to 114% baseline at max takeoff (MTO). The work split was modified so that this increase in OPR was accomplished solely by a 5 stage LPC with

water injection and smaller core. This change allowed for an increase in the HPTC efficiency from 89% to 91% and a 20°F decrease in T3.

In our cycle study, T3 and T45 were set to MTO values, and T4 and OPR were calculated. These conditions enabled an uncooled low turbine with 2500°F capable static CMC components. The CMC material capabilities were measured directly from the testing of the current P&W CMC / EBC material system.

Predicted Vane Life Improvement

TPM #3 is the predicted life improvement of a high temperature CMC vane over the state of the art (SOA) metal baseline. There is no established model to predict life below the damage threshold and it is not practical to rig test a CMC vane for the number of hours required to establish vane life under HyTEC vision engine conditions. Task 2.1 has established a guideline on damage threshold for CMCs. From the Task 2.3 model calculations shown earlier in section 3.3.2, a P&W high temperature CMC vane would exhibit stresses below the CMC damage threshold under HyTEC operating conditions without the need for cooling air. The intent of the proposed test plan for Task 2.3 was to test both above and below the damage threshold. This would allow us to verify the model based on current CMC vane design and material properties. Unfortunately, since the proposed testing was not performed under this contract, we can only state that given no operating degradation mechanism, the P&W CMC vane would meet, if not exceed, expected life a baseline metal vane. However, the EBC would be expected to show degradation at the CMC vane operating conditions proposed in Task 2.3, as was demonstrated by the coupon learning from Task 2.2, and would therefore not meet the target SOA lifetime.

Learning gained during the course of this contract will influence the direction of internally funded material development efforts. The next generation of 2700F capable P&W EBC/CMC will meet the TRL5/6 metric and address the limitations documented in this report. This generation of material will achieve the durability requirements necessary to extend operating hours between major refurbishment for EBC coated CMC vanes (KPP4).

Predicted Vane Trailing Edge Life

The argument presented earlier under the predicted vane life improvement also holds true for the predicted life and validation of the P&W CMC vane trailing edge design. Based on analysis performed for Task 2.3, CMC stress in the vane trailing edge was predicted to be below the material damage threshold.

Predictions of expected P&W vision engine performance, including CMC vane technology, are shown in Table 32.

Table 32. Predicted performance of P&W Vision Engine

KPP#	Key Performance Parameter (KPP)	Full Success Single Aisle ~2035 EIS	P&W Vision Engine	Min. Success Single Aisle ~2035 EIS
KPP-1	Fuel burn reduction attributed to the high power density core of the original equipment manufacturer's (OEM) vision turbofan engine	10%	6%	5%
KPP-3	Engine Overall Pressure Ratio	>50	56	>45
KPP-4	Durability, measured in operating hours between major refurbishment	Exceed SOA by 5%	TBD	Meet SOA baseline

4.3 EVALUATION OF TRL

High Temperature CMC Vane Technology is a key technology investment that P&W has fully committed to for next generation engines. To fast-track this enabling technology, accelerated durability testing is required to ensure that this new material capability will be able to achieve the component life requirements necessary for next generation single-aisle propulsion systems. P&W has outlined a path to establish testing to accelerate this durability learning, and ultimately deliver this technology into the next generation single-aisle product as outlined in Table 33. During the course of this contract, when combined with internal research and development efforts, we have advanced our CMC learning through TRL4. Since we were unable to conduct required TRL5 component rig testing, TRL5 readiness will be achieved through future internal program funding.

Table 33. P&W CMC Technology Progression Plan

	Readiness Criteria / Requirements	**Validation Strategy / Methodology**	**Status**
TRL 4	*Component validation in lab environment*		
	• Initial CMC Durability Testing	• Coupon Testing	• Complete – internal testing for military application
	• Initial EBC Durability Testing	• Coupon Testing	• Complete – internal testing for military application
		• Rig Testing - RTRC Gradient Burner Rig	• Complete – internal testing for military application
	Readiness Criteria / Requirements	**Validation Strategy / Methodology**	**Status**
TRL 5	*Component validation in relevant environment*		
	• CMC Durability Testing	• Coupon Testing	• Ongoing
		• Subelement Rig Testing - RTRC HPTC Rig	• De-scoped
		• Modeling for CMC Durability	• Future/TBD
	• EBC Durability Testing	• Coupon Rig Testing - RTRC Cyclic Steam Rig, High Velocity Steam Jet Rig	• Ongoing
		• Subelement Rig Testing - RTRC HPTC Rig	• De-scoped
		• Modeling for EBC Durability	• Future/TBD

4.4 CLOSING REMARKS

High Temperature CMC Vane Technology is a key technology investment that P&W has fully committed to for next generation turbine engines. To fast-track this enabling technology, accelerated durability testing is required to ensure that this new material capability will be able to achieve the component life requirements necessary for next generation single-aisle propulsion systems. P&W has outlined a TRL/MRL path to establish testing to accelerate this durability learning, and ultimately deliver this technology into the next generation single-aisle product. During the period of performance of this contract, along with internally funded efforts, P&W has advanced CMC technology readiness level through TRL4 and completed relevant coupon testing for TRL5. Task 2.2 EBC Durability highlighted challenges in P&W's current EBC material system under commercial engine conditions. This critical knowledge will be implemented to driving our next generation EBC system development. In conjunction with P&W's internal development and learning gained under this contract, P&W is poised to proceed to component validation in TRL5. P&W's vision is to then implement this high temperature CMC technology in future engine tests.

5 REFERENCES

[1] Callaway, E.B. and Zok, F.W., 2020. Tensile response of unidirectional ceramic minicomposites. *Journal of the Mechanics and Physics of Solids*, *138*, pp. 103903.

[2] Parthasarathy, T.A., Cox, B., Sudre, O., Przybyla, C. and Cinibulk, M.K., 2018. Modeling environmentally induced property degradation of SiC/BN/SiC ceramic matrix composites. *Journal of the American Ceramic Society*, *101*(3), pp.973-997.

[3] Hay, R.S. and Chater, R.J., 2017. Oxidation kinetics strength of Hi-NicalonTM-S SiC fiber after oxidation in dry and wet air. *Journal of the American Ceramic Society*, *100*(9), pp.4110-4130.

[4] S. L. dos Santos e Lucato, O. H. Sudre, D. B. Marshall, “A Method for Assessing Reactions of Water Vapor with Materials in High-Speed, High-Temperature Flow”, Journal of the American Ceramic Society, Vol. 94, issue s1, June 2011, pp. s186-s195.

[5] M. Ridley and E. Opila, “Thermomechanical and Thermochemical Stability of $HfSiO_4$ for Environmental Barrier Coatings”, Journal of the American Ceramic Society, Vol. 104, no. 7, July 2021, pp. 3593-3602.

[6] R. A. Golden, E. Opila, “A method for assessing the volatility of oxides in high-temperature high-velocity water vapor”, Journal of the European Ceramic Society, vol. 36, no. 5, January 2016, 1135-1147.

[7] Barringer, M., Coward, A., Clark, K., Thole, K.A., Schmitz, J., Wagner, J., Alvin, M.A., Burke, P., and Dennis, R., 2014, “The Design of a Steady Aero Thermal Research Turbine (START) for Studying Secondary Flow Leakages and Airfoil Heat Transfer,” GT2014-25570.

[8] Rozman, M., Berdanier, R.A., Barringer, M.D., and Thole, K.A., “Strategies for High-Accuracy Measurements of Stage Efficiency for a Cooled Turbine,” In Review for J Turbomach, TURBO-23-1338.

[9] Clark, K., Barringer, M., Johnson, D., Thole, K. A., Grover, E., and Robak, C., 2018, “Effects of Purge Flow Configuration on Sealing Effectiveness in a Rotor-Stator Cavity,” J. Eng. Gas Turb. Power, 140(11), pp. 112502.

[10] Monge-Concepción, I., Barringer, M. D., Berdanier, R. A., Thole, K. A., and Robak, C., 2023, “Use of Multiple Tracer Gases to Quantify Vane Trailing Edge Flow Into Turbine Rim-seals,” J. Turbomach., 145(1), pp. 011006.

[11] Owen, J. Michael. "Prediction of Ingestion Through Turbine Rim Seals—Part 2: Externally-Induced and Combined Ingress." In Turbo Expo: Power for Land, Sea, and Air, vol. 48845, pp. 1083-1093. 2009.

[12] Gὺlder, O. L., “Flame Temperature Estimation of Conventional and Future Jet Fuels”, *Journal of Engineering for Gas Turbines and Power*, Vol. 108, April 1986, pp. 376-380.

[13] Gordon, S. and McBride, B.J., “Computer Program for Calculation of Complex Chemical Equilibrium Compositions and Applications”, NASA Ref 1311, Oct 1994.

[14] Lefebvre, A. H. and Ballal, D. R., Gas Turbine Combustion, Alternative Fuels and Emissions, CRC Press, 2010.